Multi Active Electron Effects in the Strong-Field Ionization of Transition Metal Atoms and Clusters

Smits, M.

2005

document version
Publisher's PDF, also known as Version of record

VRIJE UNIVERSITEIT

Multi Active Electron Effects in the Strong-Field Ionization of Transition Metal Atoms and Clusters

ACADEMISCH PROEFSCHRIFT

ter verkrijging van de graad van doctor aan
de Vrije Universiteit Amsterdam,
op gezag van de rector magnificus
prof.dr. T. Sminia,
in het openbaar te verdedigen
ten overstaan van de promotiecommissie
van de faculteit der Exacte Wetenschappen
op dinsdag 22 februari 2005 om 15.45 uur
in de aula van de universiteit,
De Boelelaan 1105

door
Marc Smits
geboren te Nijmegen

promotoren:	prof.dr. W.M.G. Ubachs
	prof.dr. C.A. de Lange
copromotor:	prof.dr. A. Stolow

Ancient Indian Proverb
"We do not inherit the Earth from our Ancestors, we borrow it from our Children."

List of publications

Stable kilohertz-rate molecular beam laser ablation sources
Marc Smits, C.A. de Lange, Susanne Ullrich, T. Schultz, M. Schmitt, Jonathan G. Underwood, James P. Shaffer, D.M. Rayner and Albert Stolow
Review of Scientific Instruments **74**, 4812-4817 (2003).

Femtosecond infrared strong field ionisation of metal clusters produced by kHz ablation
Marc Smits, C.A. de Lange, Adrian Pegoraro, D.M. Rayner and Albert Stolow
In "Femtochemistry and Femtobiology; Ultrafast Events in Molecular Science, Proceedings of the Femtochemistry VI conference", Paris 2003 (Eds. Monique M. Martin and James T. Hynes), p. 61 - 65, Elsevier, 2004.

Absolute Ionization Rates of Multielectron Transition Metal Atoms in Strong Infrared Laser Fields
Marc Smits, C. A. de Lange, A. Stolow and D.M. Rayner
Physical Review Letters **93**, 213003 (2004)

Dynamic Polarization in the Strong-Field Ionization of Small Metal Clusters
Marc Smits, C. A. de Lange, A. Stolow and D.M. Rayner
Physical Review Letters **93**, 203402 (2004)

Ionization dynamics of extended multielectron systems
M. Kitzler, J. Zanghellini, Ch. Jungreuthmayer, M. Smits, A. Scrinzi and T. Brabec
Physical Review A **70**, 041401(R) (2004)

Complexe Materie in Intense Velden: Voorbij de Storingstheorie
Marc Smits
Het Nederlands Tijdschrift voor Natuurkunde, Submitted

Non-resonant strong-field ionization of multielectron systems: 1. Transition metal atoms
Marc Smits, C.A. de Lange, Markus Kitzler, Thomas Brabec, D.M. Rayner and Albert Stolow
In preparation

Non-resonant strong field ionization of multielectron systems: 2. Transition metal clusters
Marc Smits, C.A. de Lange, Adrian Pegoraro, D.M. Rayner and Albert Stolow
In preparation

CONTENTS

1. INTRODUCTION

Since the invention of chirped pulse amplification of femtosecond laser systems, intensities over 10^{15} W/cm^2 are readily available [1, 2]. These intensities correspond to electric field strengths of over 10^9 V/cm, producing forces that are comparable to the forces that bind matter. Femtosecond lasers are therefore a promising tool for the precise manipulation of atomic forces with little energy per pulse. For instance, to reach the intensity mentioned above, a pulse of only 10 μJ at 800 nm and a pulse duration of 100 fs has to be used with an $f_\# = 2$ ($f_\#$ is the f-number) optic. There are however complications in the theoretical description of strong-field processes at these high intensities: the correction to the energy levels by the dynamic Stark shift and the failure of the perturbative approximations. For a system with a polarizability of *e.g.* 4 $\mathring{A}^3$ (Xenon) the dynamic Stark shift leads to a correction to the energy levels of more than 100 meV relative to the field free Eigenstates. This means that during every optical period, all Eigenstates will move up and down by more than 100 meV. Perturbation theory, where the field is assumed to have little influence on the system, becomes inapplicable. Highly nonlinear interactions have to be taken into account and alternative theories to describe strong-field processes had to be developed [3, 4, 5, 6, 7]. Strong-Field Ionization (SFI) is traditionally described for two limiting cases [8, 9, 10]: MultiPhoton Ionization (MPI) and tunnel ionization. In the MPI regime, the system absorbs an integer number of photons until the ionization energy is exceeded (vertical arrows in figure 1.1). A simplified tunnel ionization picture can be understood as a barrier suppression ionization (BSI) mechanism as depicted in figure 1.1 [9, 11]: the system with a Coulomb potential (dotted line) interacts with the laser field (dashed line), resulting in a distorted Coulomb potential. The distortion of the potential by the laser field leads to the formation of a barrier (solid line). By increasing the laser field sufficiently, the barrier can be suppressed until the electron can escape classically over the top of the barrier (horizontal arrow in figure 1.1). Quantum mechanically, an electron can penetrate through this barrier by tun-

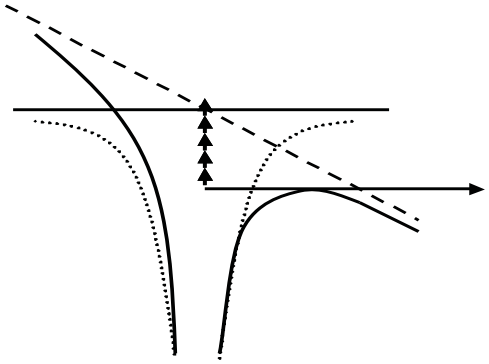

Fig. 1.1: The process of tunnel ionization can be understood by considering the interaction of the laser field (dashed line) and the potential of the system (dotted line). The result is a distorted potential (solid line) where the electron can quantum mechanically tunnel through the barrier or classically escape over the top of the barrier (horizontal arrow). Distinguishing tunnel ionization from the Multi Photon Ionization (MPI) process where an integer number of photons is absorbed to exceed the ionization potential (vertical arrows), is based upon the Keldysh parameter (see text for details).

neling before it is fully suppressed. In order to distinguish between the MPI and tunneling regimes, the theoretical description by Keldysh can be used as a first indication [4]. The Keldysh adiabaticity parameter (γ) is defined as the ratio of the tunneling time and the laser period, i.e.

$$\gamma = \frac{\text{tunneling time}}{\text{laser period}}. \tag{1.1}$$

When $\gamma \gg 1$, the tunneling time is larger than the laser period such that the electric field will change direction while the electron is still underneath the barrier. Therefore, tunnel ionization is completely suppressed and ionization takes place in the MPI regime. For the other limiting case, where $\gamma \ll 1$, ionization takes place in the tunneling regime [1].

Experimental studies on SFI of noble gas atoms and molecules have led to the discovery of many exciting highly nonlinear phenomena:

Recollision After an electron has been removed from a (noble gas) atom, it will move away from the ion, still under the influence of the laser field. When

[1] Most measurements in this thesis take place at intensities where $\gamma \sim 1$ or $\gamma \ll 1$ for the specific systems, and therefore the dominating process in the SFI measurements occurs in the tunneling regime. In the modeling of the experimental results the MPI contribution is therefore neglected.

the electric field changes direction, the electron will be decelerated and turned around. Under certain conditions, the electron can collide with the ion and remove a second electron: *recollision ionization* [12]. It is possible to use the electron as a probe in a time resolved experiment, where the time resolution is now less than half an optical period [13]. Instead of removing a second electron during the interaction with the ion, the kinetic energy of the returning electron can also be converted into a photon in the X-ray regime [14]. Using few cycle laser pulses it is in principle possible to generate single *attosecond* pulses [15].

Above threshold ionization Measuring photoelectron spectra in SFI experiments has led to the discovery of *above threshold ionization* (ATI) [16]: More photons are absorbed than required for ionization. Energy absorption takes place during one optical cycle, leading to a maximum electron energy of 2 times the ponderomotive energy. Further interaction with the ion leads to higher energies of the electron to a maximum of 10 times the ponderomotive energy.

Coulomb Explosion By continuing to remove electrons from a molecule, the nuclear repulsion will finally lead to an explosive dissociation process. The spatially resolved detection of the fragments contains information about the structure and dynamics of the parent molecule [17].

Strong-field Control Using genetic algorithms, the temporal profile of strong laser pulses can be optimized to control (complex) chemical processes [18, 19]. A recent experiment proposes an efficient energy deposition scheme in C_{60} [20].

Dielectric Modification On a macroscopic level, the interaction between the strong laser field and bulk material will lead to the formation of a plasma (free carriers). The subsequent interaction between the plasma and the bulk material results in ejection of material (laser machining [21]) or in modification of the optical parameters (dielectric modification [22]). The latter can be used to write waveguides inside dielectric materials.

1.1 *Single Active* versus *Multi Active Electron Systems*

Many theories describing tunnel ionization rely on the theory developed by Wentzel, Kramers and Brillouin (WKB). The potential is assumed to be one-dimensional and slowly varying, or more specifically the change in the potential over one de Broglie wavelength is small. Since the de Broglie wavelength of an electron tends to zero classically, WKB theory is a semi-classical approxima-

tion. The wavefunctions are found by generalizing the results of an electron in a constant potential, where the wavefunction ψ is given by $\psi = \exp i \int p \mathrm{d}x$. The constant momentum p is replaced by a power series and substituted in the Schrödinger equation. All terms that depend on the first and higher order derivatives of the potential are now neglected, since the potential is assumed to be slowly varying. However, the wavefunctions are only valid in the limit far away from a barrier where the momentum differs significantly from zero. Combining the two limiting wavefunctions from both sides of the barrier by matching the derivatives using the connection formulae, yields a continuous wavefunction. From this, a tunneling rate is obtained that depends exponentially on the area under the barrier.

The next approximation that underlies most theories is the *Single Active Electron* (SAE) approach. It is assumed that only the tunneling electron responds to the laser field and that all other electrons remain unaffected by the field. A justification for this approach in the case of noble gas atoms will be discussed in 1.2.

A highly successful theory to predict tunneling rates in SAE systems (noble gas atoms) was developed by Ammosov, Delone and Krainov (ADK) [7]. An analytical expression for cycle averaged tunneling rates was derived in terms of the quantum numbers n, l and m of hydrogen-like systems. It requires the Keldysh parameter to be $\ll 1$ and it is based on the above approximations. This theory is a generalization of the tunneling theory for the ground state of the hydrogen atom developed by Perelomov *et al.* [3]: the ionization rates are cycle averaged, are valid for any arbitrary state of the hydrogen atom and include a correction for the quantum defect (δ) by replacing n with $n^* = n - \delta$. Later extensions of these theories include MPI contributions and are valid for both $\gamma \ll 1$ and $\gamma \gg 1$ [23]. Other theories include the Keldysh theory [4] and the Keldysh-Faisal-Reiss theory[5, 6]. An experimental study by Walker *et al.* shows excellent agreement with ADK theory at high intensity and an SAE numerical simulation (including MPI) predicts correctly the ionization rate over 12 orders of magnitude in signal [8].

Molecules are inherently *Multi Active Electron* (MAE) systems and introduce many complications in the description of strong-field processes. Molecules have a certain shape and ionization can be different along each of the axes of the molecule. Alignment effects of the molecule with respect to the applied laser field can influence the ionization behavior drastically [24]. Furthermore, the extended geometry of molecules yields a more complex potential than the atomic

Coulomb potential. Also, typical timescales of the electron motion within the potential can become larger than the laser period and lead to non-adiabatic behavior. Finally, molecules consist of two or more nuclei that can move during the ionization process. This can influence the ionization dynamics and can lead to fragmentation. Although no unifying theory is currently available to describe the ionization dynamics of molecules in strong laser fields, many theoretical and experimental studies are available.

Molecular Keldysh Parameter When the width of the molecular potential becomes larger, the effect of the laser field on the height of the barrier is increased. A theoretical modification of the Keldysh parameter is proposed and an increase in the tunneling rate is predicted [25].

Non-adiabatic Dynamics The increase of the width of the barrier will increase the density of states and can lead, irrespective of the (modified) Keldysh parameter, to non-adiabatic transitions [26, 27].

Enhanced Ionization Due to processes like *bond softening* or simply nuclear repulsion of charged parts of the molecule, the nuclei can move apart during ionization process. Because of the separation, the barrier is suppressed further, but at the same time a barrier in between the two nuclei is formed. At a critical distance, the combination of the two barriers is such that tunneling of a localized electron from one side of the potential is enhanced [28].

Plasmon Resonance When several electrons are removed from a cluster of atoms, the nuclear repulsion will lead to an expansion of the cluster and at the same time, a decrease in the plasmon resonance frequency. When this frequency reaches the laser frequency, the cluster will explode and produce highly charged ions [29].

Taking the above processes into account, one might expect to find that molecules are easier to ionize than noble gas atoms of similar IP's. The contrary is true: two extensive studies by Hankin *et al.* [30, 24] and Lezius *et al.* [26, 27] showed for a large class of conjugated organic molecules, that tunneling rates are smaller than expected from ADK theory. A similar effect is observed in the damage threshold of surfaces [31] and in some diatomic molecules [32].

The origin of this suppression of ionization is the topic of this thesis and will be addressed in the next section.

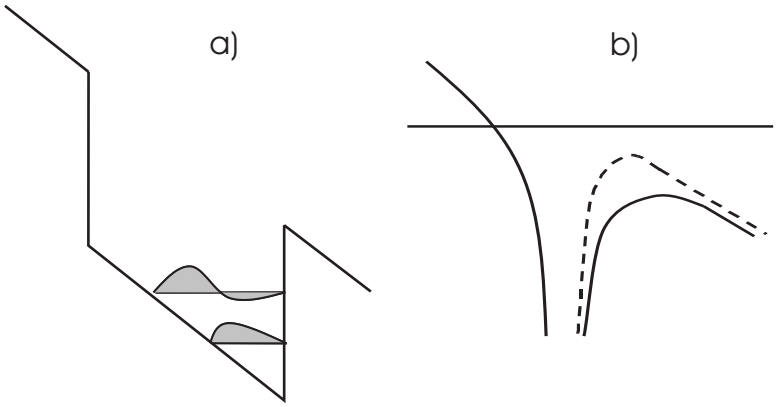

Fig. 1.2: In a *Multi Active Electron* (MAE) system, all electrons will respond to the laser field by a collective motion towards one side of the potential (a). The effect is a dynamic polarization and therefore an increase in the height of the barrier (dashed line) relative to a potential (solid line) where this polarization is ignored (b). As a result, Strong-field Ionization (SFI) in MAE systems is suppressed.

1.2 Dynamic Screening in Multi Active Electron Systems

When an MAE system is placed in a strong laser field, not only the tunneling electron, but all electrons will respond to the laser field. A full calculation, taking into account all electron correlations, to obtain the true potential of a MAE system in a strong laser field, is presently not possible [33, 34]. Qualitatively, the effect of the response of all electrons to laser field is a polarization of the system by a joint motion of the electrons to one side of the potential. Equivalently, the result of this motion will lead to a change in the barrier the electron has to tunnel through, as can be seen in figure 1.2. The response of all electrons (see figure 1.2a) result in a boost of the barrier (or a screening of the laser field) as shown in the schematic representation of the potential in an electric field (see figure 1.2b). Using classical electrodynamics, an approximate potential can be obtained that an escaping electron feels during the ionization process. The remaining ion is simulated as a singly positively charged conducting sphere in the presence of a static electric field. In figure 1.2b the potentials are shown by including and omitting the field induced polarization. It can be seen clearly that by including the polarization effect (the response of all electrons), the barrier is raised and the escaping electron has to penetrate a higher

barrier. It is for this reason that ionization is suppressed in MAE systems.

The suppression of ionization by dynamic screening is an effect of importance in most molecular systems. However, different explanations for the suppression of ionization in specific systems with a special symmetry, have been proposed. All these studies are based on quantum interference effects in systems where due to the symmetry, an effective destructive interference exists between the subwaves of the ejected electron [32, 35, 36]. However, these theories are only applicable to very few systems of a specific symmetry and therefore do not explain the general observation of the suppression of ionization in MAE systems.

At this point it is worth mentioning a long-standing problem why noble gas atoms behave like SAE systems with respect to SFI. One argument, briefly sketched by Lambropolous [10], involves the difference in electronic structure between noble gas atoms and many molecular systems. An MAE response in the SFI of noble gas atoms would require excitation of two or more electrons. Since doubly excited states in noble gas atoms lie well above the first ionization potential, these excitations are unlikely to happen during the removal of the first electron. More rigidly, in this thesis it is argued that the effect of a MAE response is a polarization of the system that results in a screening of the laser field and therefore a suppression of ionization. To understand the MAE nature of the ionization process, the contribution of a MAE response to the polarizability has to be considered. Since the contribution to the polarizability of electronically excited states is inversely proportional to their energy distance from the ground state, consideration of the energy gaps between multiple excited states and the ground state is important. In noble gas atoms, these energy gaps are very large and little contribution from multiply excited states to the polarizability is anticipated, resulting in an effective SAE response with respect to SFI.

1.3 Outline of the thesis

Traditionally, *Single Active Electron* (SAE) theories have been used to obtain lower limits of Strong-field Ionization (SFI) rates. Although this seems to be justified in the case of noble gas atoms, not very surprisingly the SAE theories have been shown to fail dramatically when applied to systems with many electrons, *e.g.* molecules. Unfortunately, no theoretical calculations are available for *Multi Active Electron* (MAE) systems. In this thesis a qualitative model is presented that explains the observed behavior of MAE systems and detailed

results are provided that can be used as test cases in the development of new quantitative MAE theories. First, relatively simple prototype systems with many equivalent electrons (*i.e.* a strong MAE character) are studied: transition metal atoms. Next, the clusters of the transition metal atoms are studied, where the complexity of the system can be varied by increasing or decreasing the number of atoms per cluster.

All measurements of this study take place in the gas phase and the ion yield as a function of the laser intensity is measured. The method for the data analysis as well as the vacuum and laser setup are presented in chapter 2. The detailed design of a novel kilohertz laser ablation source to bring the metal atoms into the gas phase is discussed in chapter 3. The source operates at a 50 times higher repetition rate (or more) than existing sources, making the elaborate experiments of this study feasible. Test results of the source are presented for the ablation of one of the transition metals (niobium), as well as for the laser desorption of a biologically relevant molecule (Guanine).

The atomic beam of the kHz laser ablation source is first used in chapter 4 to study the SFI of Vanadium (V), Niobium (Nb), Tantalum (Ta), Nickel (Ni) and Palladium (Pd). Saturation intensities, that can be used as a first-order indication of the "ease" of ionization, have been obtained. Further data analysis yielded the absolute ionization rates that can be compared directly to numerical simulations. First, the results are (naively) compared to SAE theories, since no full calculations are presently available that take all electron interactions during the SFI process into account. Next, a simplified but limiting model is provided (tunneling out of Zero Range Potential: ZRP). Results of a qualitative Time-Dependent MultiConfigurational Hartree-Fock (TD-MCHF) one-dimensional theory that are published elsewhere, are briefly reproduced.

In order to study the strong-field dynamics of the transition metal clusters, the source conditions were slightly modified to favor cluster production. Clusters bridge the gap between atomic and solid-state phenomena and allow to study the SFI dynamics of systems with growing complexity. A quantitative classical model (Conducting Sphere Model: CSM) is proposed that takes the MAE effect into account as the polarizability of the system. The properties of small metal clusters can differ drastically from predictions by classical theories, but generally, when the clusters are growing larger, their properties converge to bulk behavior. By studying the ionization behavior as a function of the number of atoms per cluster, polarization effects in the SFI process can be studied systematically. In chapter 5, saturation intensities for the charge states $z = 1$

and $z = 2$ are presented for the clusters of the transition metals V/Nb/Ta and Ni.

Finally, in the appendix (chapter 6) two short Letters that are based on part of the work of this thesis, are presented in their original form as published in the scientific journal "Physical Review Letters".

2. METHOD

In this thesis, absolute ionization rates as a function of intensity for several transition metal atoms and a measure of the "ease" of ionization (the saturation intensity) for the atoms and small clusters have been measured. Conventional methods to study strong-field ionization processes use a tight laser focus and sample over the entire focal volume. In order to compare different experiments with each other and experiments with theory, it is necessary to obtain ionization efficiencies, absolute ionization rates and saturation intensities. Generally, this requires knowledge of experimental parameters that cannot always be obtained easily, like instrument sensitivity, concentration of the neutral species in the molecular beam, and absolute laser intensities. Therefore, relative ionization rates are often measured and compared to other experiments and theory by (arbitrary) scaling or alternatively, numerical integration over the irradiation volume is required. Furthermore, by integrating over the entire focal volume, subtle features of the ionization process that are very sensitive to the intensity, may be washed out. Examples are Ramsey oscillations [37, 38] and population trapping [39]. In this chapter an approach is described that defines the saturation intensity (I_{Sat}), circumvents the requirement of knowledge of many experimental parameters, and does not obscure any subtle features. Hereto an analytical expression of the intensity dependence of the ion signal is derived. Next, a method is described to retrieve absolute ionization rates from the experimental data. Finally, realization of the method is described and the intensity calibration is presented.

2.1 The Saturation Intensity and Absolute Ionization Rates

In this study a method is employed that was developed by Rayner and coworkers [24] and is similar to the approach used by Van Woerkom [40, 41] and Uiterwaal [42]. A slit of approximately 1/3 the size of the Rayleigh range is placed perpendicular to the laser propagation direction, so that integration

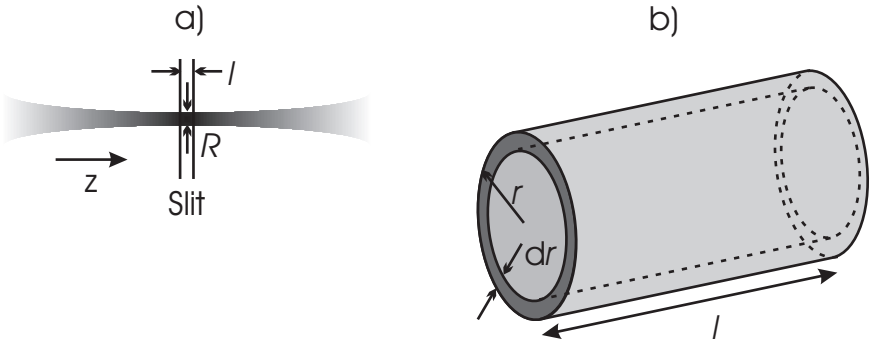

Fig. 2.1: By placing a slit, narrower than the Rayleigh range, an axially symmetric parallel beam geometry is obtained that simplifies the integration of the ion yield over the laser focus (a). Integration has to be carried out over the volume elements defined by the length l and radius r of the cylindrical parts of the laser focus (b).

is constant over the z-direction (see figure 2.1a). An effective parallel axially symmetric beam is obtained that allows to derive an analytical expression of the intensity dependence of the ion yield.

Starting with the ionization process with rate $W(I)$,

$$A \xrightarrow{W(I)} A^+ + e^- \tag{2.1}$$

the concentration $[A^+]$ can be obtained using first order kinetics.

$$-\frac{\mathrm{d}[A^+]}{\mathrm{t}} = W(I)[A] \tag{2.2}$$

For a volume element $\mathrm{d}V = 2\pi r l \mathrm{d}r$ with radius r and length l as displayed in figure 2.1b, the ion signal $\mathrm{d}S$ is given by

$$\mathrm{d}S = \alpha 2\pi r c l \left(1 - e^{-\int_{-\infty}^{\infty} W(I(r,t))\mathrm{d}t}\right) \mathrm{dr} \tag{2.3}$$

where α is the instrument sensitivity and c is the concentration of neutral species. The ionization rate w depends on the intensity I(r,t) at radius r and time t. For a temporal beam profile f(t) and a Gaussian laser radial intensity profile $I_r = I_0 \times \exp(-r^2/R^2)$, with the peak intensity I_0 and the beam waist at the focus R, a change of variables from $\mathrm{d}r$ to $\mathrm{d}I$ leads to an expression for the ion signal S,

$$S = \alpha \pi R^2 c l \int_0^{\infty} \frac{\left(1 - e^{-\int_{-\infty}^{\infty} W(I_r f(t))\mathrm{d}t}\right)}{I_r} \mathrm{d}I_r. \tag{2.4}$$

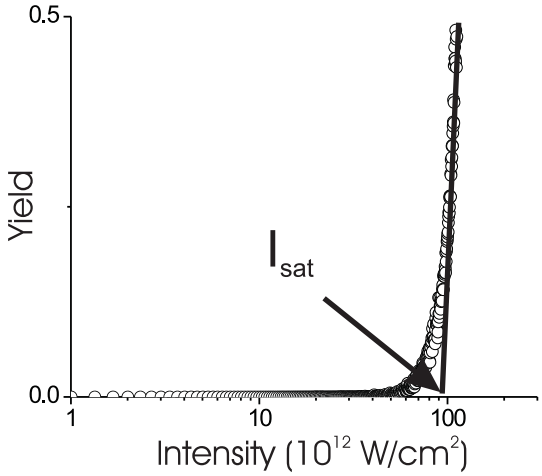

Fig. 2.2: Under parallel axially symmetric beam irradiation, a linear dependence of the ion signal on the logarithm of the intensity is predicted for any highly nonlinear ionization process. The saturation intensity is defined as the intercept of this linear behavior and the intensity axis. Here the experimental ion yield of the noble gas xenon is shown as a function of the logarithm of the intensity and the saturation intensity is indicated.

Next, equation 2.4 is differentiated with respect to $\mathrm{d}\ln I_0$ to obtain

$$\frac{\mathrm{d}S}{\mathrm{d}\ln I_0} = \alpha\pi R^2 cl\left(1 - e^{-\int_{-\infty}^{\infty} W(I_0 f(t))dt}\right) \tag{2.5}$$

At high intensity the term $e^{-\int_{-\infty}^{\infty} W(I_0 f(t))dt}$ becomes $\ll 1$ and the slope $\mathrm{d}S/\mathrm{d}\ln I_0$ becomes constant ($\alpha\pi R^2 cl$), i.e. at high intensity the ion signal depends linearly on the logarithm of the intensity. The expression for this linear dependence can be written as

$$S = \alpha\pi R^2 cl(\ln I_0 - \ln I_{\mathrm{sat}}) \tag{2.6}$$

The intersection of this line and the intensity axis is defined as the saturation intensity (I_{Sat}) and can be considered as a first-order indication of the relative ease of ionization. In the next section it is explained how the absolute intensity is obtained using an internal calibration method. The figure 2.2, shows the experimental ion yield of xenon *versus* the logarithm of the intensity. The linear dependency at high intensity is extrapolated to the intensity axis and the saturation intensity is indicated.

As an example, the tractable case of a multiphoton ionization process is considered that further clarifies the method for the situation that the exact expression for $W(I)$ is unknown. Carrying out the integration in equation 2.4 for a square temporal pulse profile of duration τ and an ionization rate $W(I) = \sigma_n I^n$, with σ_n as the n-photon cross section, yields

$$S = \frac{\alpha\pi R^2 cl}{n} \left[E_1(\sigma_n I_0^n \tau) + \ln(\sigma_n I_0^n \tau) + \gamma\right] \tag{2.7}$$

Here E_1 is the exponential integral function and γ is Euler's constant. In the high intensity limit, E_1 tends to 0 and the linear behavior predicted by eq. 2.6, is recovered. The expression for this linear behavior can be written as

$$S \rightarrow \frac{\alpha\pi R^2 cl}{n} \left(\ln(\sigma_n \tau) + \gamma\right) + \alpha \tag{2.8}$$

Finding the intercept of this line with the intensity axis yields an expression for the saturation intensity

$$I_{\mathrm{Sat}} = (\sigma_n \tau)^{-1/n} e^{-\gamma/n} \tag{2.9}$$

In the case of a multiphoton ionization process this identifies $\mathrm{I_{Sat}}$ as the intensity at which 43 % of the molecules in a region of constant intensity are ionized. It contains information on the order of the ionization process and the cross-section.

To summarize, as long as the ionization rate is a nonlinear function of the intensity, the general features of the intensity scan method in the case of an arbitrary ionization mechanism are as follows: in the high intensity limit, the dependency of the ion signal on the logarithm of the intensity becomes linear with a slope of $\alpha\pi R^2 cl$; the saturation intensity can be found using an expression for this linear behavior (see equation 2.6); and at $\mathrm{I_{Sat}}$ a fixed percentage of the neutrals is ionized (the percentage depends on the mechanism only, but not on any experimental details). The saturation intensity is therefore a molecular property and can be used as a first order indication of the "ease" of ionization. In this thesis, the intensity scan method is used to obtain saturation intensities for vanadium, niobium, tantalum, nickel and palladium atoms (chapter 4) and small clusters (5).

It is shown that the slope in a semilogarithmic plot of the signal *versus* intensity in the limit of high intensity characterizes the combination of all experimental parameters ($\alpha\pi R^2 cl$). It is therefore possible to obtain ionization

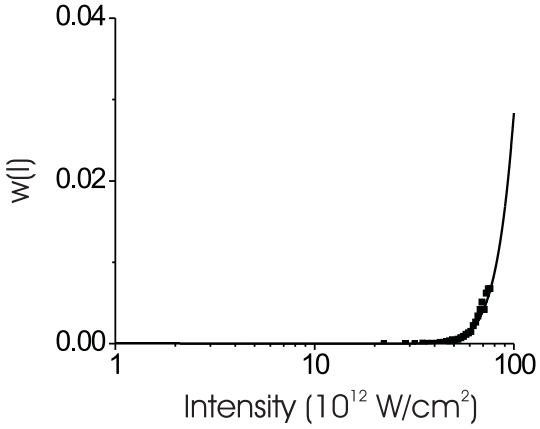

Fig. 2.3: From the data of figure 2.2 the derivatives at each intensity point are calculated and using equation 2.11 absolute ionization rates can be obtained. With this method there is no need for detailed knowledge of experimental factors like apparatus sensitivity, focal parameters and concentrations in a molecular beam. The solid line is the predicted ionization rate using ADK theory, where the pulse is assumed to be a square temporal pulse of 50 fs.

efficiencies and absolute ionization rates without specifically measuring the concentration of the neutrals in the molecular beam, the apparatus sensitivity or the beam waist at the focus. This makes a direct comparison possible without numerical integration or scaling between different experiments, or between experiment and theory. Writing the slope in the limit of high intensity as β_∞, and the slope at an arbitrary (lower) intensity as β, equation 2.4 can be rewritten as

$$\left(1 - e^{-\int_\infty^\infty W(I_r f(t))dt}\right) = \frac{\beta}{\beta_\infty}. \tag{2.10}$$

The term on the left can be recognized as the probability of ionization (P) or ionization efficiency (Φ). Further rearrangement leads to an expression for the integral of the rate over the temporal profile of the pulse

$$\int_\infty^\infty W(I_r f(t))dt = \ln \frac{\beta_\infty}{\beta_\infty - \beta} \tag{2.11}$$

Assuming a square temporal profile, the integral simplifies to $W(I)\tau$ from which the absolute ionization rate $W(I)$ is obtained. In figure 2.3 the example for the experimental data of xenon is shown. The experimental data are

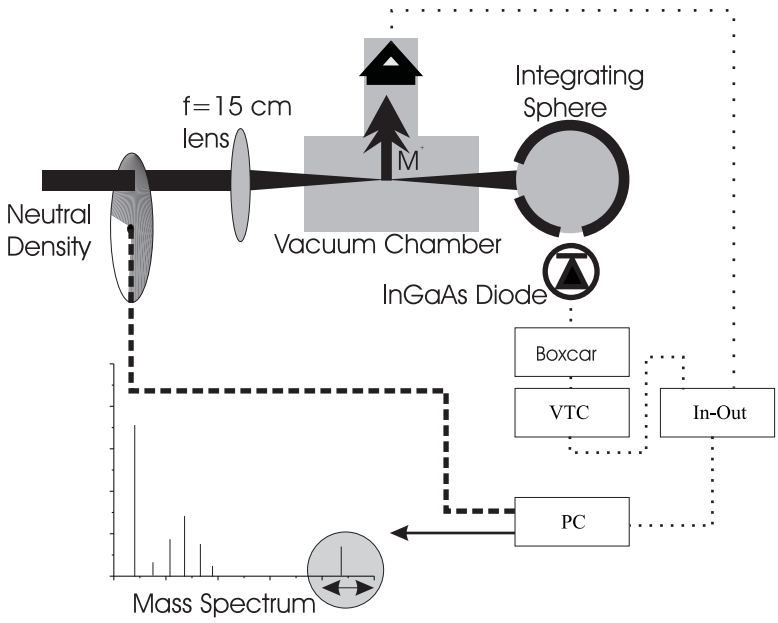

Fig. 2.4: The energies of the laser pulses are varied using a neutral density filter wheel. The pulses are focused into a linear time-of-flight mass spectrometer. For each individual laser shot, the energy is measured and a mass spectrum is recorded. To guarantee the correlation between the mass spectrum and the correct energy, a home-built voltage to time converter is used to write the energy information at the end of the mass spectrum. Using a calibration standard (xenon), energy is converted into intensity with an absolute error of less than 30 %

compared to theoretical rates calculated by ADK theory [7].

When the signal-to-noise ratio of the experimental data is good enough to obtain the slope at the high intensity limit with reasonable confidence, absolute ionization rates can be obtained by measuring the slope at any intensity and using equation 2.11. Alternatively, a function is fitted to the raw data in the semilogarithmic plot of the signal *versus* intensity and the derivative of this function is used to obtain the absolute ionization rates. This method will be used in chapter 4to obtain absolute ionization rates for the atoms of vanadium, niobium, tantalum, nickel and palladium .

2.2 Experiment

The laser parameters are chosen as to avoid complications induced by various forms of enhancing the ionization rates (see section 1.1): (i) the laser wavelength is chosen in the infrared regime (1.5μm), where both the Keldysh parameter is $\ll 1$ (see section 1), but also nonadiabatic dynamics of the electrons within the potential are more likely to be avoided; (ii) the pulse duration is sufficiently short to neglect motion of the nuclei during the laser pulse, leading to enhanced ionization and plasmon resonances; and finally (iii) measurements are taken at intensities around the saturation intensity, to avoid the formation of highly charged states and eventually Coulomb explosion.

In order to obtain saturation intensities and absolute ionization rates using equations 2.4 and 2.11, the laser intensity has to be varied while the ion yield is measured. Since an ablation source is used for metal cluster production that is inherently not very stable (see chapter 3), elaborate averaging is required. A neutral density filter wheel is used to vary the laser pulse energy and is controlled by the data acquisition computer (see figure 2.4). The laser beam intersects the molecular beam in the mass spectrometer, where for every individual laser shot a mass spectrum is recorded by a PCI based multichannel scaler card. The energy of the laser pulse is obtained using an integrating sphere and a InGaAs photodiode. A boxcar integrator is used to measure the laser energy. It is of uppermost importance that for every individual mass spectrum, the corresponding laser energy is recorded. The use of an analog to digital converter for the boxcar signal requires an additional readout by the data acquisition computer and can lead to a wrong correlation between the mass spectrum and the laser energy. Therefore, a home built voltage to time converter is employed to convert the energy information into a time delay. The energy information is now written in an empty part of the mass spectrum and only one readout is necessary to obtain both the mass spectrum and the laser energy information. To convert energy into intensity we used the previously described calibration method [24]. Using the known saturation intensity for xenon (obtained by ADK theory, that is shown to predict I_{Sat} very accurately for noble gas atoms), a measurement of the ion yield of xenon as a function of energy can be used to convert energy into intensity. Without the exact knowledge of the focal parameters, the semilogarithmic plot yields a saturation intensity that can be set to the theoretical value obtained by ADK theory. In this manner absolute intensities to an accuracy of better than 30 % can be obtained.

3. STABLE KILOHERTZ-RATE MOLECULAR BEAM LASER ABLATION SOURCES

We describe a stable kHz rate laser ablation/desorption supersonic molecular beam source for use in kHz rate laser experiments. With the development of modern lasers that typically operate at kHz rates, a need has arisen for stable molecular beam laser ablation/desorption sources that match this repetition rate to study involatile species. Many biomolecules of interest cannot be brought into the gas phase without thermal decomposition by simply heating the substrate and most (especially refractory) metals have melting and boiling points that are impossible to reach with conventional ovens. The source is based upon strong non-resonant interaction of a dithering laser focus with a rotating and translating solid rod, hydrodynamic transport of the ablated/desorbed material in Helium or Argon and subsequent supersonic expansion. Further design details include flexible and easy adjustment of the source that allows for rapid prototyping and optimization for kHz rate performance. Due to the high rate of sample removal, a major concern is clogging of the nozzle and laser input channel due to both material condensation and debris formation. In order to illustrate the range of applications, we demonstrate: (i) the kHz laser ablation of a high temperature refractory metal (Niobium) for use in studies of metal clusters; and (ii) the kHz laser desorption and jet-cooling of an involatile biomolecule (the DNA base Guanine) for use in spectroscopic and dynamical studies. This kHz source has been shown to be stable for over twelve continuous hours of operation ($> 4 \times 10^7$ laser shots). We believe that this design could readily be adapted to even higher repetition rate (> 10 kHz) experiments, should the need arise.

3.1 Introduction

The development of stable, commercially available kHz-rate femtosecond laser systems has engendered many new classes of experimental investigation [2]. Such investigations in the gas phase are normally limited to gaseous or relatively volatile systems. The general application of kHz-rate gas phase methods to involatile substances such as high temperature inorganic clusters or delicate biomolecules remains problematic. Simply heating the substrate to improve its vapour pressure is usually impossible for two reasons: firstly, many (especially transition) metals and inorganic solids have extremely high melting and boiling points; secondly, many bio-organic molecules thermally decompose upon heating. The use of laser ablation/desorption is one well-known technique that circumvents both these problems [43] and is the only way of producing refractory metal clusters. An important consideration in kHz-rate femtosecond studies is the long-term stability of the molecular beam source (*e.g.* flux, cluster distribution, internal and translational temperatures *etc.*). As ablation sources are not inherently very stable, experiments based upon this technique generally require extensive signal averaging. In addition, many powerful experimental gas phase methods are based upon the small signal limit of particle counting. For example, femtosecond time-resolved photoelectron spectroscopies [44, 45, 46, 47, 48] are generally restricted to small signals per laser shot in order to avoid higher optical non-linearities due to the inherent high intensities of amplified fs pulses [49, 50]. The use of gas phase techniques such as PhotoElectron PhotoIon Coincidence (PEPICO) Spectroscopy [51, 52] and Coincidence-Imaging Spectroscopy (also known as Angle-Resolved PEPICO or ARPEPICO) [53, 54, 55, 56]require much less than one particle per laser shot and hence long signal averaging times. As it is often unfeasible to operate an ablation/desorption source over a period of many days, it is necessary to increase the laser repetition rate in order to reduce averaging times. Ideally, laser ablation/desorption sources should match the repetition rate of the femtosecond laser system. A second area where high repetition ablation sources are of interest are experiments that hinge upon large flux, such as those involving mass-selected deposition [57] or direct linear absorption. If the ablation rate can be scaled without altering the concentration per pulse, significant timesaving can be achieved or, alternatively, less abundant species can be accumulated or studied. Laser ablation/desorption is governed by a series of complex processes, from the initial laser irradiation to the ejection of molecules and clusters and depends sensitively on the laser wavelength (λ), the

pulse duration (τ), the energy per pulse (E) [58, 59, 60, 61], the source design as it relates to the gas dynamics, as well as on optical, topological and thermodynamic properties of the target material. Many experimental and theoretical reviews have summarized and categorized the different mechanisms involved [62, 63, 64, 65], but sources are often developed on a trial and error approach. For the purpose of this discussion, we wish to distinguish between laser desorption and laser ablation. The former, of relevance to studies on involatile biomolecules, is predominantly in the regime of intermediate power densities and leads to the removal of neutral molecules from the surface. The latter, of interest to studies of inorganic and metallic clusters, requires high ablation laser power densities and, for high temperatures species, laser-plasma interaction. A significant issue for kHz rate ablation sources is the clogging of the nozzle due to condensation and debris formation. The three most important processes for debris formation are recoil ejection, subsurface boiling and exfoliation. Which of these are dominant depends on the target material and the laser characteristics. The first process, recoil ejection, is the result of the extremely high pressure in the nascent plasma. The melt on the surface of the plasma is squeezed to a droplet by the high pressure and produces particulates of less than a micron in size. The second process, subsurface boiling, is mainly a problem for metals with low melting points and high heat conductivity (*e.g.* aluminum). In this case, the time needed to heat the thermal diffusion layer is shorter than the time needed to evaporate the absorption surface. The explosive phase transition produces droplets similar to recoil ejection, although the ejection angles are different. The last process, exfoliation, is a result of extreme forces due to the highly energetic collisions of the ions from the plasma with the target bulk. Multiple melt-freeze cycles on the surface of the target roughen the surface and macroscopic particulates are formed. When these particulates break off by recoil forces, they may have dimensions of many microns and lead to source flow instabilities.

In the following, we present an overview of the design considerations for our highly versatile supersonic molecular beam source used in kHz rate femtosecond laser experiments. We illustrate its application in the areas of: (i) atomic and cluster beams of a high temperature refractory metal (Niobium); (ii) molecular and cluster beams of an involatile biomolecule which is considered difficult to produce using thermal methods (the DNA base Guanine).

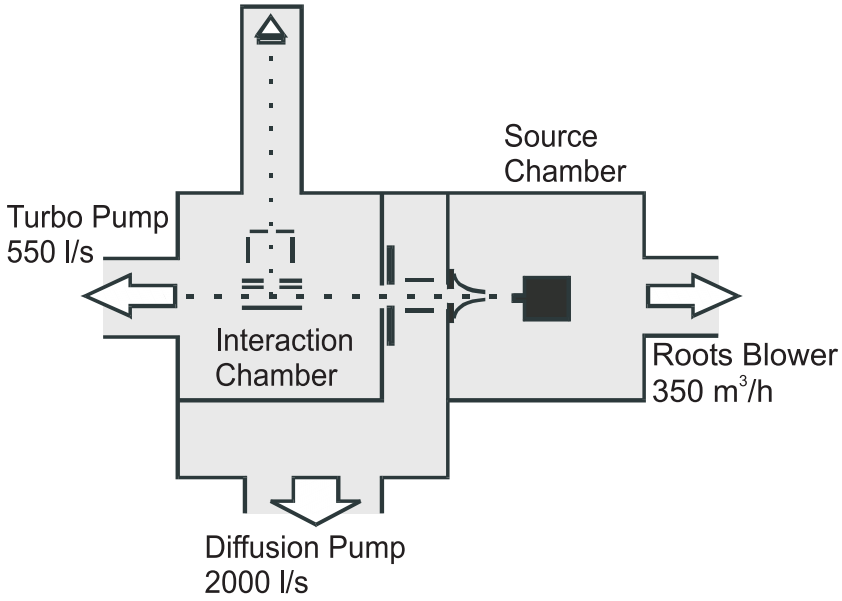

Fig. 3.1: The kHz ablation apparatus consists of three differentially pumped regions. The first or source region is pumped by a Roots blower (350 m^3/h, $< 10^{-1}$ torr during operation). The molecular beam enters the second region, via a 1 mm skimmer, pumped by a single diffusion pump (2000 l/s, $< 10^{-4}$ torr during operation). Residual ions formed during ablation are removed from the molecular beam by two deflection plates ($\Delta V_1 = 250$ V). The skimmed molecular beam passes through an aperture into the third or interaction region which is pumped by a turbomolecular pump (550 l/s) and contains the time of flight (TOF) mass spectrometer (both linear and reflectron). Another pair of deflection plates (ΔV_2) can be used to remove the initial molecular beam velocity, if required.

3.2 Design

Modern kHz laser systems are available with pulse durations ranging from a few femtoseconds to hundreds of nanoseconds, and wavelengths ranging from the near UV to the infrared. For applications to laser ablation, the wavelength dependent absorption penetration depth and the target material dependent thermal diffusion rate have to be considered. For nanosecond pulses, the thermal diffusion length in a typical metal is orders of magnitude larger than the absorption depth. A large volume of molten material is typically formed and a strong reaction with any laser-induced plasma is expected. At the other

extreme of femtosecond pulses, thermal diffusion can be neglected and the process is dominated by a highly non-linear optical absorption processes. In the present study, three different laser systems with pulses ranging from 100 ps to 150 ns are successfully demonstrated as (i) an ablation source for the generation of transition metal clusters and as (ii) a desorption source of involatile biological molecules. Our most successful laser system for ablation is an arc lamp pumped Nd:YLF laser (Positive Light Merlin), producing pulses of > 10 mJ/pulse in 150 ns at 527 nm. The second laser system, with only very moderate cluster production, is an NRC-design kHz diode-pumped grazing incidence Nd:YVO_4 slab laser with pulses of 1 mJ/pulse in 2 ns at 532 nm [66]. Optionally this laser can be operated as a picosecond amplifier using a ps Nd:YAG oscillator (Lightwave Electronics 131) as a seed-laser, shortening the 532 nm pulse to 100 ps. In this case, a very stable and clean source is achieved. Unfortunately densities of ablated species in the molecular beam are relatively low (approximately 10 times lower) and therefore we restrict the following discussion of kHz ablation sources to applications with the Nd:YLF laser. It is worth noting, however, that such diode-pumping technologies can be scaled to many tens of kHz repetition rate. High throughput sources for applications in spectroscopy or thin film deposition have as a major concern the high gas load and, hence, high pumping speed requirements. Employing pulsed nozzle designs can present difficulties at kHz rates in terms of stability and reproducibility when heated to high temperatures. Moreover, little is gained in controlling throughput because of the limited duty cycle (often ~ 3). A continuous carrier gas flow has therefore been implemented in the present study. Because throughput, ease of use and adaptability are more important in our experiments than cooling, we adopted a Campargue design [67] that operates at a high background pressure ($P_1 < 1$ torr) with use of only a single standard booster pump, instead of the Fenn-type design [68, 69], that operates at a sufficiently low background pressure to avoid interference with the expanding beam ($P_1 < 10^{-3}$ torr) with use of (several) large diffusion pumps. In figure 3.1 we show an overview of our triply differentially pumped vacuum chamber. The first or source region is pumped by an Edwards mechanical roots blower (EH500A, 350 m^3/h), allowing the source to operate in the Campargue-type configuration with background pressures of $< 10^{-1}$ torr during operation. The molecular beam enters the second or differential region, via a 1 mm diameter skimmer (Beam Dynamics), places 1 cm away from the nozzle. This reggion is pumped by a single diffusion pump (Edwards Diffstak 250, 2000 l/s) to pressures of $< 10^{-4}$ torr during operation. In this region, any

residual ions formed during ablation are removed from the molecular beam by two deflection plates ($\Delta V_1 =\sim 250$ V). [It is in principle possible to operate in the Fenn-type configuration by closing off the Roots blower and opening a bypass, or by moving the source holder and skimmer into the second region.] The distance from the source to the interaction point is kept as short as possible to maximize the beam density at the laser focus. The third or interaction region is differentially pumped by a turbomolecular pump (Varian V550, 550 l/s) and houses a linear time-of-flight (TOF) mass spectrometer. This high vacuum region can be isolated from the other regions by an NRC-design low profile gate valve.

In a kHz desorption/ablation source, the target material is removed at a sufficiently rapid rate that clogging of the nozzle and tooling of the substrate become serious problems. In our design, shown in figure 3.2, the target sample is a cylindrical rod of 6 mm diameter and up to 3 cm length. The source holder is a modified Smalley-type cluster source [70, 71] and is designed for easy adjustment. The inset in figure 3.2 shows the nozzle block detail (top view). The nozzle itself is machined as a separate insert (black) into this block and it functions as an optional growth channel. This allows for rapid prototyping and makes the source highly versatile. A variety of inserts with different diameters and lengths of growth channel, different materials of growth channel and nozzle, different diameters of the nozzle, and different diameters of the laser entrance aperture have been tested. Using a rotary motion feedthrough and an external stepper motor, the rod is simultaneously translated and rotated in helical fashion using a screw drive. Via bevel gears, the rotary motion of the drive leads to rotation of a perpendicular threaded shaft within an internally threaded block (white). The sample rod mounts, via a hex key, into the top of this threaded shaft. The sample rod is constrained to move within another block (gray) which also houses the nozzle insert. In this manner, a new sample spot can be provided to each ablation laser pulse in order to minimize the formation of deep pits and debris formation processes like exfoliation. At the endpoints of the screw drive, the direction of the stepper motor is reversed and helical motion of the opposite sense occurs. The carrier gas is introduced along a long flow tube (which also serves as the laser input tube) and through a small aperture to the rotating sample, as shown in the insert "top view") in figure 3.2. In this manner, debris ablated from the target surface does not reach the laser input window, which would otherwise become obscured over time. The distance from the laser input window to the sample rod is 25 cm. With a $f = 300$ mm lens, the ablation laser

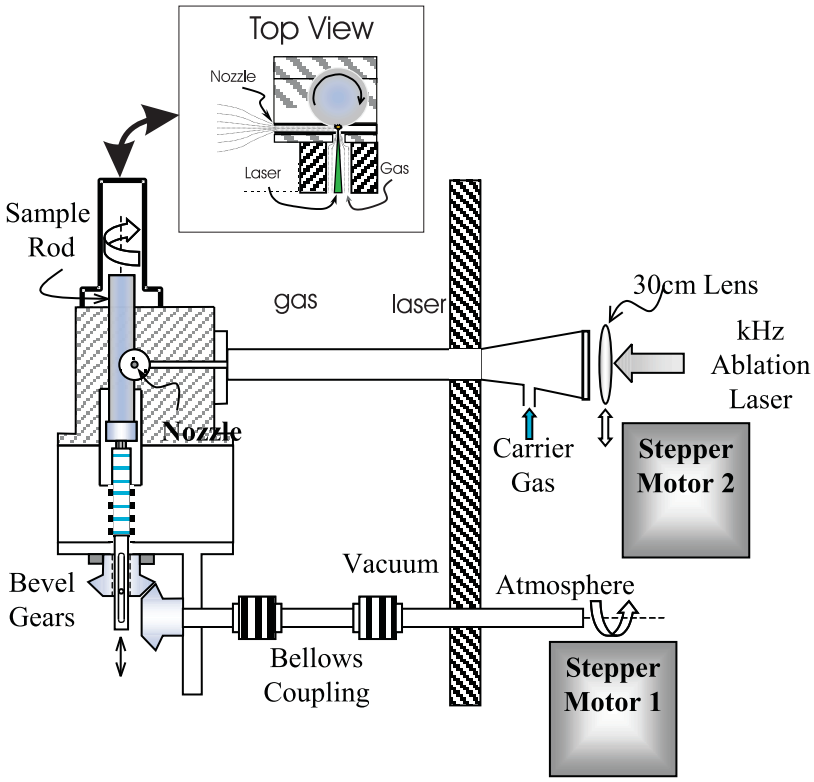

Fig. 3.2: Using a rotary motion feedthrough and an external stepper motor, the sample rod is simultaneously translated and rotated using a screw drive. The target is a cylindrical rod of 6mm diameter and up to 3 cm in length. The source holder is a modified Smalley-type cluster source and allows for easy adjustments. As shown in the insert, the nozzle is machined in a separate insert that functions as an optional growing channel. At the endpoints of the screw drive, the direction of the stepper motor is reversed and helical motion of the opposite sense occurs. The carrier gas is introduced along a long flow tube (also the laser input tube) and through a small aperture to the rotating sample, as shown in the TOP VIEW insert. The length of the channel between the sample rod and the nozzle can be varied using different inserts (black).

can be focused onto the target with minimum spot size of about 15 μm. For most stable operation, however, the focus is pulled slightly backwards, yielding an estimated spot size of about 100 mm. This provides upper limits for the maximum intensities of $\sim 10^9$ W/cm^2 and maximum energy densities of $\sim 10^8$

J/cm^2 for the 150ns Nd:YLF laser. The use of separate inserts containing the nozzle and growth channel also allows for easy exchange and cleaning. We have found that for stable long term operation, both the nozzle and laser/carrier gas aperture diameters must be at least 2 mm. The length of the channel between the sample rod and the nozzle can be varied using different inserts. In some cases (*e.g.* metals), this length defines a clustering region that governs the cluster size distribution. Different materials for the growth channel and the nozzle have been tested, with standard glass being the most successful in our metallic cluster experiments. Depending on the characteristics of the growth channel, the time spent in the channel is up to several hundreds of microseconds and produces metallic (here Niobium) clusters up to 40 atoms. Accurate, stable control of the helium or argon (Air Products, zero grade) buffer gas is achieved with mass flow controllers (MKS 1159B). Our pumps can support a continuous flow of up to 1400 sccm. With a growth tube of 2 mm in diameter and approximately 1 cm in length, this corresponds to a stagnation pressure of $\sim$ 10 torr at the throat of the nozzle. The buffer gas provides conditions for the cooling and clustering of the ablated/desorbed material by collisions in the source exit channel. In addition the large flow rate is important in keeping the channel and apertures in the source unclogged. With our design, flow rates below 800 sccm lead to clogging of the nozzle and laser aperture within one hour of operation. The motion of the rod should be sufficiently fast that a "fresh" surface spot can be presented to the ablation laser every millisecond (*i.e.* kHz rate), otherwise signal levels degrade quickly. Even this, however, is not sufficient for stable long-term operation. We have observed, due to the reproducibility of the helical track produced by the drive motion and the high rate of material removal, that a deep thread is cut into the rod. This leads to a strong diminution and eventual loss of the signal. To avoid this, we *dithered* the up-down position of the laser focus, as shown in figure 3.2, by displacing the focusing lens slightly (with a $\sim$ 0.1 Hz period, $\sim$ 1 mm amplitude of travel) and, importantly, in an *asynchronous* manner, using a second stepper motor. With this approach, the pattern of laser spots on the rod surface do not produce regular helices. This simple modification allowed us to operate kHz rate ablation sources for over twelve continuous hours (*i.e.* $> 4 \times 10^7$ laser shots). Upon inspection of the rod after such a long run, the rod diameter was significantly thinner but no thread pattern could be observed on the surface.

3.3 Experimental Setup

The 50 cm time-of-flight mass spectrometer consists of a standard Wiley-McLaren and (optional) reflectron TOF mass spectrometer. Single ions are detected using Burle microchannel plate detectors (MCPs), fed directly into a pulse amplifier and discriminator (Phillips). Mass spectra are recorded using either a stand-alone multichannel scaler (Stanford Research SR430) or a PCI-based multichannel scaler (FastComtec P7888). In order to compensate for any potentially large lab-frame molecular beam velocities, deflection plates ($\Delta V_2 = 0 - 150$V) can be used to remove the component of velocity perpendicular to the time-of-flight axis and thus straighten the ion trajectories. This can help to produce an essentially background free mass spectrum, depending on the mass of interest and the nature of ablation. In some cases, active background subtraction can be implemented in order to ensure the signal originates from laser ablation. This is simply achieved by alternating at 2000 shot intervals, with the ablation laser unblocked/blocked and the background signal subtracted.

The present National Research Council femtosecond laser system, depicted in figure 3.3, has been described in detail elsewhere [72]. Briefly, a fs Ti:Sa (Spectra-Physics "Lok-to-Clok" Tsunami) and a ps Nd:YAG (Lightwave Electronics 131) oscillator are individually locked, via phase-locked loops, to a stable 80 MHz external reference oscillator, thus synchronizing the oscillators. The Ti:Sa pulses are regeneratively amplified (Positive Light Spitfire) using a diode-pumped Nd:YLF laser (Positive Light Evolution30). These amplified pulses are subsequently passed through a two-pass linear Ti:Sa amplifier, pumped by another Nd:YLF laser (Positive Light Evolution30). After recompression, transform-limited 800nm pulses of 80 fs and 2.7 mJ are obtained. The ps Nd:YAG pulses are amplified using an NRC-design kHz diode-pumped grazing incidence Nd:YVO_4 slab laser [66], producing 1 mJ, 100 ps pulses at 532 nm. The arc lamp pumped Nd:YLF laser (Positive Light Merlin), with pulses of > 10 mJ/pulse in 150 ns at 527 nm is synchronized with the fs laser system using a digital delay generator. The amplified fs laser system pumps four optical parametric amplifiers (two Quantronix/LightConversion TOPAS, two Clark-MXR NOPA). Laser pulse energies are monitored on a shot-to-shot basis, using integrating spheres with photodiodes, for kHz rate active data filtering and sorting.

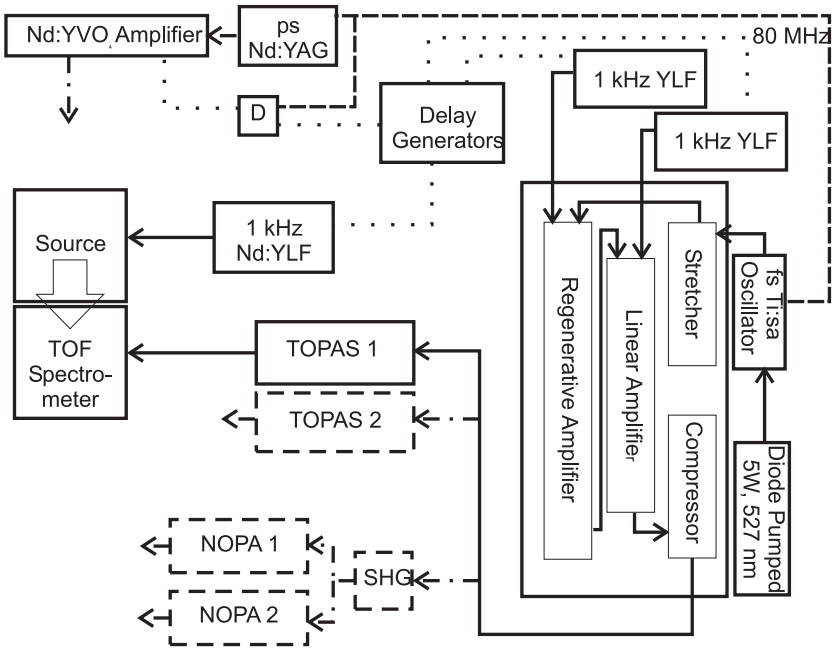

Fig. 3.3: A fs Ti:Sa (Spectra-Physics 'Lok-to-Clok' Tsunami) and a ps Nd:YAG (Lightwave Electronics 131) oscillator are locked, to a 80 MHz external reference oscillator. The Ti:Sa pulses are regeneratively amplified and subsequently passed through a two-pass linear Ti:Sa amplifier. Each Ti:Sa amplifier is pumped by a kHz Nd:YLF laser. After recompression, transform-limited 800nm pulses of 80fs and 2.7 mJ are obtained. The ps Nd:YAG pulses are amplified using an NRC-design kHz diode-pumped grazing incidence Nd:YVO4 slab laser, producing 1mJ, 100ps pulses at 532nm. The amplified fs laser system pumps four optical parametric amplifiers (two Quantronix/LightConversion TOPAS, two Clark-MXR NOPA). An arc-lamp pumped kHz Nd:YLF laser (Positive Light Merlin), synchronized to the Ti:Sa lasers, is used for kHz rate ablation.

3.4 Demonstration and applications of kHz ablated beams

3.4.1 Strong Field Ionization of Transition Metal Clusters

As a first example of the use of kHz rate laser ablation sources, we discuss in the following aspects of our studies in the strong field ionization of metal clusters. Modern amplified femtosecond lasers can reach electric field strengths of $> 10^9$ V/cm, exceeding those that bind matter. The study of strong field physics con-

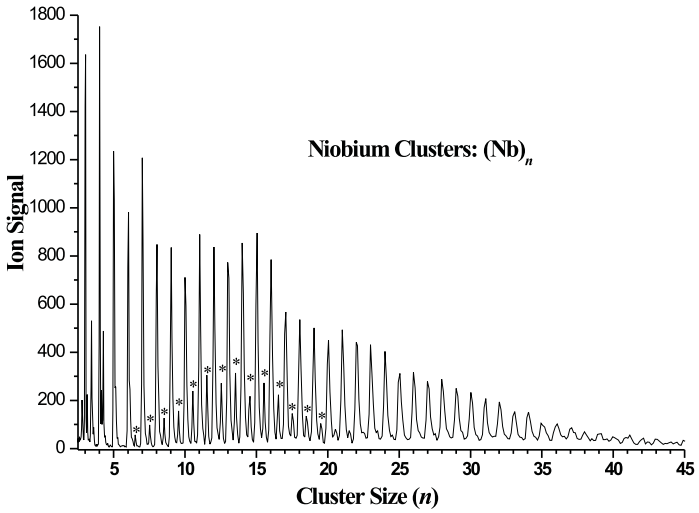

Fig. 3.4: A typical mass spectrum, recorded in five minutes, of kHz-rate laser ablated Niobium clusters, non-resonantly ionized at a laser intensity of 10^{13} W/cm^2 (l=0.8mm). With this particular growth channel, a broad cluster distribution obtained with this method. The mass peaks marked with an asterisk are the doubly charged cluster species. This kHz source is stable for over 12 continuous hours of operation. For details, see the text.

tributes to our understanding of strong field quantum control [19] and extreme non-linear optics [73]. A technological application is in laser machining, where precise removal of material is possible by using laser intensities that exceed the damage threshold [21]. Most current models of strong field interaction with matter are based upon the highly successful atomic Quasi-static model [8]. Recently, these Quasi-static models have been shown to fail for certain classes of polyatomic molecules due to non-adiabatic multi-electron effects [26, 27]. These studies showed that multi-electron effects exist (specifically, strong suppression of ionization) even in the long wavelength limit due to the effects of dynamic electron polarization. In this regard, the strong field ionization of metal clusters should provide an ideal test case for the role of dynamic polarizabilities. Using the saturation intensity method [30], we have studied non-resonant (l=0.8 and 1.5 mm) strong field ionization of size post-selected metal clusters, using kHz rate laser ablation as the molecular beam source [74].

In this study we chose Niobium (Nb) as a model target metal. Nb is a typical transition metal with high melting and boiling points of 2477 K and 4744 K [75], respectively, and has the advantage of having only one natural isotope, simplifying the mass spectrum. Using the laser ablation method described above, we were able to generate stable (> 12 hours) cluster beams at a 1 kHz rate. For studies of strong field ionization, we used both $\lambda = 0.8$ and 1.5 μm wavelengths. Typical pulse durations were ~ 80 fs. Absolute laser intensities ($\pm 30\%$) were determined using the saturation intensity method with Xenon gas as a reference standard. For the 1.5 μm radiation, a maximum intensity of over 2×10^{14} W/cm^2 at the focus was achievable. At 0.8 μm, an order of magnitude higher intensity was achievable. A typical mass spectrum (recorded in five minutes) at an intensity of 1×10^{13} W/cm^2 (0.8 μm) is shown in Figure 3.4. Strong non-resonant field ionization of Niobium clusters is clearly observed. A broad cluster distribution is obtained with this method. The mass peaks marked with an asterisk are the doubly charged cluster species. The stability of this source allows for long duration experiments (such as the saturation intensity method which requires sampling over all laser intensities at each cluster mass) to be performed.

3.4.2 Pump-Probe Spectroscopy of Gas Phase Biomolecules and their Clusters

As a second demonstration of kHz rate ablation sources, we discuss in the following the study of involatile biomolecules in the gas phase. There is increasing interest in studies of biologically relevant molecules in the gas phase, triggered by the first applications of laser desorption/ablation techniques to involatile, organic molecules [76, 77]. The femtosecond (fs) pump-probe spectroscopic method, developed for the investigation of dynamical processes in photochemistry [78], is now reaching into the area of photobiology [79, 80]. One approach to studying details of ultrafast excited state electronic relaxation processes such as internal conversion and intersystem crossing is Femtosecond Time-Resolved Photoelectron Spectroscopy (TRPES) [47, 48, 81, 82, 83]. Due to its inherently low count rate, successful application of TRPES to involatile biological molecules demands a soft vaporization molecular beam source that is stable enough over an extended period of time to allow such spectra to be recorded.

In order to test our kHz laser ablation source for involatile biological molecules, we used the DNA base Guanine as an example. As for many biomolecules,

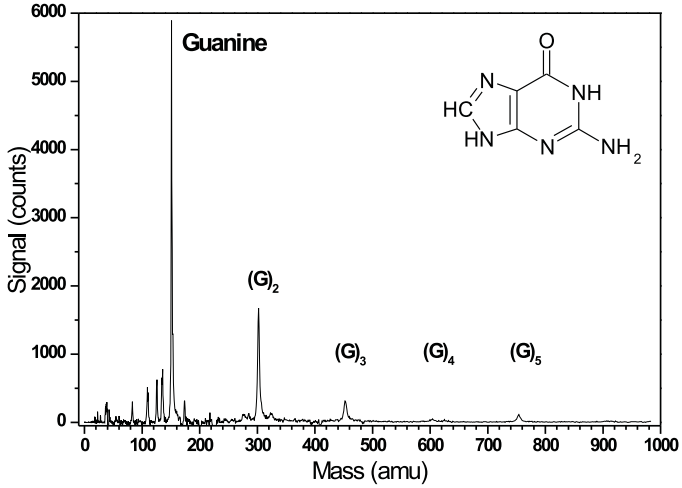

Fig. 3.5: A typical mass spectrum of kHz-rate laser ablated Guanine monomer and molecular clusters, resonantly ionized at 277 nm using 150 fs laser pulses. The count rate was 0.3 counts per laser shot, (i.e. 300 counts per second), a respectable signal for many purposes. Peaks marked with "*"correspond to loss of the NH2-group (m = 135 amu) and loss of N2CH2 (m = 109 amu) from the guanine monomer. For details, see the text.

simple heating of Guanine would lead to thermal decomposition before desorption [84]. Sample preparation for use in our ablation source involves pressing guanine powder (Sigma, 99% purity) into a quarter inch diameter rod under one to two tons of pressure. Although only neat guanine was employed in this demonstration, rods consisting of biomolecules and matrices or mixtures of biomolecules can be readily prepared.

We demonstrate the successful application of our kHz laser ablation source to the generation of jet-cooled molecular beams of guanine. The kHz ablation laser (attenuated to 1 mJ/pulse) was focused ($f/30$) onto the rotating, translating neat guanine rod. The guanine vapor was expanded through a 1 mm diameter orifice seeded in Ar at a flow rate of 1200 sccm. For probing the skimmed guanine molecular beam, we employed femtosecond laser (1+1) one-color resonant two-photon ionization of guanine at 277 nm (15 μJ/pulse, 150 fs). We present an example of a mass spectrum of kHz laser ablated guanine

in figure 3.5. [In order to demonstrate that the guanine signal originated from true laser ablation (as opposed to, for example, merely heating of the source region with the laser), we unblocked and blocked the ablation laser, at 2000 shot intervals, and subtracted any background signal]. The most prominent peak in the mass spectrum (m=151 amu) originates from the guanine monomer, with 3.000 counts per 10.000 laser shots. This is a respectable signal for the purposes of TRPES. Experiments are currently under way in our laboratory to use fs time-resolved two-colour TRPES to study the intramolecular dynamics of the isolated DNA bases. We note that cluster formation of up to five guanine molecules is also observed under the above conditions, which is an indication of a cold expansion. This suggests the possibility of using such a source for studying the spectroscopy and dynamics of solvated biomolecules, DNA base pairs etc. Fragmentation of guanine during the photoionisation process [85] leads to the appearance of relatively small daughter peaks below m=151 amu (m=135 amu and 109 amu corresponding to NH2 and N2CH2 loss, respectively). As always, the ratio of parent to fragmentation signal depends on laser energy, as does the absolute signal magnitude.

4. NON-RESONANT STRONG-FIELD IONIZATION OF MULTIELECTRON SYSTEMS: 1. TRANSITION METAL ATOMS

Multi Active Electron (MAE) dynamics in the Strong-Field Ionization (SFI) of transition metal atoms of the fifth and tenth column of the periodic table are investigated in the adiabatic regime ($\lambda = 1.5$ μm). A kilohertz laser ablation source, based on a dithering laser focus and a rotating and translating metal target rod, in combination with the intensity scan method with a restricted ion collection volume (constant axial intensity focusing geometry) have been employed to obtain for V/Nb/Ta and Ni/Pd : (i) the first charge state saturation intensity; and (ii) the absolute ionization rates for intensities up to 3×10^{14} W/cm^2. A dramatic suppression of ionization of the MAE atoms, compared to Single Active Electron (SAE) theories, is observed. As the origin of the ionization suppression, a dynamic polarization of the system in the laser field is proposed: due to the collective motion of all electrons towards the barrier, the resulting height of the barrier for the tunneling electron is increased. As qualitative theoretical models are presently not available, a simplified but limiting model for the description of strong-field ionization of MAE systems is proposed.

4.1 Introduction

Strong-Field Ionization (SFI) is the key feature in many highly nonlinear processes that are of fundamental importance to chemistry. Chemical applications can be found in sub-femtosecond time resolution in pump-probe experiments to measure *e.g.* electron dynamics, tomography to map molecular orbitals, new methods to obtain structural and dynamical information of molecules, control of complex chemical reactions, etc. The underlying physical processes are: (i) Recollision, where an electron that has been removed will return to the ion under the influence of the laser field. Upon colliding with the ion, it can remove a second electron [12]. This process allows the use of the returning electron as the probe in a time resolved experiment, where the time resolution is now less than half an optical period [13]. Instead of removing a second electron the returning electron can recombine with the ion while the kinetic energy is converted into a photon in the X-ray regime [14]. Using few cycle laser pulses it is in principle possible to generate single attosecond pulses [15]. Also, by measuring the efficiency of the X-ray yield as a function of alignment of a molecule with respect to the laser field, the recombination process can be used as a tomography method. Finally, measuring photoelectron spectra in SFI experiments has led to the discovery of above threshold ionization (ATI) [16]; (ii) Coulomb Explosion Imaging where the fragments of a system that is exploded due to the nuclear repulsion after removal of several electrons are detected [17] to retrieve the structural and dynamical information; (iii) Strong-field Control where using a genetic algorithms to optimize the temporal profile of strong laser pulses, is used to control (complex) chemical processes [18, 19, 20]; and finally (iv) laser ablation where on a macroscopic level, materials can be very precisely machined [21] or the optical parameters inside dielectric materials are modified [22].

To understand the physics of these processes, a detailed understanding of the first ionization step is required. Ionization can be described in two limiting regimes: Multi-Photon Ionization (MPI) and tunnel ionization. In the case of MPI the system absorbs an integer number of photons until the ionization limit is exceeded. On the other hand, tunnel ionization can be understood in terms of a simple picture where the distortion of the field free Coulomb potential by the laser field leads to the formation of a barrier. An electron can classically escape over the top of this barrier or quantum mechanically tunnel through it. To distinguish between the MPI and tunneling regime, the Keldysh parameter (γ) is employed [4]. This (adiabaticity) parameter is defined

as the ratio of the tunneling time ($\tau_{tunneling}$) and the laser period (τ_{laser}), i.e. $\gamma = \tau_{tunneling}/\tau_{laser}$. When $\gamma \gg 1$, tunneling is completely suppressed because the laser field will change direction before the electron can tunnel through the barrier and ionization is dominated by MPI. At the other extreme where $\gamma \ll 1$, the ionization process takes place in the tunneling regime. In this study only the regime where $\gamma < 1$ is considered. Theoretical descriptions of SFI have to take into account the (large) correction to the field free energy levels due to the AC Stark shift. Furthermore, highly nonlinear interactions become more and more important at higher intensities. Perturbation theory becomes inapplicable and different methods have to be employed. The most common approach to describe the ionization in strong laser fields is the single active electron (SAE) approximation. A numerical simulation based on the SAE approximation has shown excellent agreement with the experimental ionization rates of helium [8]. Correlated two-electron phenomena, like non-sequential double ionization in rare gas atoms, can be treated successfully within the SAE approximation by considering the recollision of the continuum electron with the ion [8, 12]. However, recent studies have shown a dramatic failure of SAE theories when applied to Multi Active Electron (MAE) systems, including diatomic molecules [32], conjugated molecules [30, 24, 26, 27], C_{60} [20] and surfaces [31]. The tunneling rates in all of these systems are found to be lower than predicted by SAE theories. Presently, no calculations are available that take all electron interactions during the ionization process into account. To gain more insight in the true nature of the SFI of MAE systems, more experimental data are required. It has been postulated previously that the failure of SAE theories when applied to the above systems will result in the observation of a suppression of ionization relative to theoretical predictions for the following reason [26, 27]: when an MAE system is placed in a strong laser field, not only the tunneling electron, but all electrons will respond to the field. Qualitatively, the effect of the response of all electrons to the laser field is a polarization of the system by a joint motion of all electrons to one side of the potential. The result of this motion of the electrons is a change in the shape of the barrier that the electron has to tunnel through. The response of all electrons results in a boost in the barrier (or a screening of the laser field), leading to suppression of ionization. A full calculation, taking into account all electron correlations, to obtain the true potential of a multi electron system in a strong laser field, is still under development [33, 34]. For systems with a specific symmetry (not generally applicable), a different explanation for the suppression of ionization in terms of

quantum interference has been presented [32, 35, 36]. An effective destructive interference arises between the subwaves of the ejected electron

In this chapter absolute ionization rates of the strong-field ionization of "simple" MAE systems are presented: the transition metal atoms V/Nb/Ta and Ni/Pd. Some initial experimental data on the double ionization of two-electron atoms (Ca and Mg), showing a deviation from SAE theories, are available elsewhere [86, 87]. Unlike noble gases, transition metal atoms have many low lying electronic states and an MAE response to the applied laser field is anticipated. The excellent signal-to-noise ratios of the ion yield as a function of intensity in our experiment allow for the possibility to obtain absolute ionization rates that are directly comparable to theoretical models. This constitutes a major advantage over studies that report relative ionization rates only.

In this chapter it is shown that the experimental ionization rates are much lower than predicted by SAE theories due to the dynamic screening of the local field. Next, a simplified model is presented to obtain an upper limit of the MAE effect: the Zero Range Potential (ZRP). The experimental ionization rates are bracketed between the underestimate of SAE theories and the limiting ZRP model. In the following chapter, results on more complex systems are provided: strong-field ionization of small transition metal clusters [74]. The multi-nuclei nature of these systems introduces many complications that will be discussed carefully. It is shown that for clusters larger than approximately 10 atoms, classical electrodynamics can be used to describe the effect of polarization, and therefore the MAE dynamics, in the strong-field ionization process.

4.2 Method

In this section a general method is presented to obtain saturation intensities for the transition metal atoms and clusters, as well as the more elaborate analysis required to retrieve absolute ionization rates for the atoms. To investigate the ionization mechanism of the MAE systems, the intensity scan method is employed that is described in detail elsewhere [30, 24]. Briefly, a narrow slit, smaller than the Rayleigh range, is placed above the focus perpendicular to the laser propagation direction. In this manner only ions are collected from within a volume of parallel beam geometry and a resulting axial constant intensity. Using a first order rate equation and assuming a Gaussian spatial beam profile ($I_r = I_0 \times \exp -r^2/R^2$ with R as the minimum beam radius and I_0 as the peak

intensity), the ion signal S is obtained as

$$S = \alpha\pi R^2 cl \int_0^\infty \frac{\left(1 - e^{-\int_{-\infty}^{\infty} W(I_r f(t))\mathrm{d}t}\right)}{I_r} \mathrm{d}I_r. \tag{4.1}$$

Here α is the instrument sensitivity, c is the concentration of the neutrals (atoms or clusters), and l is the length of the focal cylinder projected onto the detector. The ionization rate W depends on the (Gaussian) radial intensity I_r and temporal profile $f(t)$. In the high intensity limit, where $e^{-\int_{-\infty}^{\infty} W(I_r f(t))\mathrm{d}t} \ll 1$, the integral over $\mathrm{d}I$ leads to a linear dependence of the ion signal on the logarithm of the intensity. This linear behavior can be written as

$$S = \alpha\pi R^2 cl(\ln I_0 - \ln I_{\mathrm{sat}}). \tag{4.2}$$

The saturation intensity (I_{sat}) is defined by this equation as the intersection of the extrapolated linear behavior and the intensity axis. In order to clarify the meaning of I_{Sat} it is instructive to treat the tractable case of multiphoton ionization with $W = I^n$. In this case it can be shown that at I_{Sat} 43 % of the neutrals are ionized. In the case of an arbitrary ionization mechanism, an unknown but fixed percentage of the neutrals is ionized. The saturation intensity is therefore a first order indication of the "ease" of ionization.

The data obtained with the intensity scan method can be transformed to obtain absolute ionization rates as described elsewhere [26]. Writing the slope in the high-intensity limit ($\alpha\pi R^2 cl$) as β_∞ and at any arbitrary (lower) intensity as β (see figure 4.1), equation 4.2 can be rewritten as

$$\int_{-\infty}^{\infty} W(I_0 f(t))dt = \ln \frac{\beta_\infty}{\beta_\infty - \beta} \tag{4.3}$$

The integral on the left part of this equation represents the integration of the absolute ionization rate over the temporal laser profile. By assuming a specific profile, the absolute ionization rate can be extracted. However, the signal-to-noise ratio of the raw data has to be sufficient to obtain the slope at any given intensity with reasonable confidence. Note that for the extraction of both the saturation intensity as well as the absolute ionization rate, no knowledge relating to any experimental parameter is required.

Finally, the intensity scan method allows for very accurate intensity calibration. Since ADK [7] theory predicts very reliably the ionization rates and saturation intensity of effective SAE systems, measuring the ion yield of e.g. xenon

Fig. 4.1: The data of an intensity scan for our calibration standard xenon are shown, where the ion yield is plotted as a function of the logarithm of the laser peak intensity. A linear dependency at the high intensity limit is found that can be extrapolated to find the saturation intensity at the intersection with the intensity axis. The slope in the high intensity limit (β_∞) as well as the slope at an arbitrary intensity (β) are indicated for use in the extraction of the absolute ionization rates.

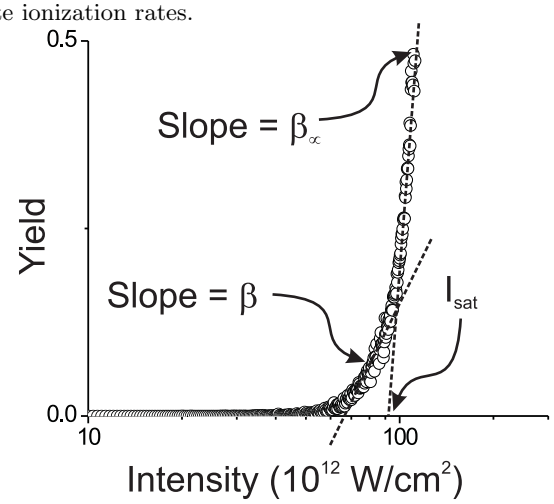

as a function of energy can be used to convert energy into intensity. Without the knowledge of the pulse duration or the focal parameters, the semilogarithmic plot of the ion yield vs. the logarithm of the intensity for the experimental data of the calibration standard (Xe), yields a saturation intensity that can be set to the theoretical value obtained by ADK theory. In this manner absolute intensities within 30 % can be obtained.

To investigate the MAE affects in SFI, transition metal atoms and clusters are chosen as prototype systems. However, these metals cannot be brought into the gas phase with conventional ovens because of the extremely high melting and boiling points. To circumvent this problem, conventional techniques to study metal atoms and clusters in the gas phase employ laser ablation sources that typically operate at 20 Hz. In this study, the ion count rate is very small due to sampling over only a fraction of the Rayleigh range of the laser focus. Therefore, a unique laser ablation source operating at a repetition frequency of 1 kHz was developed. Technical details, including the minimization of the debris formation and clogging of the apertures, are described elsewhere [88]. This source matches

Fig. 4.2: The kHz ablation source consisted of three separate regions pumped by a Roots blower, a diffusion pump and a turbomolecular pump (panel a). From the source region the molecular beam entered the second region via a 1mm skimmer, where residual ions were removed by two deflection plates. The interaction region contained a Wiley-McLaren mass spectrometer, deflection plates to compensate for large lab-frame velocities in the molecular beam, and the narrow slit to collect ions only from within a fraction of the Rayleigh range of the focus (left panel). Using a dithering 30 cm lens, laser pulses at 1 kHz were focused onto a rotating and translating metal rod. This rod was housed in a modified Smalley-type cluster source and was mounted via a hex key into a threaded shaft. Using an external stepper motor and a rotary motion feedthrough, the shaft was rotated in an internally threaded block and therefore moved up or down depending on the direction of rotation. The carrier gas flowed through the same tube in the same direction as the incoming laser light, avoiding clusters to move towards the laser window (enlargement in panel b).

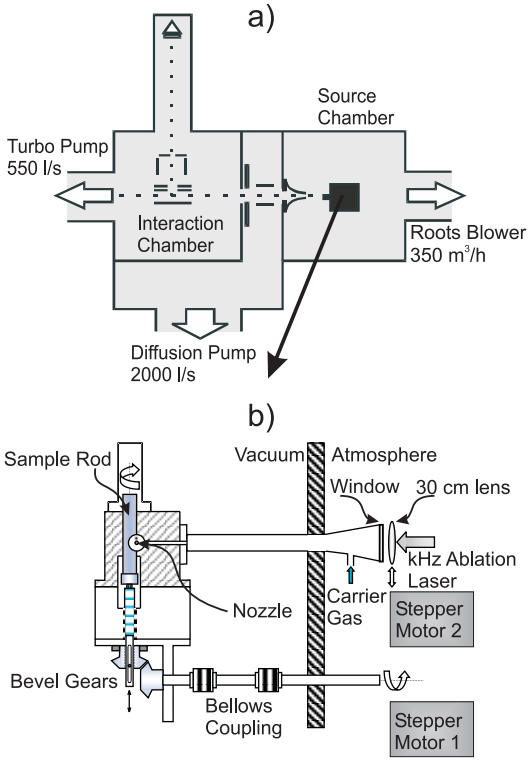

the repetition frequency of the amplified femtosecond laser system and increases the count rate by a factor of 50 or more. An additional advantage of a kHz source is the reduced formation of oxides and carbides. The formation rates of oxides and carbides are the same as in conventional sources, but the ablation rate is 50 times faster yielding a lower percentage of oxides and carbides per laser shot. Due to the high repetition rate, a continuous flow of the buffer gas (He) is employed for hydrodynamic transport of the atoms and clusters. The gas flow, that was propagating in the same direction as the incoming laser beam and that used the same inlet tube (25 cm in length) prevented clusters from moving back to coat the laser window. In the lower panel of figure 4.2 the details of the source design are shown. The light of an arc lamp pumped Nd:YLF laser (Positive Light Merlin), synchronized with the femtosecond laser system and with pulses of $>$ 10 mJ/150 ns/527 nm, was focused with $f/15$ optics onto a translating and rotating vanadium, niobium, tantalum, nickel or palladium cylindrical rod (Goodfellow) of 6 mm in diameter and $\sim$ 3 cm in length. Depending on the ablation mechanism of the specific metal, the energy was reduced to compromise between ablation rate and stability. A Smalley-type source holder was modified to allow for easy adjustment, containing a separate insert with the nozzle and growth channel. The insert was made out of a base (stainless steel) and a glass tube (2 mm diameter and 1 to 3 cm length) that functions as a growth channel to change the cluster size distribution. An external stepper motor and a rotary motion feed through were used to rotate and translate the sample rod that was mounted on a screw drive mechanism. To avoid thread formation or uneven exposure, decoupling of the rotation and up-and-down movement was necessary by dithering the laser focus with a $\sim$ 0.1 Hz period and a $\sim$ 1 mm amplitude of travel. In this study, the source conditions were optimized to favor the production of atoms instead of clusters by: lowering the pressure in the growth channel to the minimum flow of 800 sccm (lower flow conditions lead to unstable operation); minimizing the length of the growth channel to $<$ 1 cm (restricted by the physical geometry of the apparatus); shortening the time delay between the laser pulse used for ablation and the laser pulse used for the ionization process (depending on the exact source conditions around 300 μs); and lowering the deflection voltage (depending on the source and mass of the metal around 20 V).

Our vacuum setup is presented in the top panel of figure 4.2 and shows three differentially pumped regions. The regions were pumped by respectively an Edwards mechanical Roots blower (EH500A, 350 m^3/h), an Edwards diffu-

sion pump (Diffstak 250, 2000 l/s) and a Varian turbomolecular pump (V550, 550 l/s). During operation with maximum gas inlet, the pressures in the three regions were respectively $< 10^{-1}$ Torr, $< 10^{-4}$ Torr and $< 10^{-6}$ Torr, whereas the base pressure in the third region was below 5×10^{-8} Torr. The second and third region were isolated by an NRC-design low-profile gate valve. The first region, the source chamber, housed the cluster source. After the 1 mm skimmer (Beam Dynamics) the molecular beam entered the second region where any residual ions were removed from the molecular beam by two deflection plates. The final region contained a dual slope Wiley-Mclaren time-of-flight mass spectrometer. Compensation for any potentially large lab-frame molecular beam velocities in the 50 cm long flight tube was achieved by two deflection plates ($\Delta V = 0 - 150$V), mounted directly on top of the last attractor plate. In this manner, ions produced in the molecular beam are favored over background signal with an arbitrary velocity component and a virtual background free mass spectrum can be obtained. A narrow slit was placed directly on top of these deflection plates, allowing to collect ions from within a parallel beam axial symmetric focal volume only. Ions were detected using a double stack microchannel plate (Burle) detector, where the signal was fed directly into a pulse amplifier (Phillips Scientific 6950) and discriminator (Phillips Scientific 6915). Mass spectra were recorded using a standalone multichannel scaler (Stanford Research RS430) with a minimum bin width of 5 ns, but to operate at 1 kHz normally set to bin widths of 40 or 160 ns. During the intensity scans, ion counts were recorded using a computer-based PCI multichannel scaler (FastComtec P7888), with a bin width of 500 ps. Every individual laser shot, all the hits were transferred to the computer and count rates for a specific intensity were obtained by integration over a preset gate. Although a maximum of about thirty hits per laser shot could in principle be transferred to the computer at a repetition frequency of 1 kHz, the count rates in our scans were significantly lower (up to 0.1 count per laser shot).

The amplified femtosecond laser system, used in this experiment, is discussed in detail elsewhere [72]. Briefly, the 800 nm pulses of a fs Ti:Sapphire (Spectra-Physics Lok-to-Clok Tsunami) were first regeneratively amplified (Positive Light Spitfire) using a diode-pumped Nd:YLF laser (Positive Light Evolution 30). Next, the pulses were passed through a two-pass linear Ti:Sapphire amplifier pumped by another Nd:YLF laser (Positive Light Evolution 30). The recompressed, transform-limited 80 fs/2.7 mJ pulses were used to pump an Optical parametric amplifier (Quantronix/LightConversion TOPAS) to produce 1.5

Fig. 4.3: The energy of the laser light was varied using a neutral density filter wheel and was focused with $f/15$ up to a maximum intensity of 3×10^{14} W/cm^2. Each laser shot, a mass spectrum was recorded and the energy of the laser pulse was measured by an InGaAs photodiode and written as a time delay at the end of the mass spectrum.

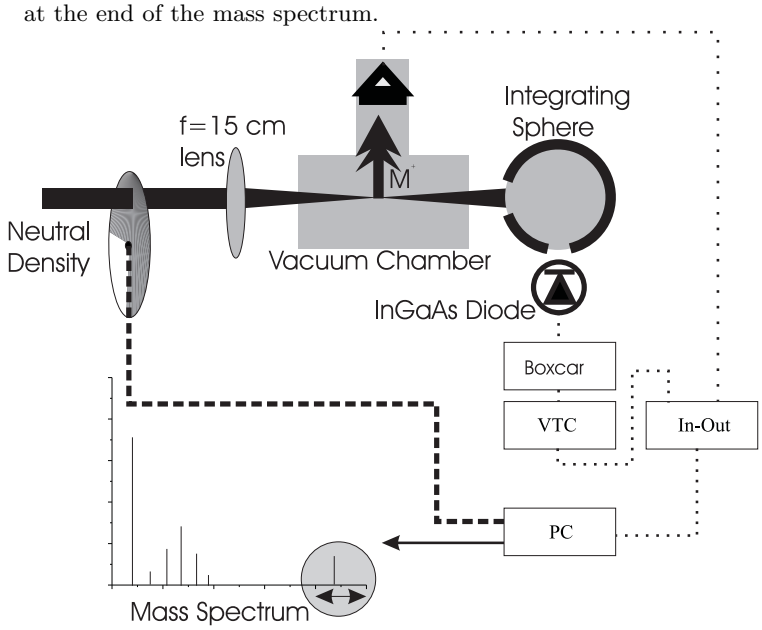

μm/150 μJ/90 fs pulses for the SFI experiment. The laser energy was varied using a neutral density filter wheel, controlled by the data acquisition computer (see figure 4.3). The energy of each laser shot was recorded using an integrating sphere and an InGaAs photodiode. In our intensity scan method it is of utmost importance to correlate for every laser shot the mass spectrum to the corresponding laser energy/intensity. Hereto a voltage to time converter to write the energy of the laser pulse as a time delay at the end of the mass spectrum was developed.

4.3 Results

The raw data of our intensity scans for V/Nb/Ta and Ni/Pd are displayed in figure 4.4. The ion yield is plotted as a function of the logarithm of the laser peak intensity. A least-square-error linear fit to the the high intensity data (dashed line) was used to obtain I_{sat} at the intersection of the linear fit and the

Fig. 4.4: Typical data from the intensity scans are shown in a semi-logarithmic plot for V/Nb/Ta and Ni/Pd. The saturation intensities are indicated at the intersection of the extrapolated linear data in the high intensity limit and the intensity axis.

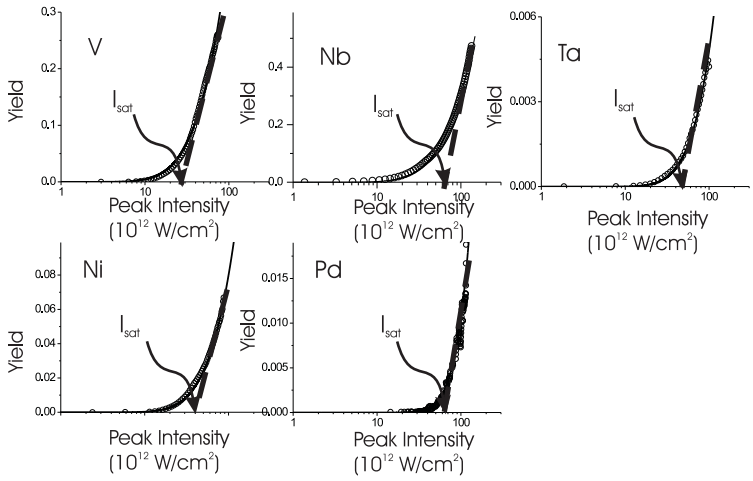

Tab. 4.1: Experimental saturation intensities and the corresponding values for both ADK and ZRP models are given for V, Nb, Ta and Ni, Pd. The value η is an indication of the contribution of MAE effects (see text). For reference, the electronic configurations, ionization potentials [89] and static polarizabilities [75] are given.

Atom	Configuration	IP	α	I_{sat} (10^{13} W/cm^2)			η
		(eV)	Å^3	Exp	ADK	ZRP	(%)
V	[Ar] $3d^3 4s^2$	6.75	12.4	3.2	1.2	12.2	18
Nb	[Kr] $4d^4 5s^1$	6.76	15.7	6.7	1.2	12.2	50
Ta	[Xe] $4f^{14} 5d^3 6s^2$	7.89	13.1	5.4	2.1	18.4	20
Ni	[Ar] $3d^8 4s^2$	7.6	6.8	4.7	1.8	16.7	19
Pd	[Kr] $4d^{10}$	8.34	4.8	6.2	2.6	21.3	19
Xe	[Kr] $4d^{10} 5s^2 5p^6$	12.13	4	9.5	9.5	57.6	0

intensity axis. The solid line is a convenient exponential fit to the data at all intensities that is later used alternatively to obtain absolute ionization rates. A series of four or more measurements was used to obtain the standard deviation of I_{sat}. Taking into account the standard deviation of I_{sat} of our calibration standard xenon, the total standard deviation was estimated to be less than 20 %.

Fig. 4.5: Absolute ionization rates are shown for V/Nb/Ta and Ni/Pd, extracted from the data in figure 4.4 (open circles). The solid line represents the accurate ionization rate obtained using the exponential fit of the same data as in figure 4.4. The dashed (*vide infra*: ADK) and dotted (*vide infra*: ZRP) line are theoretical rates.

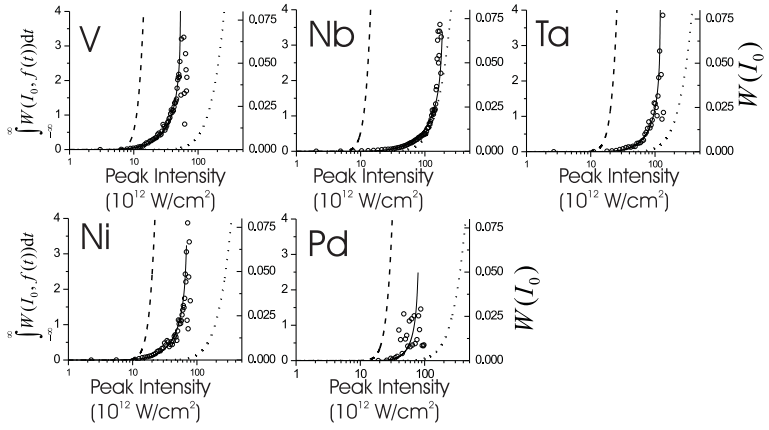

For all metal atoms, I_{sat} is presented in table 4.3 together with the previously reported ionization potential (IP) [89], polarizability (α) [75] and theoretical predictions (*vide infra*: ADK, ZRP, η). Next, the raw data in figure 4.4 were smoothed with a 10 point binning method in order to evaluate within reliable accuracy both the slope in the high intensity limit as well as the slopes at all lower intensities. The three-point differential method was employed to obtain the different slopes: the slope at any given intensity was calculated from the rise and run over its two neighboring points. The time integrated ionization rate $\int_{-\infty}^{\infty} W \mathrm{d}t$ is obtained using equation 4.3. The results for V/Nb/Ta and Ni/Pd are displayed in figure 4.5, where on the left ordinate the integrated ionization rate($\int_{-\infty}^{\infty} W(I_0 f(t))dt$) is plotted. On the right ordinate the absolute ionization rate ($W(I_0)$) is plotted, assuming a square temporal profile pulse of 50 fs as obtained by a fit of the experimental ionization rates of xenon to ADK theory. The solid lines in figure 4.5 represent the same transformation of equation 4.3, but using the data from the exponential fit instead of the experimental data. For comparison, theoretical ionization rates have been added to figure 4.5 as dotted and dashed lines (*vide infra*: ADK and ZRP).

4.4 Discussion

In order to discuss the MAE nature of the strong-field ionization of the transition metal atoms V/Nb/Ta and Ni/Pd, the experimental data are compared to a SAE theory (ADK) and a simplified but limiting MAE model (Zero Range Potential: ZRP).

Both models operate in the tunneling regime, where the tunneling time ($\tau_{tunneling}$) is longer than the laser period (τ_{laser}), i.e. $\gamma = \tau_{tunneling}/\tau_{laser} < 1$. Care has been taken that around the experimentally measured saturation intensities, ionization takes place in this regime. Hereto, the laser wavelength is chosen in the infrared at 1.5 μm. Next, the possibility of a contribution to the atoms signal of fragmented clusters is considered. However, dissociation after ionization of clusters of size n into smaller fragments (atoms) can be ruled out due to the very high dissociation energy of transition metal clusters (typically higher than the IP). This is furthermore verified in the case of niobium by recording a mass spectrum with a soft one-photon ionization process using ArF radiation. Contributions from doubly or higher charge states (z) of larger clusters with the ratio $n/z = 1$ (e.g. Ni_2^{2+}) to the atom signal can be neglected as argued in chapter 5 of this thesis, where typical mass spectra for the cluster distributions (under different source conditions) are shown and discussed in detail.

The first model that is naively applied, is a SAE theory to calculate I_{sat} for the transition metal atoms. ADK theory [7] is often considered the benchmark for the lower limit of the ionization rates, i.e. an upper limit of I_{sat}. The expression for the ionisation rate W in terms of the electric field strength E is given by

$$W = \omega_A C_{nl}^2 f(l,m) IP \left(\frac{3E}{\pi(2IP)^{3/2}}\right)^{1/2} \left[\frac{2}{E}(2IP)^{3/2}\right]^{2n-|m|-1} \times \\ \times \exp\left[-\frac{2}{3E}(2IP)^{3/2}\right] \qquad (4.4)$$

where n, l and m are the conventional quantum numbers, ω_A is the atomic unit of frequency, and the factors f and C are given by

$$f(l,m) = \frac{(2l+1)(l+|m|)!}{2^{|m|}(|M|)!(l-|M|)!} \\ C_{n,l} = \left(\frac{2e}{n}\right)^n \frac{1}{(2\pi n)^{1/2}}. \qquad (4.5)$$

Theoretical saturation intensities using ADK theory (ADK:I_{sat}) have been

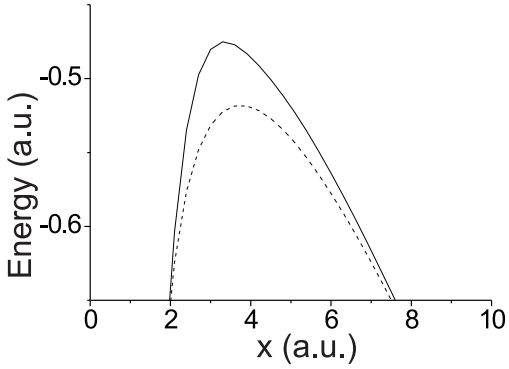

Fig. 4.6: A 4-electron, one-dimensional model atom, with ionization potential $IP = 0.5$ a.u. and polarizability $\alpha = 30$ $\mathring{A}^3$, in a strong laser field. Laser parameters: wavelength 1000 nm, peak intensity $2 \cdot 10^{14}$ W/cm^2, pulse duration 10 fs. The lines represent the potential barrier experienced by the tunneling electron at the laser pulse peak. To demonstrate the effect of polarizability on tunnel ionization the potential is calculated in two different ways. Full/dotted line: potential of the 4-electron system in the presence/absence of the laser field plus the potential due to the laser field. The difference between the two lines represents the potential caused by the laser induced polarization of the bound electrons. The potentials were calculated from the solution of the 4-electron Schrödinger equation by using the multi-configuration time dependent Hartree Fock approach. For more information see references [33] and [90].

added to table 4.3. For the metal atoms V/Nb/Ta an s-electron is being removed during the ionization process and the orbital angular momentum $l = 0$ can be used in the calculations. In the case of Ni/Pd a d-electron is being removed ($l = 2$) and therefore I_{sat} has to be averaged for $m = -2 \cdots 2$. All values for I_{sat} are significantly smaller than the experimental values, clearly demonstrating the failure of SAE theories: the MAE nature of transition metal atoms suppresses ionization. Since I_{sat} is a nonlinear parameter, a small deviation from the experimental saturation intensity results in a much larger discrepancy in the ionization rate. We propose that this suppression of ionization in MAE systems is due to the joint motion of all electrons induced by the laser field. The effect is a polarization of the system that increases the barrier for the tunneling electron by repulsion or equivalently screens the laser field.

Although the exact ab initio analysis of multi-electron atoms in strong laser fields is still out of reach, recently a multi-configuration time dependent Hartree Fock (MCTDHF) approach has been carried out in a collaboration that can treat the non-perturbative dynamics in correlated, few-electron systems [33, 90]. Currently, MCTDHF can handle the dynamics of up to 10 electrons in one dimension. Generalization of this method to two and three dimensions is under progress. In figure 4.6 the main mechanism for the reduction of tunnel ionization is identified. We have solved the Schrödinger equation for a 4-electron one-dimensional model atom in a strong laser field by using the MCTDHF method. The laser wavelength is 1000 nm, and the laser peak intensity is $2 \cdot 10^{14}$ W/cm^2. The ionization potential of the valence electron is $IP = 0.5$ a.u., and the polarizability is $\alpha = 30$ $\mathring{A}^3$. A one-dimensional solution of the Schrödinger equation requires shielding of the electron-electron and electron-nucleus interaction. The shielding parameters were adjusted to realize polarizabilities and ionization potentials as close as possible to experimental values. In general, a one-dimensional calculation tends to overestimate the polarizability. Therefore, the ionization potential was chosen slightly larger than the experimental values in order to avoid unreasonably high polarizabilities. The full and dotted lines in figure 4.6 show the potential barrier experienced by the tunneling electron at the peak of the laser field. The full line depicts the potential of the polarized atom plus the potential due to the laser field, whereas the dotted line shows the potential of the field free atom plus the potential due to the laser field. We find that the presence of the laser field shifts the bound electrons and creates a polarization which changes the potential barrier of the atom. The difference between the two lines in figure 4.6 represents the change of the potential caused by the polarization of the atom. As the electrons are pushed in the direction of the laser field, the polarization increases the tunneling barrier and therewith reduces ionization, as was also shown for molecular systems [90]. The MCTDHF analysis corroborates the conclusion derived from figure 4.5 that ADK theory overestimates tunnel ionization in complex atoms. The largest part of the overestimation comes from the fact that complex atoms have a large polarizability which reduces tunnel ionization. A smaller part can also come from the fact that ionization in transition metal atoms takes place in the above barrier ionization (ABI) regime. In the limit of ABI the laser field deforms the tunneling barrier to such an extent that the barrier is completely suppressed and the electron can escape over the barrier. ADK theory is known to overestimate tunnel ionization in the above barrier ionization regime. In Helium ADK and ABI rates differ by

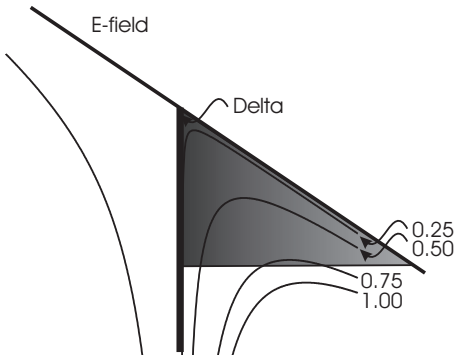

Fig. 4.7: The effect of the MAE dynamic response can be mimicked by an effective Coulomb potential in the laser field. The applied field will push the electrons to the downfield side of the potential, resulting in a screening of the core for the tunneling electron (a reduction in z). In the extreme case, the resulting potential resembles a Zero Range Potential (ZRP). The different values for z shown in the figure are 1.00, 0.75, 0.25 and 0.01. For clarity the resulting triangular barrier from the ZRP is shown in grey

up to a factor of 3 [91]. As there exists no theory of ABI, comparison of experiment and ADK theory gives an upper estimate of the polarization induced reduction of ionization.

As the second model, a simplified but limiting model is used. The result of the joint motion of all electrons is an additional dynamic screening of the ionic core. The potential that the tunneling electron feels can therefore be approached by an effective Coulomb potential. The displacement of the electron cloud relative to the nucleus due to the laser interaction, will lead to an additional dynamic screening of the core. In figure 4.7 the effect of reducing the charge z of a Coulomb potential in the presence of a laser field is shown. In the limiting case of full screening ($z \to 0$), this potential approaches the Zero Range Potential (ZRP). The theoretical ionisation rates are calculated using the cycle-averaged Wentzel-Kramer-Brillouin tunneling rates out of a ZRP

$$W(I) = 1/\pi \sqrt{\frac{2\pi E}{2/3(2IP)^{3/2}}} \frac{E}{2(2IP)^{1/2}} \exp \frac{-2(2IP)^{3/2}}{3E} \tag{4.6}$$

and the calculated I_{sat} are shown in table 4.3 as well.

Finally we propose to bracket the MAE character of the ionization process

by the following property (η).

$$\eta = \frac{I_{sat}(\text{Exp}) - I_{sat}(\text{ADK})}{I_{sat}(\text{Delta}) - I_{sat}(\text{ADK})} \times 100 \tag{4.7}$$

This nonlinear parameter is 0% (or lower) for pure SAE systems and can increase to the limiting value of 100% with increasing MAE contributions. As anticipated, due to the the MAE nature of transition metal atoms, η deviates strongly from zero for all tested atoms (see table 4.3). However, it is surprising to notice that except for niobium, all values for η are around 20 %, independent of the number of valence electrons or polarizabilities. In the case of niobium, a much larger contribution from MAE effects is found as $\eta = 50\%$.

Theoretical ionization rates have been added to figure 4.5: ADK (dashed line) and ZRP (dotted line). The same effects as described above are observed. ADK theory overestimates and the limiting case of the ZRP approach underestimates the ionization rates of transition metal atoms. At this point it is instructive to estimate the failure of SAE theories when applied to transition metal atoms. First the experimental ionization rate is obtained at ADK:I_{sat}. At this intensity the experimentally measured ionization rate is extremely small and our method is not suitable to extract a reliable rate. Instead, we fit the experimental data to ADK rates obtained with an arbitrary (larger) IP. The rate obtained from the fitted data is off by a factor off 10^4 relative to the ADK rate with the experimental IP. This clearly shows the failure of SAE theories to predict I_{sat} as shown in table 4.3.

4.5 Conclusion and Future Directions

A dramatic failure of SAE theories (e.g. ADK) when applied to transition metal atoms is found (experimental rates can be lower by a factor of 10^4). Presently, MAE theories taking into account all electron interactions during a strong-field ionization process are still under development. Qualitatively, the origin of the suppression of ionization is argued to result from a joint motion of all electrons in the laser field, i.e. a polarization of the system. The increased repulsion of the higher electron density near the barrier reduces the tunneling rates. A simplified but limiting MAE model is proposed in terms of a Zero Range Potential. The saturation intensities and absolute ionization rates are measured for V/Nb/Ta and Ni/Pd. A single parameter to indicate the MAE character of the ionization process of the atoms is provided. Except for niobium, the

MAE contribution is approximately the same for all tested metals, irrespective of the number of valence electrons or the polarizability. An anomalously high MAE contribution for niobium is found. The strong deviation of the behavior of niobium is currently under further investigation in our laboratory, but several indications of anomalous behavior of niobium atoms and clusters have been described in the literature (including extremely large polarizabilities of niobium clusters) [92, 93]. The experimental technique described in this study can be applied to many systems not accessible with conventional sources, yielding more data to gain full insight in MAE dynamics during the strong-field ionization process of relatively simple systems (atoms) and providing a more extensive background for the anomalous behavior of niobium.

5. NON-RESONANT STRONG-FIELD IONIZATION OF MULTIELECTRON SYSTEMS: 2. TRANSITION METAL CLUSTERS

Metal clusters are adopted as prototype systems to study multi-electron effects in Strong-Field Ionization (SFI) and the transition from the quantum mechanical description of small systems to a classical behavior for larger systems. The saturation intensities of the first ionization step are reported for the clusters V_n (n=1-12), Nb_n (n=1-15), Ta_n (n=1-12) and Ni_n (n=1-12), as well as the saturation intensities of the second ionization step for the clusters V_n (odd n=13-23), Ta_n (odd n=9-17) and Ni_n (odd n=15-35 and even n=26-36). It is shown that the tunneling rates predicted by single active electron theories can be off by a factor of $10^4 - 10^6$. The smallest clusters behave like quantum systems and their response to a strong laser field is compared to that of a system with a zero range potential. A classical model that takes into account the multi-electron response by a static polarization term, starts to converge to the experimental results for $n > 10$ for V_n, Ta_n and Ni_n. Niobium custers show anomalous behavior that might be ascribed to the failure of classical models to account for the polarizabilities that vary significantly as a function of size, as measured in niobium clusters.

5.1 Introduction

In chapter 4 of this thesis the importance of strong-field ionization (SFI) to chemistry was briefly discussed [94], with emphasis on the highly nonlinear processes of Recollision, Coulomb Explosion Imaging, Strong-field Control and Laser Ablation/Optical Modification. The physics of ionization in all these processes can be well described using e.g. ADK theory [7], if a Single Active Electron (SAE) response can be assumed. The naive application of SAE theories to Multi Active Electron (MAE) systems, including diatomic molecules [32], conjugated molecules [30, 24, 26, 27], C_{60} [20] and surfaces [31] has shown a large overestimation of ionization rates. The origin of this suppression of ionization relative to SAE theories is ascribed to joint motion of all electrons towards the lower part of the potential: a *dynamic polarization*. The tunneling electron now experiences additional repulsion, or equivalently, the height of the barrier that the electron has to tunnel through is increased effectively by the higher density of electrons near the barrier. In chapter 4 of this thesis [94], "simple" Multi Active Electron (MAE) systems were studied: transition metal atoms. Saturation intensities and absolute ionization rates were obtained that can be compared directly to theoretical models. In this part, more complex MAE systems are investigated by studying the strong-field ionization behavior of small metal clusters of V/Nb/Ta and Ni. The introduction of multiple nuclei leads to many complications in the description of strong-field ionization, including (i) the larger effect on the suppression of the barrier by the laser field due to the extended width of the potential. A modification of the Keldysh parameter has been proposed to compensate for this effect[25]; (ii) the non-adiabatic response of electrons due to the higher density of states in extended systems [26, 27]; (iii) the motion of the nuclei during that laser pulse leading to Enhanced Ionization at a critical separation of the nuclei [28]; and (iv) the drop of the plasmon frequency due to the expansion of an atomic cluster where several electrons have been removed, leading to the production of highly charged ions when the plasmon frequency matches the laser frequency (Plasmon Resonance) [29].

By choosing to study metal clusters of varying size and by carefully selecting the laser parameters (wavelength, pulse duration and intensity), it is possible to study exclusively the effect of polarization during the strong-field ionization process. The first quantitative model to describe the effect of polarizability was recently communicated for C_{60} [20]. This molecule is modeled as a conducting sphere and classical electrodynamics are used to obtain the potential in a strong

laser field. Classical models can be used to predict correctly the polarizability and ionization potentials of the higher charge states of C_{60}. The MAE effect in the SFI process is taken into account by a single polarizability term, yielding an effective MAE theory with (still) only one active electron. The agreement of this classical model with the experimental strong-field ionization results is excellent. On the other hand, small quantum systems like MAE atoms cannot be treated by classical models as we have shown in an earlier communication [95]. Since a full multi-body calculation is presently not available, a model that assumes perfect screening was employed as a limiting case to describe the SFI of small quantum systems like atoms. We investigated when the transition from small quantum to classical systems takes place and how the physics of the quantum systems differs from the classical picture. Hereto, a prototype system with many electrons and varying size is used: (transition) metal clusters. Additional advantages of these systems are: (i) the high dissociation energy that makes the interpretation of the mass spectrum unambiguous; (ii) the heavy nuclei that will hardly move (if singly charged) during the short laser pulse, thus avoiding complications like enhanced ionization and plasmon resonances; (iii) the property to form congregations of atoms that resemble spheres to rule out alignment effects and allow for simple classical models; and (iv) the availability of the relevant experimental data, like ionization potentials (IP) and in some cases also the polarizabilities (α). The suppression of ionization relative to SAE theories for these systems is observed, and can be quantitatively understood for the larger clusters. As is the case in C_{60}, the strong-field ionization of larger metal clusters can be described as a classical process [20]. The physics of the smaller systems is similar, but for quantitative agreement full multi-body numerical simulations have to be developed.

5.2 Method

The experimental technique to obtain the saturation intensities of the V/Nb/Ta and Ni clusters is detailed in chapters 3 and 4. Briefly, the transition metal cluster beam was generated using a stable kHz rate laser ablation source [88]. Using a dithering focus, the light of a 1 kHz Nd:YLF laser was focused on to the rotating and translating target metal rod, ensuring even exposure and minimizing debris formation. An amplified femtosecond laser system, described elsewhere [72], pumped an optical parametric amplifier (OPA) of which the signal at 1.5 μm was used for ionization. The energy was varied using a neutral density filter

wheel, allowing to scan up to a maximum intensity of 3×10^{14} W/cm^2. Ion yields were recorded using a multichannel scaler card and stored in a PC. The intensity scan method, based on a restricted parallel axially symmetric focusing geometry as described elsewhere [30], was used to extract the saturation intensities (I_{sat}). The quantity I_{sat} corresponds to a fixed percentage (the exact number depends on the ionization mechanism) of ionized neutrals and is a measure of the "ease" of ionization. It is independent of experimental parameters, including apparatus sensitivity, concentration of neutrals in the molecular beam and focal geometry.

5.3 Results

The combination of a kHz laser ablation source and the intensity scan method allows for a systematic investigation of the strong-field ionization mechanism of many atoms and atomic clusters not available from conventional sources. The strong-field ionization at 1.5 μm was initially investigated for metal clusters from two columns in the periodic table: niobium (column 5) and nickel (column 10). The reason for the choice of these original two metals is the availability of experimental data, most importantly ionization potentials [96, 97] and polarizabilities (related to the multi electron screening effect) [93, 98]. Both experimental and theoretical studies are available of low-lying electronic states [99, 100, 101, 102, 103] and geometries [104, 105]. Although a few electronic states below the photon energy of 1.5 μm have been predicted theoretically for some clusters of these metals, experimental absorption spectra show extremely small dipole coupling to these states. All absorption spectra show a large plasmon resonance in the UV range with a long tail into the near IR. At the wavelength of 1.5 μm (as used here), these experimental studies show only very little absorption and an adiabatic electronic response is assumed throughout this study. For the larger clusters, the geometrical studies show a compact packing symmetry that closely resembles a sphere, avoiding problems due to alignment and allowing the application of very simple classical models. Because the niobium results differ significantly from those of nickel (*vide infra*), additional results are presented for niobium at 800 nm. Furthermore, to check if the different behavior is a property of the early transition metals, the two neighboring metals in the fifth column are also investigated: vanadium and tantalum.

Nickel The results for nickel, the first row element in the 10th column

Fig. 5.1: The mass spectrum for Nickel is shown in panel (a) as a function of the number of atoms n divided by the charge state z. Peaks at half integer n/z indicate doubly charged clusters of an odd number of atoms. Doubly charged clusters of an even number of atoms per cluster coincide with singly charged clusters. Assuming a smooth cluster distribution, contributions from these doubly charged clusters can be estimated by extrapolating the neighboring peaks of doubly charged clusters of an odd number of atoms per cluster. As an example, an intensity scan is shown in panel (b) for Ni_7, where the contribution from the Ni_{14}^{2+} signal is subtracted. The saturation intensity I_{Sat} is found by fitting a line (gray solid line) to the high intensity data and finding the intersection of this line with the intensity axis (see arrow). Errors are estimated by a worst-case fits to the data (gray dashed line). Experimental saturation intensities, including error bars are shown in panel (c) for the first ionization step (solid squares) and (d) for the second ionization step (solid circles). Two classical models are included: CSM, where the laser induced polarizability is neglected (dashed line) and CSM where the dynamic multi-electron polarizability is included (solid line). Also a limiting theory based on the Zero Range Potential (dotted line) is included.

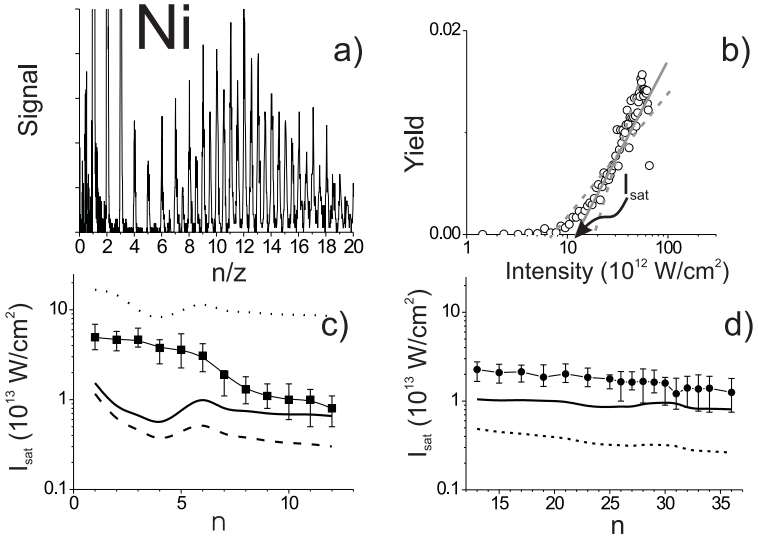

of the periodic table, have recently been communicated elsewhere [74]. The electronic ground state of the atom is $[Ar]3d^8 4s^2$, giving a total of ten valence electrons. At maximum laser intensity ($\sim 10^{14}$ W/cm^2), a mass spectrum of nickel clusters as shown in figure 5.1a is obtained in a few seconds with mod-

Tab. 5.1: Experimental (Exp) and theoretical (CSM) saturation intensities for the first ionization step are presented for vanadium, niobium, tantalum and nickel. Ionization potentials are added for reference purposes together with the electronic configurations and radii of the atoms.

	V [Ar] $3d^3 4s^2$ R=1.35			Nb [Kr] $4d^4 5s^1$ R=1.45			Ta [Xe] $4f^{14} 5d^3 6s^2$ R=1.45			Ni [Ar] $3d^8 4s^2$ R=1.35		
	IP	$I_{sat}/10^{13}$		IP	$I_{sat}/10^{13}$		IP	$I_{sat}/10^{13}$		IP	$I_{sat}/10^{13}$	
	(eV)	(W/cm^2)		(eV)	(W/cm^2)		(eV)	(W/cm^2)		(eV)	(W/cm^2)	
N		EXP	CSM		EXP	CSM		EXP	CSM		EXP	CSM
1	6.8	3.2	1.0	6.8	6.7	0.9	7.9	5.4	1.8	7.6	4.7	1.5
2	6.4	3.1	0.8	6.2	6.6	0.7	6.0	5.1	0.6	7.4	4.7	1.0
3	5.5	2.9	0.5	5.8	6.0	0.5	5.6	3.6	0.5	6.2	4.7	0.7
4	5.7	2.8	0.5	5.6	5.9	0.5	5.8	2.4	0.5	5.7	3.8	0.5
5	5.5	2.5	0.5	5.5	5.1	0.4	5.2	1.5	0.4	6.2	3.6	0.8
6	5.4	2.5	0.4	5.4	5.1	0.4	5.1	1.3	0.3	6.8	3.1	1.1
7	5.2	1.7	0.4	5.4	5.1	0.4	5.2	1.1	0.4	6.2	1.9	0.8
8	5.4	1.5	0.5	5.5	4.8	0.5	5.2	0.8	0.4	6.2	1.3	0.8
9	5.2	1.5	0.4	5.2	3.7	0.4	5.1	0.7	0.3	6.0	1.1	0.7
10	5.2	1.5	0.4	5.5	4.3	0.5	5.1	0.8	0.4	6.0	1.0	0.7
11	5.0	1.5	0.3	4.7	3.6	0.3	4.9	0.8	0.3	6.0	1.0	0.7
12	4.9	1.3	0.3	5.2	3.6	0.4	4.9	0.7	0.3	5.9	0.8	0.7
13				4.9	3.6	0.3						
14				4.8	4.1	0.3						
15				4.5	3.7	0.2						

erate laser pulse energies for ablation (5 mJ). Nickel occurs naturally with two dominant isotopes: ^{58}Ni (68%) and ^{60}Ni (26%). The bin width of the external scaler was set to 40 ns, but scans at higher resolution have been used to show that the contributions from carbides, nitrites and oxides to the cluster signal are below a few percent for all tested metals. The mass spectrum is plotted as a function of cluster size n divided by the charge z and is the result of the cluster size distribution and the mass spectrometer transmission function. The transmission depends on the voltage setting of the deflection plates and the ratio n/z. Overall, the form of the mass spectrum is explained by a transmission function centered at $n/z = 12$ (much larger clusters can therefore not be detected), combined with a typical bimodal cluster distribution, peaking at the atom and $n \sim 30$. The peaks in the mass spectrum at half integer values of

Tab. 5.2: Experimental (Exp) and theoretical (CSM) saturation intensities for the second ionization step are presented for vanadium, niobium, tantalum and nickel. Ionization potentials are estimated using equation 5.3. No double ionization occurs within the measured intensity regime for niobium.

	V [Ar] $3d^3 4s^2$ R=1.35			Nb [Kr] $4d^4 5s^1$ R=1.45			Ta [Xe] $4f^{14} 5d^3 6s^2$ R=1.45			Ni [Ar] $3d^8 4s^2$ R=1.35		
	IP	$I_{sat}/10^{13}$		IP	$I_{sat}/10^{13}$		IP	$I_{sat}/10^{13}$		IP	$I_{sat}/10^{13}$	
	(eV)	(W/cm^2)		(eV)	(W/cm^2)		(eV)	(W/cm^2)		(eV)	(W/cm^2)	
N		EXP	CSM		EXP	CSM		EXP	CSM		EXP	CSM
9							8.2	2.5	0.7			
11							7.9	2.0	0.6			
13	7.2	2.9	0.5	7.6	> 10	0.5	7.4	1.8	0.5	8.8	2.3	1.0
15	6.9	2.7	0.4	7.2	> 10	0.4	7.3	1.7	0.5	8.6	2.1	1.0
17	7.1	2.8	0.5	7.2	> 10	0.5	7.5	1.5	0.6	8.6	2.1	1.0
19	6.7	2.9	0.4	7.1	> 10	0.4				8.5	1.9	1.0
21	6.6	2.8	0.4	7.0	> 10	0.4				8.4	2.0	1.0
23	6.6	2.8	0.4	7.0	> 10	0.4				8.1	1.9	0.9
25				6.9	> 10	0.4				8.1	1.8	0.9
26				6.9	> 10	0.4				8.1	1.7	0.9
27										8.0	1.6	0.9
28										8.1	1.7	0.9
29										8.2	1.6	1.0
30										8.1	1.6	1.0
31										8.1	1.2	1.0
32										7.9	1.4	0.8
33										7.8	1.4	0.8
34										7.8	1.4	0.8
36										7.8	1.3	0.8

n/z result from doubly charged clusters of odd n, e.g. Ni_{15}^{2+} is shown in the mass spectrum at $15/2 = 7.5$. Doubly charged clusters of even n coincide in the mass spectrum with singly charged clusters, but assuming a smooth cluster distribution, the contribution from doubly charged clusters of even n can be estimated as the interpolated doubly charged neighboring peaks of odd cluster size n. In figure 5.1a it can be seen that there are no doubly charged clusters at half integer numbers below $n/z = 6$. Therefore, we assume that the signals up to $n = 6$ result only from singly charged clusters. For integer values

Tab. 5.3: Experimental (Exp) and theoretical (CSM) saturation intensities are presented for niobium at 800 nm. Ionization potentials are added for reference purposes.

N	IP	(I_{sat} 10^{13} W/cm^2)	
	(eV)	EXP	CSM
1	6.76	5.6	0.9
2	6.20	5.1	0.7
3	5.81	2.8	0.5
4	5.64	2.8	0.5
5	5.45	2.8	0.4
6	5.38	2.0	0.4
7	5.35	2.0	0.4
8	5.53	2.2	0.5

of $n/z > 12$ the intensity is almost equal to the interpolated intensity of the neighboring doubly charged clusters of odd size n. Therefore, it can be assumed that the signals at all values $n/z > 12$ are due to doubly charged clusters only. In the region of $n/z = 7 - 12$ we have to deduct the estimated contribution of the doubly charged to the singly charged signals. This information is used to obtain saturation intensities for the first ionization step of Ni_1 to Ni_{12} and the second ionization step for both odd cluster sizes Ni_{13} to Ni_{37} and even cluster sizes Ni_{26} to Ni_{34}. The intensity is scanned to a maximum of $\sim 3\times10^{14}$ W/cm^2 and the ion yield is measured as shown in the semi-logarithmic plot in figure 5.1b for Ni_7. The estimated contribution of the signal due to double ionization of Ni_{14} is deducted from these results. We fitted a straight line (solid line in figure 5.1b to the high intensity results using the least square error method and obtained the saturation intensity at the intersection of this line and the intensity axis. At the same time we estimate the error in the saturation intensity by fitting two worst case lines (dashed) to the same results. The intensity axis was calibrated using our reference standard xenon. The saturation intensities for all measured nickel clusters ($z = 1$ and $z = 2$) are presented in table 5.1 and table 5.2 ,and figure 5.1c and 5.1d.

Niobium The second metal that was investigated is niobium with an atomic electronic ground state of $[Kr]4d^45s^1$. Niobium occurs naturally as a single isotope (^{89}Nb). The mass spectrum recorded with a bin width of 160 ns, is shown in figure 5.2a. Although the intensity at which all mass spectra are taken,

Fig. 5.2: In panel (a) the mass spectrum for Niobium is shown, where an almost complete absence of doubly charged clusters can be observed. An example intensity scan is shown in panel (b) for Nb_7. The experimental I_{sat} for the first ionization step (solid squares) for the niobium clusters are shown in panel (c); within the intensity range of this study, I_{sat} for z=2 can not be obtained (see panel d). Three models are included: (i) CSM, where the laser induced polarizability is neglected (dashed line), (ii) CSM where the dynamic multi-electron polarizability is included (solid line) and (iii) ZRP, a limiting MAE theory (dotted line). See figure 5.1 for details

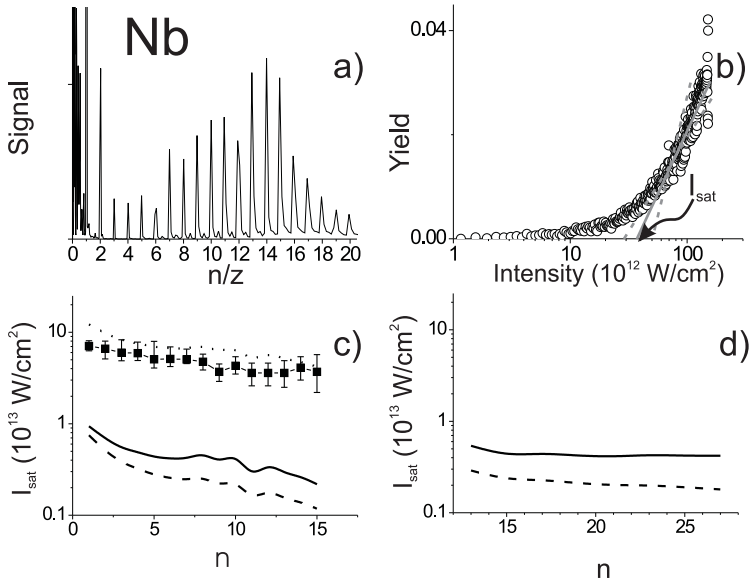

Fig. 5.3: The results for niobium at 800 nm are presented: (a) mass spectrum, (b) intensity scan for Nb_7 as an example and (c) saturation intensities. See the caption of figure 5.1 and text for details.

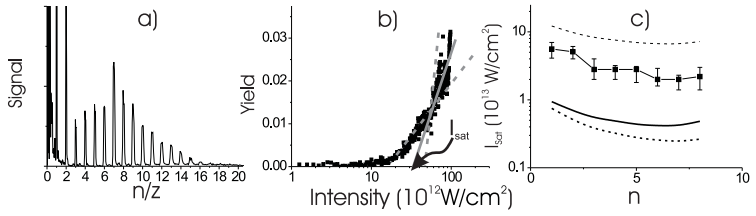

is the same ($\sim 10^{14}$ W/cm^2), and given the fact that the ionization potentials of niobium clusters are lower than the clusters of nickel, it is surprising to see an

almost complete absence of doubly charged clusters. Saturation intensities have been measured for Nb_1 to Nb_{15}. As an example, an intensity scan for Nb_7 is presented in figure 5.2b. The experimental values for the saturation intensities are presented in figure 5.2c and table 5.1 and are significantly higher than those of nickel. Due to this different behavior, more results are presented at a laser wavelength of 800 nm, where the maximum intensity that could be reached was 10^{15} W/cm^2. Even at this shorter wavelength no significant production of doubly charged niobium clusters is present. To rule out the unlikely process of dissociation, the mass spectrum has been compared to the mass spectrum obtained with the soft one photon ionization process with radiation from an ArF laser (not shown). No direct evidence of significant dissociation is observed (there is no evidence of much larger clusters in the ArF spectrum). The signals from the atom and dimer are not observed in the ArF spectrum as the photon energy is not sufficient to ionize these species. Furthermore the ArF spectrum is not sensitive to variations as a function of cluster size in IP, explaining the slight differences in intensities between the two mass spectra. The mass spectrum at 800 nm, as well as an intensity scan for Nb_7 are presented in figures 5.3a and 5.3b. Saturation intensities for Nb_1 to Nb_8 at 800 nm are presented in figures 5.3c and table 5.3.

Vanadium and Tantalum The two neighboring metals of niobium in the fifth column are tested to investigate if the behavior of niobium is typical for early transition metal clusters. The first row element is vanadium with an electronic ground state of the atom [Ar] $3d^3 4s^2$, giving five valence electrons. The mass spectrum of vanadium is shown in figure 5.4a with a bin width of 160 ns. Laser energies for ablation up to ~ 8 mJ were required for significant cluster production. The main ($> 99\%$) naturally occurring isotope of vanadium is ^{51}V. The cluster distribution peaks at $n \sim 20$ and the transmission is optimized for $n/z = 7$. Using the same method as described above, we obtained saturation intensities for the first ionization step of V_1 to V_{12} and the second ionization step of odd cluster size V_{15} to V_{21}. As an example the intensity scan for V_7 is shown in figure 5.4b with the contribution from V_{14}^{2+} subtracted. All measured saturation intensities of vanadium are presented in figures 5.4c and 5.4d, and table 5.1 and 5.2 .

The final metal of the fifth column is tantalum with an atomic electronic ground state [Xe] $4f^{14}5d^3 6s^2$, with again five valence electrons. The mass spectrum of tantalum is shown in figure 5.5a with a bin width of 160 ns and laser energies for ablation of $\sim$ 10 mJ. Tantalum occurs naturally with one main

Fig. 5.4: For Vanadium, the mass spectrum (a), an example intensity scan for V_7 (b) and I_{sat} for $z = 1$ (c) and $z = 2$ (d) are shown (see figure 5.1 for details). Three models are included in panel (c) and (d): (i) CSM, where the laser induced polarizability is neglected (dashed line), (ii) CSM where the dynamic multi-electron polarizability is included (solid line) and (iii) ZRP, a limiting MAE theory (dotted line).

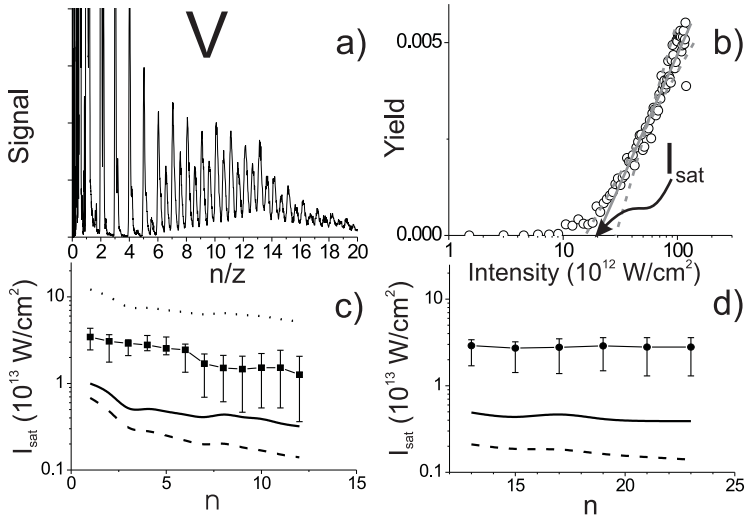

($> 99\%$) isotope ^{108}Ta . The cluster distribution peaks at $n \sim 15$ and the transmission is optimized for $n/z = 6$. The saturation intensities are measured for the first ionization step for Ta_1 to Ta_{12} and for the second ionization step for the odd cluster sizes Ta_{11} to Ta_{15}. An example of an intensity scan for Ta_7 is shown in figure 5.5b with the contribution from Ta_{14}^{2+} subtracted. All measured saturation intensities of tantalum are presented in figures 5.5c and 5.5d, and table 5.1 5.2.

5.4 Discussion

The transition from quantum mechanical behavior of small systems to a classical description of strong-field ionization of larger systems is investigated. The larger systems can be modeled as conducting spheres, whereas for the small systems a full multi-body quantum mechanical calculation is necessary. As such a calculation is presently not feasible, the results of the small systems are compared to a limiting perfect screening model.

Fig. 5.5: For Tantalum, the mass spectrum (a), an example intensity scan for Ta_7 (b) and I_{sat} for $z = 1$ (c) and $z = 2$ (d) are shown (see figure 5.1 for details). Three models are included in panel (c) and (d): (i) CSM, where the laser induced polarizability is neglected (dashed line), (ii) CSM where the dynamic multi-electron polarizability is included (solid line) and (iii) ZRP, a limiting MAE theory (dotted line).

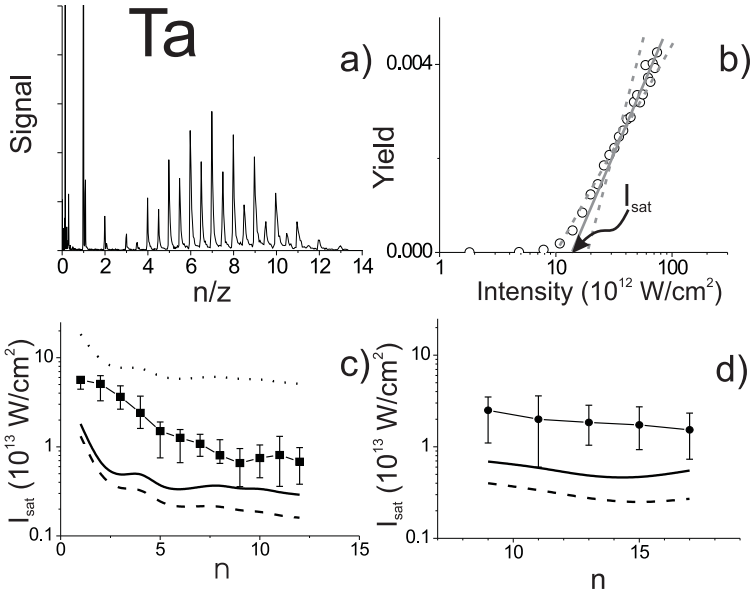

It is anticipated that the strong-field ionization of larger metal clusters can be described classically as is the case for the strong-field ionization of C_{60} [20]. To incorporate both the finite size and the multi-electron nature of clusters (or molecules), the systems of this study are modeled as conducting spheres (CS) of radius a, using classical electrodynamics (see figure 5.6). The potential (Φ_{CS}) is obtained by integrating the force equation of removing an electron to infinity from a charged sphere in the presence of an external electric field.

$$\phi_{CS}(r) = -Er + \frac{a^3}{r^2}E - \frac{q}{4\pi\epsilon}\Big(\frac{a}{2(r^2-a^2}} - \frac{z-a/2r}{r}\Big) \tag{5.1}$$

The two terms in brackets describe the contributions to the potential by the image charge and ionic charge z. The $\alpha E/r^2$ term is due to the instantaneous polarization in the sphere by the laser field, where classically $\alpha = a^3$. The saturation intensities are obtained numerically by computing where the barrier is suppressed by the (experimentally obtained) ionization potential. The radius

Fig. 5.6: The cluster is modeled as a classical conducting sphere of radius a. The MAE effect is taking into account as the polarization of the sphere by the external laser field E. The ejected electron with charge q at a distance r away from the center, induces an image charge of $-aq/r$.

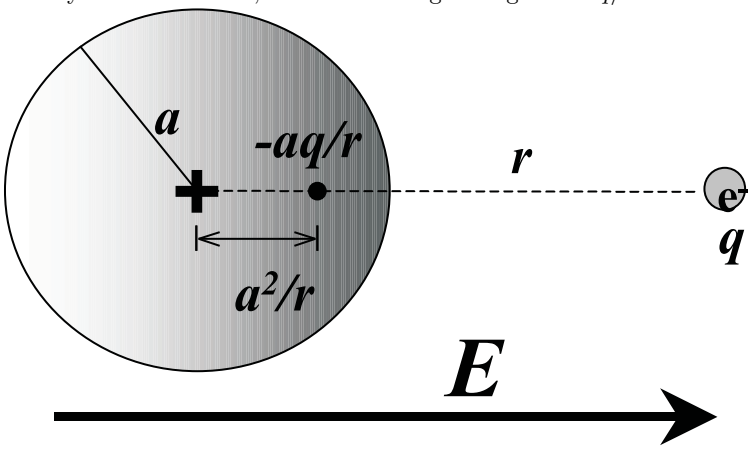

a of a given cluster size N is given by

$$a = N^{1/3} \cdot r_a, \tag{5.2}$$

where r_a is the atomic radius. Calculating the radius as the cubic root of the experimental polarizability (when available) yields similar results. Due to the polarization term in the conducting sphere model (CSM), it is an effective multi active electron (MAE) theory. The multi electron nature of the ionization mechanism is modeled by the polarizability of the sphere; the tunneling electron is still the only active electron. For comparison, a pure single active electron (SAE) theory is obtained by neglecting the polarizability term. This corresponds to considering the interaction of the laser field with one electron only, without taking into account any multi-electron response. In figure 5.1-5.5 the results are added of the CSM without the polarizability term (dashed line) and the CSM with the polarizability included (solid line). Known isomers with different ionization potentials exist for Nb_9, Nb_{12} and Ta_{12}. The highest IP is used in this study. As anticipated, by omitting the dipole term the theoretical saturation intensities of all clusters are substantially lower than the experimental values. We ascribe this to a multi-electron dynamic screening effect that suppresses ionization. By including the multi-electron dynamic screening as the polarizability term in CSM, agreement for the saturation intensities of the

first ionization step between the experiment and theory is approached for nickel clusters with $n > 10$. This convergence is similar to the convergence of the polarizabilities and ionization potentials of nickel clusters to classical models. For the ionization potential, theoretical values start to approach experimental values for $n > 10$ and are in full agreement for $n > 20$ [96]. Polarizabilities are available for $n > 11$ and are generally very close to theoretical predictions [98]. It is evident that the convergence only arises by including the dipole term. Unfortunately, no experimental values for the ionization potential for $z = 2$ (IP_2) are available and therefore the ionization potentials have been estimated using the first IP (IP_1) and the theoretical value using the molecular capacitance approach [106]

$$IP_2 = IP_1 + \frac{z-1}{R} \tag{5.3}$$

All measured saturation intensities for the second ionization step of the nickel clusters agree fairly well with CSM (see figure 5.1d), even though the ionization potentials are only an estimate. Once more, agreement between theory and experiment only obtains with the inclusion of multi electron effects (polarization). Although the convergence in the case of vanadium and tantalum is not as fast as in the case of nickel, reasonable agreement is obtained for $n > 10$ between the theoretical (CSM) and the experimental saturation intensity for the first ionization step. Unfortunately, no data are available on the polarizabilities of these clusters and therefore it is unknown where convergence to the polarizabilities calculated with classical models takes place. The larger discrepancy for the second ionization step might be ascribed to a wrong estimate of the second ionization potential. For comparison of the experimental and theoretical values, the theoretical (CSM) predictions for the saturation intensities are added to table 5.1 and 5.2.

Classical theories do not account for parameters like ionization potentials and polarizabilities for small metal clusters ($n < 10$). A classical description of the strong-field ionization of small metal clusters is therefore inapplicable. For hydrogen like (SAE) systems, a well-known example of a *quantum mechanical* SAE theory to calculate ionization rates is ADK theory [7]. It is only valid in the tunneling regime and as long as $W \ll 1$ ($I \ll I_{\mathrm{sat}}$). In the case of high ionization potentials, typical for noble gas atoms, the transition from $W \ll 1$ to $W \gg 1$ takes place very quickly and therefore ADK theory predicts correctly the saturation intensity for noble gas atoms. For systems with a high ionization potential, ADK and a classical theory, Barrier Suppression Ionization (BSI)

predict very similar saturation intensities that agree well with the experimental values for rare gas atoms. However, in the case of low ionization potentials (~ 5 eV), typical for metal clusters, the transition from $W \ll 1$ to $W \gg 1$ is very slow and a discrepancy between ADK and BSI arises. Although ADK theory predicts a higher saturation intensity than BSI for metal atoms in this study, that are closer to the experimental value, the reason for better agreement is the failure to apply ADK theory at high ionization rates and low ionization potentials. Even so, the experimental saturation intensities are a factor of 4-6 higher than predicted by ADK theory. Since the saturation intensity is a nonlinear measure, the absolute ionization rates can be off by a factor of $10^4 - 10^6$, indicating the dramatic suppression of ionization in multi electron atoms relative to SAE theories like ADK. In order to account fully for the experimental results, a multi-body numerical method has to be employed that is currently not available. As a limiting case we have argued previously that the potential of a system with perfect screening mimics that of a zero range potential (ZRP) [95]. In this study, the ZRP approach is applied to both the atom and the (larger) clusters. This approach indicates what the saturation intensity would be of a perfectly screened atom with an ionization potential of the corresponding cluster. Therefore, this approach is a limiting case for the effect of polarizability, but completely neglects the effect of size. The results of the ZRP approach are added to figures 5.1, 5.2, 5.4 and 5.5 as well (dotted line).

Classical models cannot account for the measured polarizabilities of small metal clusters. Since the polarizability is a key parameter in the description of strong-field ionization, classical models are likely to fail to describe strong-field ionization processes in such systems. It can be seen in figure 5.1c, 5.2c, 5.4c and 5.5c that for the small clusters the experimental saturation intensities lie above the classical CSM, but below the limiting quantum mechanical ZRP approach that ignores any size dependence.

Niobium shows a more extreme MAE behavior than the other metals that are investigated. The first indication of its anomalous behavior was obtained from the mass spectrum where an almost complete absence of double ionization was observed. Two more remaining anomalous results can be seen by comparing niobium to the other metals. First, the saturation intensities of the small clusters are significantly larger for niobium, whereas their ionization potentials are among the lowest of the metals tested. Secondly, within the investigated regime no convergence to CSM is obtained. Because of the anomalous results for nio-

bium, additional results are presented at 800 nm. In the 800 nm results a drop of the saturation intensities is observed in going from Nb_2 to Nb_3 (figure 5.3c). This trend is not observed in the 1.5 μm results (figure 5.2c), indicating that at 800 nm the ionization process might be non-adiabatic. The anomalous behavior of niobium is currently under further investigation in our laboratory, but several indications of unusual properties, including polarizabilities, of niobium clusters have been documented in the literature [92, 93].

5.5 Conclusion and future directions

The transition from quantum behavior of the smallest systems to a classical description of strong-field ionization of large systems is discussed. Furthermore the failure of SAE theories when applied to MAE systems is shown. The first system that has been discussed in the literature where a classical approach to describe the strong-field ionization has shown quantitative agreement with experiment was C_{60}. Here, additional results are presented where a convergence to this classical limit is shown. Hereto a prototype system is used: metal clusters. Small clusters of transition metals are ideal systems because of: (i) the tunability of the number of atoms per cluster; (ii) the many equivalent electrons to suppress ionization by polarization; (iii) the large mass per atom to avoid nuclear motion during the laser pulse; (iv) the high dissociation energy to avoid fragmentation; (v) the near spherical symmetry that allows for simple classical models to apply and to avoid alignment effects; and (vi) the availability of experimental and theoretical data like electronic structure, geometry, ionization potentials and polarizabilities. Four different metals from two different columns of the periodic table are tested: vanadium, niobium, tantalum and nickel. The shortcomings of single active electron theories are shown for all systems and agreement with experimental results is obtained for the larger clusters of vanadium, tantalum and nickel by employing a conducting sphere model that includes the multi-electron effect through dynamic polarization. Although the correction arising from the inclusion of the dynamic polarization is in the right direction for niobium, the predicted amounts of the boost in the barrier is not sufficient to explain our experimental results. In the case of small systems, quantum mechanical multi-body numerical simulations that are currently not available have to be employed. The physics from the classical model is compared to a limiting case: the zero range potential. This approach includes perfect screening as the MAE effect, but ignores any effects due to size. As

anticipated, all measured ionization rates (including those from the small clusters) are higher than predicted by the limiting model. Quantitative agreement for the small systems might be obtained if the true potential of these systems in a strong laser field, in combination with a classical or quantum mechanical treatment of the escaping electron, can be calculated.

In future experiments the source will be further developed to produce larger clusters to study the convergence to classical models. Especially in the case of niobium it will be interesting to find at which cluster size the experimental results will start to converge. Also, more metals will be investigated to produce a systematic data set of the strong-field ionization dynamics of transition metal clusters and to find out if the behavior of niobium is truly unique.

BIBLIOGRAPHY

[1] D. Strickland and G. Mourou. *Opt. Commun.*, 56:219, 1985.

[2] S. Backus, C.G. Durfee III, M.M. Murnane, and H.C. Kapteyn. *Rev. Sci. Intrum.*, 69(1207), 1998.

[3] A.M. Perelomov, V.S. Popov, and M.V. Terent'ev. *Sov. Phys. JETP*, 23:924, 1966.

[4] V. Keldysh. *Sov. Phys. JETP*, 20:1307, 1965.

[5] F. H. M. Faisal. *J. Phys. B*, 6:L89, 1973.

[6] H. R. Reiss. *Phys. Rev. A*, 22:1786, 1980.

[7] M. V. Ammosov, N. B. Delone, and V. P. Krainov. *Sov. Phys. JETP*, 64(6):1191, 1986.

[8] B. Walker, B. Sheehy, L. F. DiMauro, P. Agostini, K. J. Schafer, and K. C. Kulander. *Phys. Rev. Lett.*, 73:1227, 1994.

[9] S. Augst, D. Strickland, D. D. Meyerhofer, S. L. Chin, and J. H. Eberly. *Phys. Rev. Lett.*, 63:2212, 1989.

[10] P. Lambropoulos, P. Maragakis, and Jian Zhang. *Phys. Rep.*, 305:203, 1998.

[11] S. Augst, D. D. Meyerhofer, D. Strickland, S. L. Chin, and J. H. Eberly. *J. Opt. Soc. Am. B*, 8:858, 1991.

[12] P. B. Corkum. *Phys. Rev. Lett.*, 71:1994, 1993.

[13] H. Niikura, F. Legare, R. Hasbani, A. D. Bandrauk, M. Yu. Ivanov, D. M. Villeneuve, and Corkum P.B. *Nature*, 417:917, 2002.

[14] A. L'Huillier and P. Balcou. *Phys. Rev. Lett.*, 70:774, 1993.

[15] M. Drescher, M. Hentschel, R. Kienberger, G. Tempea, C. Spielman, G.A. Reider, P.B. Corkum, and F. Krausz. *Science*, 291:1923, 2001.

[16] P. Agostini, F. Fabre, G. Mainfray, G. Petite, and N. K. Rahman. *Phys. Rev. Lett.*, 42:1127, 1979.

[17] D. T. Strickland, Y. Beaudoin, P. Dietrich, and P. B. Corkum. *Phys. Rev. Lett.*, 68:2755, 1992.

[18] R.J. Levis, G.M. Menkir, and H. Rabitz. *Science*, 92:709, 2001.

[19] A. Assion, T. Baumert, M. Bergt, T. Brixner, B. Kiefer, V. Seyfried, M. Strehle, and G. Gerber. *Science*, 282:919, 1998.

[20] V. R. Bhardwaj, P. B. Corkum, and D. M. Rayner. *Phys. Rev. Lett.*, 91:172302, 2003.

[21] J.S. Horwitz, H.U. Krebs, and K. Murakami, editors. *Laser Ablation, Proceedings of the 5th International Conference.* Springer, New York, 1999.

[22] R.S. Taylor, C. Hnatovsky, E. Simova, D.M. Rayner, M. Mehendale, V.R. Bhardwaj, and P.B. Corkum. *Opt. Express*, 11:775, 2003.

[23] G.L. Yudin and M.Yu. Ivanov. *Phys. Rev. A 64*, 64:013409, 2001.

[24] S. M. Hankin, D. M. Villeneuve, P. B. Corkum, and D. M. Rayner. *Phys. Rev. A*, 64:013405, 2001.

[25] M. J. DeWitt and R. J. Levis. *J. Chem. Phys.*, 108:7739, 1998.

[26] M. Lezius, V. Blanchet, D. M. Rayner, D. M. Villeneuve, A. Stolow, and M. Yu. Ivanov. *Phys. Rev. Lett.*, 86(1):51, 2001.

[27] M. Lezius, V. Blanchet, M. Yu. Ivanov, and A. Stolow. *J. Chem. Phys.*, 117:1575, 2002.

[28] T. Seideman, M. Yu. Ivanov, and P. B. Corkum. *Phys. Rev. Lett.*, 75:2819, 1995.

[29] T. Ditmire, T. Donnelly, A. M. Rubenchik, R. W. Falcone, and M. D. Perry. *Phys. Rev. A*, 53:3379, 1996.

[30] S. M. Hankin, D. M. Villeneuve, P. B. Corkum, and D. M. Rayner. *Phys. Rev. Lett.*, 84(22):5082, 2000.

[31] M. Lenzner, J. Krüger, S. Sartania, Z. Cheng, Ch. Spielmann, G. Mourou, W. Kautek, and F. Krausz. *Phys. Rev. Lett.*, 80:4076, 1998.

[32] J. Muth-Bohm, A. Becker, and F. H. M. Faisal. *Phys. Rev. Lett.*, 85:2280, 2000.

[33] J. Zanghellini, M. Kitzler, C. Fabian, T. Brabec, and A. Scrinzi. *Laser Physics*, 13(8):1064, 2003.

[34] C. Fabian, M. Kitzler, N. Milosevic, and T. Brabec. *J. Mod. Opt.*, 50:589, 2003.

[35] V. R. Bhardwaj, D. M. Rayner, D. M. Villeneuve, and P. B. Corkum. *Phys. Rev. Lett.*, 87:253003, 2001.

[36] D. Du, X. Liu, and G. Mourou. *Appl. Phys. B*, 63:617, 1996.

[37] R. R. Jones. *Phys. Rev. Lett.*, 75:1491, 1995.

[38] R. R. Jones. *Phys. Rev. Lett.*, 74:1091, 1995.

[39] A. Talebpour, C.Y. Chin, and S. L. Chin. *J. Phys. B*, 29:5725, 1996.

[40] M. A. Walker, P. Hansch, and L. D. van Woerkom. *Phys. Rev. A*, 57:R701, 1998.

[41] P. Hansch and L. D. V. Woerkom. *Opt. Lett.*, 21:1286, 1996.

[42] C.J.G.J. Uiterwaal, B Witzel, Schröder, and K.-L. Kompa. *Phys. Rev. A*, 58:1592, 1998.

[43] M.B. Knickelbein. *Phil. Mag. B*, 79(1379), 1999.

[44] C.C. Hayden and A. Stolow. *in Advanced Series in Physical Chemistry*, volume Vol.10: Photoionization AND Photodetachment. World Scientific, Singapore, 2000.

[45] D.M. Neumark. *Annu. Rev. Phys. Chem.*, 52(255), 2001.

[46] T. Seideman. *Annu. Rev. Phys. Chem.*, 53(41), 2002.

[47] A. Stolow. *Annu. Rev. Phys. Chem.*, 54(89), 2003.

[48] A. Stolow. *Int. Rev. Phys. Chem.*, 22(377), 2003.

[49] I. Fischer, M.J.J. Vrakking, D.M. Villeneuve, and A. Stolow. *Chem. Phys.*, 207(331), 1996.

[50] A. Zavriyev, I. Fischer, D.M. Villeneuve, and A. Stolow. *Chem. Phys. Lett.*, 234(281), 1995.

[51] T. Baer. *Int. J. Mass. Spectrom.*, 200(443), 2000.

[52] V. Stert, W. Radloff, C. P. Schulz, and I. V. Hertel. *Eur. Phys. J. D*, 5:97, 1999.

[53] R.E. Continetti and C.C. Hayden. *in Advanced Series in Physical Chemistry: Modern Trends in Chemical Reaction Dynamics.* in press.

[54] R.E. Continetti. *Annu. Rev. Phys. Chem.*, 52(165), 2001.

[55] M. Takahashi, J.P. Cave, and J.H.D. Eland. *Rev. Sci. Instrum.*, 71(1337), 2000.

[56] P. Downie and I. Powis. *Phys. Rev. Lett.*, 82(2864), 1999.

[57] S. Fredrigo, T.L. Haslett, and M. Moskovits. *J. Am. Chem. Soc.*, 118(5083), 1996.

[58] D.B. Geohegan. *Laser Ablation of Electronic Materials: Mechanisms AND Applications.* North Holland, Amsterdam, 1992.

[59] R. Kelly and A. Miotello. *Appl. Phys. B: Photophys. Laser Chem.*, 57(145), 1993.

[60] R. Kelly, A. Miotello, B. Braren, A. Gupta, and K. Casey. *Nucl. Instrum. Methods Phys. Res. B*, 65(187), 1992.

[61] D. Sibold and H.M. Urbassek. *Phys. Fluids*, 16(1149), 1992.

[62] J.W. Elam and D.H. Levy. *J. Phys. Chem. B*, 102(8113), 1998.

[63] R.J. Levis. *Ann., Rev. Phys. Chem.*, 45(483), 1994.

[64] R.N. Zare and R. Zenobi. *Advances in Multi-Photon Processes AND Spectroscopy*, volume Vol. 7. World Scientific, River Edge, NJ,, 1991.

[65] L.V. Zhigilei, E. Leveugle, B.J. Garisson, Y.G. Yingling, and M.I. Zeifman. *Chem. Rev.*, 103(321), 2003.

[66] J.E. Bernard and A.J. Alcock. *Opt. Lett.*, 19(1861), 1994.

[67] R. Campargue. *J. Phys. Chem.*, 88(4466), 1984.

[68] J.B. Fenn and J. Deckers. *Rarefield gas dynamics*, volume Vol. 1. Academic Press, New York, 3rd symposium edition, 1963.

[69] J.B. Anderson. *Molecular beams AND low density gas dynamics.* M. Dekker, New York, 1974.

[70] M.E. Geusic, M.D. Morse, S.C. O'Brien, and R.E. Smalley. *Rev. Sci. Instrum.*, 56(2123), 1985.

[71] M.D. Morse, M.E. Geusic, J.R. Heath, and R.E. Smalley. *J. Chem. Phys.*, 83(2293), 1985.

[72] S. Lochbrunner, J. J. Larsen, J. P. Schaffer, M. Schmitt, T. Schultz, J. G. Underwood, and A. Stolow. *J. Electron Spectrosc. Relat. Phenom.*, 112:183, 2000.

[73] C. Spielmann, H. Burnett, R. Sartania, R. Koppitsch, M. Chnurrer, C. Kan, M. Lenzner, P. Wobrauschek, and F. Krausz. *Science*, 278(661), 1997.

[74] M. Smits, C. A. de Lange, A. Stolow, and D. M. Rayner. *Phys. Rev. Lett.*, 93, 2004.

[75] T.M. Miller. *Handbook of Chemistry and Physics.* CRC Press, Boca Raton, 82nd edition edition, 2001.

[76] M.A. Posthumus, P.G. Kistemaker, H.L.C. Meuzelaar, and M.C. Ten Noever de Brauw. *Anal. Chem.*, 50(985), 1978.

[77] G. Meijer, M.S. De Vries, H.E. Hunziker, and H.R. Wendt. *Appl. Phys. B*, 51(395), 1990.

[78] A.H. Zewail. *Femtochemistry: Ultrafast Dynamics of the Chemical Bond.* World Scientific, Singapore, 1994.

[79] A.H. Zewail. *J. Phys. Chem. A*, Feature Article 104(5660), 2000.

[80] J. Jortner. *Faraday Discuss.*, 108(1), 1997.

[81] V. Blanchet, M.Z. Zgierski, T. Seideman, and A. Stolow. *Nature*, 401(52), 1999.

[82] V. Blanchet, M.Z. Zgierski, and A. Stolow. *J. Chem. Phys.*, 114(1194), 2001.

[83] M. Schmitt, S. Lochbrunner, J.P. Shaffer, J.J. Larsen, M.Z. Zgierski, and A. Stolow. *J. Chem. Phys.*, 114(1206), 2001.

[84] F. Piuzzi, I. Dimicoli, M. Mons, B. Tardivel, and Q. Zhao. *Chem. Phys. Lett.*, 320(282), 2000.

[85] R. Weinkauf, P. Aicher, G. Wesley, J. Grotemeyer, and E.W. Schlag. *J. Phys. Chem.*, 98(8381), 1994.

[86] G.D. Gillen and L.D. Van Woerkom. *Phys. Rev. A*, 68(3):33401, 2003.

[87] M. Sukharev, E. Charron, and A. Suzor-Weiner. *Phys. Rev. A*, 66(5):53407, 2002.

[88] M. Smits, C. A. de Lange, S. Ullrich, T. Schultz, M. Schmitt, J. G. Underwood, J. P. Shaffer, D. M. Rayner, and A. Stolow. *Rev. Sci. Instrum.*, 74(11):4812, 2003.

[89] S.G. Lias and J.F. Liebman. *NIST Chemistry WebBook, NIST Standard Reference Database Number 69 (http://webbook.nist.gov).* National Institute of Standards and Technology, Gaithersburg, 2003.

[90] M. Kitzler, J. Zanghellini, M. Smits, A. Scrinzi, and T. Brabec. *Phys. Rev. A.*, 70:041401(R), 2004.

[91] A. Scrinzi, M. Geissler, and T. Brabec. *Phys. Rev. Lett.*, 83(706), 1999.

[92] R. Moro, X. Xu, S. Yin, and W.A. de Heer. *Science*, 300:1265, 2003.

[93] M. B. Knickelbein. *J. Chem. Phys.*, 118:6230, 2003.

[94] M. Smits, C. A. de Lange, M. Kitzler, A. Stolow, and D. M. Rayner. *in preperation.*

[95] M. Smits, C. A. de Lange, A. Stolow, and D. M. Rayner. *Phys. Rev. Lett.*, 93, 2004.

[96] M. B. Knickelbein and S. Yang. *J. Chem. Phys.*, 93(8):5760, 1990.

[97] M. B. Knickelbein, S. Yang, and S. J. Riley. *J. Chem. Phys.*, 93(1):94, 1990.

[98] M. B. Knickelbein. *J. Chem. Phys.*, 115(13):5957, 2001.

[99] B. A. Collings, K. Athanassenas, D. M. Rayner, and P. A. Hackett. *Z. Phys. D.*, 26:36, 1992.

[100] W. J. C. Menezes and M. B. Knickelbein. *J. Chem. Phys.*, 98(3):1856, 1993.

[101] M.B. Knickelbein and W.J.C. Menezes. *Phys. Rev. Lett.*, 69(7):1046, 1992.

[102] A.M. James, P. Kowalczyk, R. Fournier, and B. Simard. *J. Chem. Phys.*, 99:8504, 1993.

[103] M.B. Knickelbein. *J. Chem. Phys.*, 99(4):2377, 1993.

[104] H. Gronbeck and A. Rosen. *Phys. Rev. B*, 54(3):1549, 1996.

[105] E. K. Parks, B. J. Winter, T. D. Klots, and S. J. Riley. *J. Chem. Phys.*, 94:1882, 1991.

[106] J. Jortner. *Z. Phys. D*, 24:247, 1992.

6. APPENDIX

In the following, two Letters based on part of the results of this thesis are presented in the format of the original publication in the scientific journal "Physical Review Letters". The first Letter deals with the Multi Active Electron (MAE) effects in the Strong Field Ionization (SFI) of transition metal atoms, whereas the second with MAE effects in the SFI of the clusters of these metals.

Absolute ionization rates of multi-electron transition metal atoms in strong infrared laser fields

Marc Smits and C.A. de Lange
Department of Physics and Astronomy, Vrije Universiteit Amsterdam, Netherlands

Albert Stolow* and D. M. Rayner†
Steacie Institute for Molecular Sciences, National Research Council Canada, 100 Sussex Dr., Ottawa, ON K1A 0R6 Canada
(Dated: October 8, 2004)

We report on non-resonant strong field ionization of the multi-electron transition metal atoms V, Nb, Ta, Ni and Pd. Operating in the adiabatic regime ($\lambda = 1.5\mu$m) and using a restricted collection volume / constant axial intensity focusing geometry with calibrated absolute intensities, we quantitatively determined both (i) the first charge state saturation intensities and (ii) the absolute ionization rates for intensities ranging from threshold up to 3×10^{14} W/cm^2. We observed a dramatic suppression of ionization relative to Single Active Electron approximation expectations. We suggest that this derives from dynamic polarization/screening effects within the multi-electron atom, stressing a need for many-body theories of strong field ionization.

PACS numbers: 32.80.Rm, 42.50.Hz

Strong field ionization dynamics is central to many extreme nonlinear optical processes such as high harmonic, X-ray and attosecond pulse generation. Much of our understanding of these dynamics derives from adiabatic theories based upon strong field (SF) tunnel ionization and single active electron (SAE) approximations. These theories, of which Ammosov-Delone-Krainov (ADK) is a well known example [1], successfully describe the strong field ionization dynamics of the effectively SAE rare gas atoms [2]. To understand the strong field physics of matter more generally, true multi-electron systems and their many-body dynamics must be considered. The first correlated two-electron phenomenon, non-sequential double ionization in rare gases, can be treated within the SF-SAE picture by considering the recollision of the continuum SAE with the core [2, 3]. The strong field ionization of two-electron atoms (Mg and Ca) show perhaps the first hints of deviation from the SF-SAE picture [4, 5]. Much more complex multi-electron correlation phenomena, showing a complete failure of the SF-SAE picture, were observed in the strong field ionization of polyatomic molecules in both the adiabatic [6, 7] and non-adiabatic [8, 9] regimes. Diatomic molecules also show differences from SAE atoms that relate to the molecular nature of the physics [10–12]. A complete many-body theory treatment of multi-electron dynamics in a strong laser field, however, is in the very early stages of development [13, 14] and therefore there is a great need for detailed, direct comparison of theory with simpler systems: multi-electron atoms. In the following, we present a quantitative determination of absolute ionization rates as a function of intensity and saturation intensities for a series of multi-electron transition metal atoms.

In the adiabatic SF regime all electrons, not just the most weakly bound 'active' one, must respond to the applied field. If there are many polarizable electrons, we expect that these will all be pushed by the field up against the partially suppressed barrier and lead to enhanced repulsion for the 'active' electron, as was discussed for the case of molecules [8]. This type of dynamic polarization yields an effectively higher tunnelling barrier and therefore a suppression of ionization. SAE models such as ADK appear to provide a good description of the ionization dynamics of the rare gases and, in this context, these show no suppression of ionization. To provide quantitative data on the adiabatic SF ionization dynamics of multi-electron atoms, we have undertaken a systematic study of two series of transition metal atoms: V, Nb and Ta (each having five outer valence electrons), and Ni and Pd (each having ten outer valence electrons). We compare our results with both ADK theory and

a simple model which we argue mimics the limiting behaviour of infinitely polarizable systems: the delta or zero-range potential (ZRP).

A stable kHz-rate laser ablation source was used to produce the transition metal atomic beam, using helium as the carrier gas [15]. A rotating, translating rod of pure metal (V, Nb, Ta, Ni, Pd) was used as the target. An amplified femtosecond Ti:Sa laser system pumped an optical parametric amplifier (OPA) to produce < 90 fs pulses at 1.5 μm with > 150 μJ of energy [16]. The focused ($f/15$) infrared laser pulses intersected the atomic beam in the extraction region of a linear time-of-flight mass spectrometer (TOFMS). The mass spectrum and laser intensity were recorded for each laser shot. We measured the intensity dependence of the atomic mass peak up to a maximum of 3×10^{14} W/cm^2.

We implemented the saturation intensity method that employs a constant axial intensity ion collection geometry, as discussed in detail elsewhere [6, 7]. Briefly, a narrow slit (<500 μm) placed perpendicular to the laser propagation direction permitted collection only of ions formed in a region of constant axial intensity. With this geometry, a linear dependence of the ionization yield on the logarithm of the intensity holds at high intensity. The saturation intensity, I_{sat}, is defined as the threshold intensity for this (extrapolated) linear behaviour and is a general measure of the "ease" of ionization. As I_{sat} is an atomic property which does not depend on experimental factors such as detection efficiency or focusing geometry, comparison with theory is unambiguous. Absolute laser intensities were determined by in situ calibration against the known saturation intensity of xenon, as described in detail elsewhere [7].

In Fig. 1 we show an example of a typical intensity scan, here for the Nb atom. The measured ion yield is plotted as a function of the logarithm of the absolute peak intensity. Similar data were recorded for V, Ta, Ni and Pd atoms. Saturation intensities are obtained by extrapolation of the high intensity linear behaviour, as shown in the figure. The I_{sat} determined from each fit is given in Table I, along with the previously reported ionization potential [17] and static polarizability [18] of each atom.

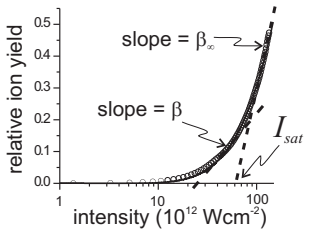

FIG. 1: A typical intensity scan, shown here for the Nb atom. The ion yield is plotted vs. the logarithm of the peak intensity. The saturation intensity I_{sat} is defined as the intensity axis intercept of a linear extrapolation of the high intensity behaviour. A multi-exponential fit to the data is shown as a solid line. The limiting slope β_∞, its intercept I_{sat} and the slope β at a lower intensity are shown. As discussed in the text, β was used to extract the absolute ionization rates. All other atoms (not shown) were treated in a similar manner.

TABLE I: Experimental saturation intensities and the corresponding values for both ADK and ZRP models are given for V, Nb, Ta and Ni, Pd. η, the relative measure of ZRP behaviour, ranges from zero for ideal ADK behaviour to 1 for ideal ZRP behaviour. For reference, the electronic configurations, ionization potentials [17] and static polarizabilities [18] are given.

Atom	Configuration	IP	α	I_{sat} (10^{13} W/cm^2)			η
		(eV)	Å^3	Exp	ADK	ZRP	
V	[Ar] $3d^34s^2$	6.75	12.4	3.2	1.2	12.2	0.18
Nb	[Kr] $4d^45s^1$	6.76	15.7	6.7	1.2	12.2	0.50
Ta	[Xe] $4f^{14}5d^36s^2$	7.89	13.1	5.4	2.1	18.4	0.20
Ni	[Ar] $3d^84s^2$	7.6	6.8	4.7	1.8	16.7	0.19
Pd	[Kr] $4d^{10}$	8.34	4.8	6.2	2.6	21.3	0.19
Xe	[Kr] $4d^{10}5s^25p^6$	12.13	4	9.5	9.5	57.6	0

The absolute ionization rates as a function of intensity were determined by transformation of the ion yield data in a manner detailed elsewhere [7]. Briefly, the method depends on measuring the slope of the ion yield curves as a function of intensity. To reduce differentiation noise, the raw ion yield data (as in Fig. 1) were smoothed with a ten point binning method. The limiting slope β_∞ of the high intensity linear behaviour was then evaluated. This experimentally determined slope contains the dependence on all experimental parameters ($\beta_\infty = \kappa c \pi R^2 l$): the apparatus sensitivity (κ), the concentration of atoms in the beam (c), the Gaussian beam waist (R), and the length of the constant axial inten-

sity region of the focus that is projected through the slits onto the ion detector (l). Finally, the slope β at all lower intensities was obtained by a three-point differential method: the slope at any given point was calculated from the rise and run over its two neighbouring points. The cycle-averaged intensity dependent ionization rate is $W(I_0, f(t))$ where I_0 is the Gaussian peak intensity and $f(t)$ is the pulse envelope function. The time integral of the ionization rate over the pulse envelope, as discussed in detail elsewhere [7], is given by the following transformation:

$$\int_{-\infty}^{\infty} W(I_0, f(t))dt = \ln \frac{\beta_\infty}{\beta_\infty - \beta}. \qquad (1)$$

For the case of a square top pulse of duration τ, the integral in Eq. 1 reduces to $W(I_0)\tau$ where $W(I_0)$ is the absolute ionization rate. In Fig. 2, both the square top absolute ionization rate and the integrals $\int_{-\infty}^{\infty} W(I_0, f(t))dt$, are plotted as a function of absolute intensity for the atoms V, Nb, Ta, Ni and Pd. The solid lines represent ionization rates derived from transformation (in the manner prescribed for the raw data) of the functional fit to the experimental data shown in Fig. 1 and similarly for all other atoms. The effective pulse duration τ for the square top pulse was obtained by fitting xenon intensity scan data to ADK theory.

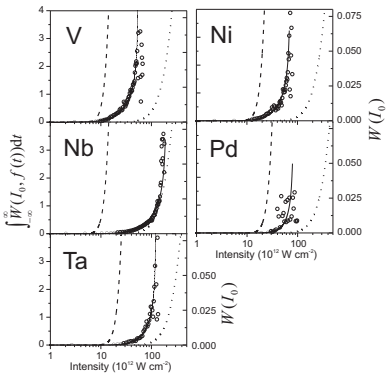

FIG. 2: Absolute ionization rates (open circles), determined from direct transformation [Eq. 1] of the data from Fig. 1 and similar data for the other atoms, are shown for each of V, Nb, Ta, Ni and Pd. The envelope-integrated ionization rates, left ordinate, are plotted as a function of peak intensity. Assuming a square-top pulse, the resultant absolute ionization rates in fs^{-1} are given by the right ordinate. The solid lines are the same transformation applied to the numerical fit to the data of Fig. 1 and likewise for the other atoms. The dashed lines are the ionization rates obtained via ADK theory and show a dramatic overestimation of the rates. The dotted lines show the limiting behaviour expected from a zero-range potential ZRP model, as described in the text.

In the following, the observed ionization rates of multi-electron atoms are compared with two limiting case models. The first model is ADK, a benchmark for single active electron atoms. Our measurements are carried out at intensities where the Keldysh parameter, γ, ≈ 0.5 or less, conditions under which ADK is still expected to maintain good accuracy for cycle averaged rates [19]. It can be seen from Table I that, in all cases, the experimental I_{sat} significantly exceeds the ADK value and from Fig. 2 that ADK drastically overestimates ionization rates: around the ADK I_{sat}, the ADK absolute ionization rate is off by a factor of $10^4 - 10^6$ (it is important to note that I_{sat} is a logarithmic measure). This demonstrates the dramatic nature of the suppression of ionization in these multi-electron atoms relative to SAE expectations. More general, but more difficult to apply and therefore less widely used treatments such as exact numerical SAE calculations [2] and the analytical SAE derivation of Perelomov-Popov-Terentev (PPT) [20] show that that ADK progressively underestimates ionization rates as γ increases above 0.5 so there is even greater disparity between our experimental results and the predictions of more sophisticated SAE approaches. We suggest that this suppression is due to the dynamic (but adiabatic) polarization of all electrons in the strong field, leading to displacement of electron density towards the barrier and, hence, increased repulsion for the 'active' electron which must pass through this region in order to escape. Equivalently, a test charge approaching the barrier from afar climbs the potential due to the laser field and feels, at close range, enhanced repulsion due to the polarization of electrons towards the barrier and, therefore, an increase of the barrier height at short range (thus leading to dramatically re-

duced tunnelling rates).

We now consider the other limiting case - that of very high multi-electron contribution to the polarizability. None of the SAE models, including ADK, consider any dynamics internal to the potential and therefore cannot include dynamic screening effects. As full many-body theories of strong field ionization dynamics are still under development [13, 14], it is useful to consider simplified models. Qualitatively, we expect an adiabatic multi-electron polarization to lead to field-induced enhancement of the tunnelling barrier for the active electron. As a model of the high polarizability limit, we used a simple function - the delta function or zero range potential (ZRP) - which we argue represents the limiting case for high multi-electron polarizability systems.

We expect that multi-electron polarization leads to displacement of electron density away from the core in the direction of the laser electric field - i.e. downfield towards the tunnelling barrier. This enhancement of electron density between the core and the exterior region should lead to enhanced screening of the core as viewed from the downfield exterior region. In the upfield region opposite the barrier, we expect, if anything, the core to be more exposed due to this displacement of electron density. As we are concerned with tunnelling rates through the field-modified barrier, we focus only on the downfield side. A simple way to mimic multi-electron screening is through the use of an effective Coulomb charge z. A reduced z implies core screening and leads to a change in the shape of the downfield potential relative to the $z = 1$ Coulomb potential, as illustrated in Fig. 3. The tunnelling barrier increases as z decreases. In the limit tending towards $z = 0$ (i.e. 'perfect' downfield screening), the potential tends towards the triangular barrier associated with a delta, or zero-range, potential function in the field. If we neglect changes in the pre-exponential factor, we can estimate the tunnelling rate through this limiting triangular barrier as that from a zero-range potential (ZRP). We propose that the ZRP behaves as the high multi-electron polarizability limit of dynamic screening of atoms in a strong laser field.

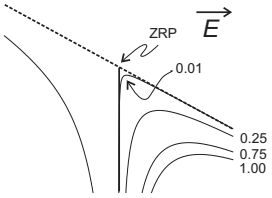

FIG. 3: Adiabatic multi-electron polarization in a strong laser field leads to displacement of electron density towards the barrier. This leads to enhanced screening of the core as viewed from the downfield region. We mimic the enhanced downfield screening through the use of an effective Coulomb charge z. For an unscreened core of unit charge, z=1, reduction in z (i.e. more core screening) mimics the field-induced modification of the tunnelling barrier, as can be seen for z=0.75, 0.25 and 0.01. In the limit, $z \to 0$, the potential tends towards a delta or zero-range potential(ZRP).

Therefore, we used the cycle-averaged Wentzel-Kramers-Brillouin (WKB) tunnelling rates out of ZRPs as the second limiting case - that of high multi-electron polarizability - for calculating ionization rates.

In Table I we present our experimental saturation intensities as well as the ADK and ZRP expectations. In Fig. 2, we show the absolute ionization rates calculated for each atom from both the ADK (dashed line) and ZRP (dotted line) models. In all cases, the experimental rates are bracketed by the two models, although the Nb rates approach more closely to the ZRP limit.

As a single parameter measure of the multi-electron contribution to the suppression of ionization via the dynamic polarizability, we propose the following:

$$\eta = \frac{I_{sat}(\mathrm{Exp}) - I_{sat}(\mathrm{ADK})}{I_{sat}(\mathrm{ZRP}) - I_{sat}(\mathrm{ADK})} \qquad (2)$$

The value η is a number between 0 and 1. A number close to 0 denotes good agreement with ADK theory and a single active electron picture of the ionization dynamics (hence, $\eta = 0$ for Xe). A value close to 1 denotes good agreement with the ZRP model which we suggest is indicative of strong multi-electron contributions to the dynamic polarization, leading to dramatic suppression of ionization rates. It is important

to note that η is defined in terms of the saturation intensities (as in Fig. 1) and not from the absolute ionization rates (as in Fig. 2). As can be seen from Table I, except for Nb, all these atoms show a value of η around 0.2, indicating some multi-electron contributions to the dynamic screening. Interestingly, these appear to be invariant with respect to the total number of valence electrons or the static polarizability. For Nb, by contrast, $\eta = 0.5$ represents a very strong dynamic screening effect. This anomalous behaviour is currently under further investigation in our laboratory, but several indications of the unusual polarizability of Nb and its clusters have been documented in the literature [21, 22].

In conclusion, the strong field ionization dynamics of the multi-electron atoms V, Nb, Ta, Ni and Pd have been investigated in the adiabatic (infrared) limit. We reported absolute ionization rates and saturation intensities that are independent of experimental parameters and, hence, are directly comparable with theory. We observed a strong suppression of ionization, as compared with single active electron theory expectations. We ascribed this effect to multi-electron dynamic screening, related to the multi-electron contribution to the polarizability of the system, analogous to what was discussed in the strong field ionization of C_{60} [23] and metal clusters [24]. The latter systems were described in terms of a classical conducting sphere model, successful in treating larger systems such as clusters of ten or more metal atoms, but which does not apply to small quantum systems: classical models fail to describe the polarizability of single atoms. We have bracketed the absolute ionization rates of the atoms investigated here between, on the one hand, a SAE model (ADK) and, on the other hand, a simple model which we propose behaves as the high dynamic screening limit - the zero range potential (ZRP). In strong fields, even material systems as simple as isolated atoms can exhibit a richness that transcends the simple physics of one electron systems. We hope that these results will encourage the further development of full many-body quantum mechanical theories of strong field ionization.

The authors especially wish to thank M.-Yu. Ivanov (NRC) for many helpful discussions. In addition we thank Profs. T. Brabec (Univ. of Ottawa) and E. Zaremba (Queen's Univ.) for valuable discussions.

* Electronic address: albert.stolow@nrc-cnrc.gc.ca;
† Electronic address: david.rayner@nrc-cnrc.gc.ca

[1] M. V. Ammosov et al., Sov. Phys. JETP **64**, 1191 (1986).
[2] B. Walker et al. Phys. Rev. Lett. **73**, 1227 (1994).
[3] P. B. Corkum, Phys. Rev. Lett. **71**, 1994 (1993).
[4] G. D. Gillen and L. D. Van Woerkom, Phys. Rev. A **68**, 33401 (2003).
[5] M. Sukharev et al., Phys. Rev. A **66**, 53407 (2002).
[6] S. M. Hankin et al., Phys. Rev. Lett. **84**, 5082 (2000).
[7] S. M. Hankin et al., Phys. Rev. A **64**, 013405 (2001).
[8] M. Lezius et al., Phys. Rev. Lett. **86**, 51 (2001).
[9] M. Lezius et al., J. Chem. Phys. **117**, 1575 (2002).
[10] M. J. DeWitt et al., Phys. Rev. Lett. **87**, 153001 (2001).
[11] X. M. Tong et al., Phys. Rev. A **66**, 033402 (2002).
[12] J. Muth-Bohm et al., Phys. Rev. Lett. **85**, 2280 (2000).
[13] J. Zanghellini et al., J. Phys. B **37**, 763 (2004).
[14] C. Fabian et al., J. Mod. Opt. **50(3-4)**, 589 (2003).
[15] M. Smits et al., Rev. Sci. Instrum. **74**, 4812 (2003).
[16] S. Lochbrunner et al., J. Electron Spectrosc. Relat. Phenom. **112**, 183 (2000).
[17] S. G. Lias and J. F. Liebman, in *NIST Chemistry WebBook, NIST Standard Reference Database Number 69 (http://webbook.nist.gov)*, edited by P. J. Linstrom and W. G. Mallard (NIST, Gaithersburg, 2003).
[18] T. M. Miller, in *Handbook of Chemistry and Physics*, edited by D. Lide (CRC Press, Boca Raton, 2003), 84th ed.
[19] G. Yudin and M. Ivanov, Phys. Rev. A 64 **64**, 013409 (2001).
[20] A. Perelomov et al., Sov. Phys. JETP **23**, 924 (1966).
[21] R. Moro et al., Science **300**, 1265 (2003).
[22] M. B. Knickelbein, J. Chem. Phys. **118**, 6230 (2003).
[23] V. R. Bhardwaj et al., Phys. Rev. Lett. **91**, 203004 (2003).
[24] M. Smits et al., submitted (2004).

APS/123-QED

Dynamic polarization in the strong field ionization of small metal clusters

Marc Smits[†], C.A. de Lange [†], Albert Stolow[*], D. M. Rayner [*]
[†] *Department of Physics and Astronomy, Vrije Universiteit Amsterdam, Netherlands and Steacie Institute for Molecular Sciences, National Research Council Canada, 100 Sussex Dr., Ottawa, ON K1A 0R6 Canada* [*]

(Dated: December 17, 2004)

We report on the strong field ionization of small transition metal clusters (nickel, Ni_n n= 1-36) within the quasi-static regime at an infrared wavelength of 1.5 μm and at intensities up to 2×10^{14} W/cm^2. By measuring ion yields in a constant axial intensity focusing geometry, we obtained saturation intensities for the individual Ni_n clusters. As compared to quasi-static, single active electron theory expectations, a dramatic suppression of ionization was observed. We ascribe this to a dynamic polarization in the laser field that leads to strong multi-electron screening of the "active" electron. To support this idea, we represented the metal clusters as classical conducting spheres and, via a barrier suppression calculation, obtained classical ionization rates. Agreement was generally obtained for larger clusters with $n > 10$, but only when the dynamic polarization was taken into account, emphasizing the multi-electron nature of the ionization suppression.

PACS numbers: 33.80.Rv, 33.80.Wz, 36.40.Qv

The study of atoms in strong, non-resonant laser fields has led to the discovery of extreme non-linear optical processes such as ultra-high harmonic, X-ray and attosecond pulse generation. For rare gas atoms, their adiabatic electronic response with respect to optical field oscillations and effective single-electron dynamics permit a quasi-static (QS), single active electron (SAE) treatment of their strong field ionization [1]. Certain polyatomic molecules, by contrast, have extended geometries which can lead to non-adiabatic multi-electron (NME) ionization dynamics and an enhancement of the ionization and fragmentation rates [2–4]. By contrast, in the low-frequency limit many polyatomic molecules are significantly harder to ionize than predicted by QS-SAE models [5, 6]. This resistance may contain contributions from quantum interferences [7, 8] and molecular frame alignment effects [9]. However, in polyatomic systems, another important contribution may be due to a multi-electron response which leads to a dynamic screening of the "active" electron [2, 3, 10]. Here we report on the non-resonant strong field ionization of systems that have an adiabatic electronic response, but contain many polarizable electrons: metal (Ni) clusters. We observed a dramatic suppression of ionization relative to SAE expectations, demonstrating the need for true many-body theories of strong field ionization.

Our goal is to study the failure of single active electron approximations in quasi-static strong field ionization, at threshold intensities. As such, metal clusters, being multi-electron systems whose electronic and geometric properties vary systematically with cluster size, present a comprehensive test for models. The transition metal clusters in particular are very strongly bound, often with bond energies exceeding their ionization potentials. This permits strong field ionization studies without the complications of fragmentation and large amplitude atomic motion leading to "enhanced" ionization effects [12, 13]. Finally, metal clusters are of near spherical symmetry, avoiding strong molecular frame alignment effects.

The strong field ionization of rare gas clusters has included studies of ionization up to highly charged states in a regime where the laser pulse duration is sufficiently long for the oscillating "nano-plasma" to expand and come into resonance with the laser field [14, 15]. These processes have been observed in the strong field ionization of metal clusters [16]. Here, by studying Ni cluster ion yields at their ionization intensity threshold and by choosing sufficiently short laser pulse durations ($<$ 100 fs), we en-

[*]Electronic address: Albert.Stolow@nrc.ca;David.Rayner@nrc.ca

deavoured to avoid atomic motion and plasma oscillation effects. Furthermore, by working in the low-frequency infrared region (1.5 μm), we have attempted to minimize non-adiabatic effects in the electronic response [2]. We characterized the metal cluster ionization process by measuring the intensity dependence of singly and doubly charged cluster ion yields. Extrapolating to the ionization thresholds, we extracted (for each cluster size) the saturation intensities [6] which, importantly, allow for direct comparison with theoretical predictions.

Nickel cluster beams were generated using a kHz-rate laser ablation molecular beam source [17]. An amplified femtosecond Ti:Sa laser pumped an optical parametric amplifier (OPA), producing < 90 fs pulses at 1.5 μm with over 150 μJ of energy [18]. The focused (f/15) infrared laser pulses intersected the metal cluster beam in the extraction region of a linear time-of-flight mass spectrometer (TOFMS). In the metal cluster experiments reported here, discrimination between clusters of different size was achieved post-ionization. As the transition metal clusters exhibit no fragmentation at threshold, the parent ion signal is a direct measure of the net ionization response. Via the multiplexed nature of TOFMS, the response of all cluster sizes was determined under identical laser conditions. The TOFMS axis was orthogonal to the cluster beam and therefore deflection plates were used in the drift region to compensate for molecular beam lab frame velocity. This provided good mass resolution, but windowed the range of cluster sizes that could be monitored in any one single experiment. Mass spectra were recorded for each laser shot using a PCI-based multichannel scaler (MCS). We measured the intensity dependence of each cluster mass peak and varied the laser intensity pseudo-randomly (up to the maximum of 2×10^{14} W/cm^2) using a computer controlled variable neutral density filter wheel. The laser pulse energy was measured on a shot-to-shot basis using an integrating sphere and a GeGaAs photodiode. In order to ensure that the MCS mass spectrum and the (randomly varying) laser pulse energy were recorded in coincidence for each laser trigger event, an amplitude-to-time converter was used to write the pulse energy information as a time delay at the end of each MCS record.

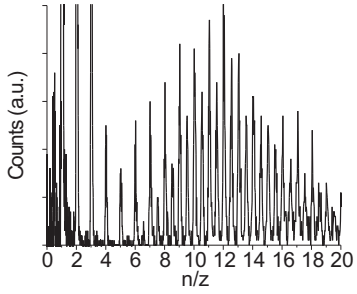

FIG. 1: A mass spectrum of nickel clusters, obtained via strong field ionization at 1.5 μm with an intensity $\sim 10^{14}$ W/cm^2, plotted as a function of the number of nickel atoms, n, divided by the charge state z of the ion. Peaks at half integer n/z correspond to doubly charged clusters. Peaks at integer n/z can have contributions from both singly and doubly charged ions. The singly charged contribution can be estimated by subtracting the average of the neighbouring half-integer peaks.

We implemented the saturation intensity method, employing a constant axial intensity geometry, described elsewhere [5, 6]. Briefly, a narrow (<500 μm) slit placed perpendicular to the laser propagation direction permitted collection only of ions formed in a region of constant axial intensity. With this geometry, a linear dependence of the ionization yield on the logarithm of the intensity obtains at high intensity. The saturation intensity, $I_{\rm sat}$, is defined as the threshold intensity for this (extrapolated) linear behaviour and is a general measure of the "ease" of ionization. As $I_{\rm sat}$ is a molecular property and does not depend on experimental factors such as detection efficiency or focal length, comparison with theory is unambiguous. As described in detail elsewhere, absolute laser intensities (to within 20 %) were determined by standard calibration against the known saturation intensity of atomic xenon [2, 3, 6].

A Ni cluster mass spectrum, shown in figure 1, is plotted as a function of cluster size n divided by cluster charge z. The dominant isotopes of nickel are ^{58}Ni (68%) and ^{60}Ni (26%). This par-

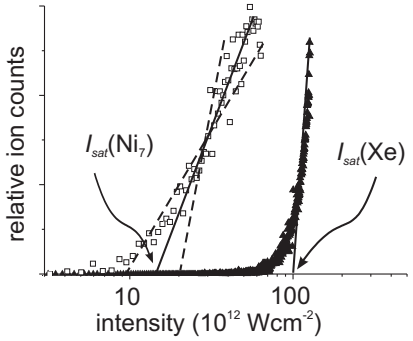

FIG. 2: An example of an intensity dependence study of the ion yield of Ni_7^+ and the calibration standard, Xe. A straight line is fitted to the signal at high intensity. The saturation intensity, $I_{\rm sat}$, is defined as the intercept with the intensity axis. The dashed lines indicate the "worst-case" fits, used to obtain error estimates for the $I_{\rm sat}$. Using an established method, absolute intensities (to within 20%) were determined using atomic Xenon as a reference standard, as described in the text. Analogous plots were obtained for all other cluster masses.

ticular spectrum, obtained at 10^{14} W/cm^2, consists of peaks attributable to both singly and doubly ionized Ni clusters. The spectrum is a function of the cluster size distribution and the TOFMS transmission function. The latter is determined by the voltage applied to the deflection plates, ions of the same n/z having the same transmission factor. In Fig. 1 peaks at half integer values of n/z are solely due to doubly charged ions. Peaks at integer n/z can have contributions from both doubly and singly charged Ni_n. Both singly and doubly charged species contribute to the integer $n = 7 - 12$ peaks. We assign the peaks for $n/z = 1$ to 5 to singly charged Ni_n^+ (no non-integer n/z mass peaks are observed below $n = 6$). The mass peaks for $n \sim 13 - 18$ to are largely due to the doubly charged Ni_n^{2+} species (assuming the Ni_n^{2+} yield to be the average of the Ni_{n-1}^{2+} and Ni_{n+1}^{2+} yields). This information was used to extract the intensity dependence of individual clusters from the measured intensity dependence of the TOFMS peaks. We note that there are no even-odd abundance fluctuations in the Ni systems, unlike those seen in other systems such as the alkalis. Overall the form of the mass spectrum shown in Fig. 1 is that expected from a typical bimodal cluster distribution, peaking at the atom and at $n \geq 30$, with a TOFMS transmission function centred at $n/z \sim 12$. With modifications to the source design, it should be possible to study considerably larger metal clusters, a subject of future inquiry.

We show in Fig. 2 a sample intensity scan for Ni_7^+ production, including the atomic xenon signal obtained simultaneously. Similar plots were obtained for all other cluster species. A straight line was fitted to the ionization yield curve in the linear high intensity region. $I_{\rm sat}$ is the linear intercept with the intensity axis. In Fig. 3 we report $I_{\rm sat}$ as a function of cluster size and charge. The values are the mean obtained from a series of three or more measurements for each cluster. Errors estimated from worst case fits, as illustrated in Fig. 2, include the error in measuring $I_{\rm sat}$(Xe).

A striking conclusion emerging from the data in Fig. 3 is that the Ni atom and clusters are much harder to ionize than expected from simple QS-SAE models, which consider the ionization potential (IP) alone. For example, the Ni atom $I_{\rm sat}$ is 5 times greater than that predicted using the commonly used ADK theory of atomic ionization[19], shown as the open circle in Fig. 3. As $I_{\rm sat}$ is a logarithmic measure, this implies a large suppression of the ionization rate. Simple barrier suppression ionization (BSI) models predict that $I_{\rm sat}$ varies as IP^4, suggesting that low IP clusters such as Ni_7 ($IP = 6.13$ eV) should ionize at much lower intensities than observed here.

In order to develop a simple physical picture of $Ni_n^{(z-1)+}$ ionization, we work within the BSI approximation where $I_{\rm sat}$ is identified with the minimum laser field required to suppress the Coulomb barrier below the IP. For a QS-SAE "atom", the BSI $I_{\rm sat} = (IP)^4/16z^2$ (atomic units). We employed a classical BSI model rather than a tunnel ionization model such as ADK for several reasons: i) BSI predicts saturation intensities in fs ionization of rare-gas atoms fairly well [20]; ii) for low IPs (metal clusters)

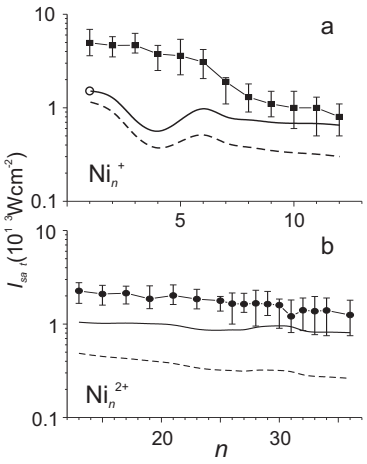

FIG. 3: Cluster size dependence of the ionization saturation intensity, I_{sat}, for (a) Ni_n^+ and (b) Ni_n^{2+}. The error bars were determined as indicated in Fig. 2. Metal clusters have dramatically higher $I_{\rm sat}$ than predicted by simple QS-SAE models. The open circle shows the ADK prediction for the Ni atom. The solid line shows the result of a simple classical conducting sphere, barrier suppression ionization model. The dashed lines show the result of omitting the dynamic polarization term from this simple model. For details, see the text.

ADK becomes less accurate due to the wide barrier and resultant failure of the particular semiclassical tunnelling connection formulae underlying ADK; iii) we expect BSI to become more accurate as the tunnelling contribution is minimized by wider barriers; iv) BSI can be easily and transparently adapted to potentials other than the Coulomb potential used in ADK theory or the zero-range potential used in other tunnelling models.

Although oversimplified, treating metal clusters as classical conducting spheres provides a very simple first-order rationalization of their ionization potentials and polarizabilities [11]. As in C_{60} ionization[10], we adopted a classical conducting sphere model (CSM) to mimic the electronic response of a Ni cluster to an intense laser field in order to gain physical insight into the nature of the ionization suppression. Strong deviations from the CSM are well known for small clusters, but for clusters with $n \sim 15$, convergence to CSM emerges for the polarizabilities, α, of Ni clusters and, in a modified form, for the IPs as well [21, 22].

Assuming an adiabatic electron response, the potential in the direction of the field $\Phi(r)$ felt by a continuum electron due to a charged conducting sphere of a radius a in the presence of an electric field E is [23]:

$$\Phi(r) = -Er + \frac{a^3}{r^2}E - \frac{q}{4\pi\varepsilon}\left(\frac{a}{2(r^2-a^2)} + \frac{z-\frac{a}{2r}}{r}\right) \quad (1)$$

The two terms in the bracket describe the contributions to the potential by the image charge and z. The a^3E/r^2 term is due to the instantaneous dipole induced in the sphere by the laser field - the dynamic polarization. Note that a^3 is directly related to the polarizability, α, of the sphere. Thus, the potential in Eq. 1 includes both the finite size and the polarizability of the cluster, two of the major differences between molecules and the rare gas atoms.

We found the CSM-BSI $I_{\rm sat}$ by numerically computing the field at which the classical barrier is suppressed by exactly the IP. For the first ionization step, we use the previously measured Ni cluster IPs and set $a = (a' + \delta a)$ where a' is the Ni_n radius, calculated from the bulk density, and δa is the spill-out, taken to be 0.74 Å[21]. The results of the CSM-BSI model for the first ionization step are compared with experiment in Fig. 3a (solid line). For the small singly charged clusters, the CS-BSI value for I_{sat} is up to eight times lower than the experimental value. However, as the cluster size increases, the experimental and CSM values begin to converge to within experimental error by $n \geq 10$. For the doubly charged Ni_n^{2+} clusters, there is reasonable agreement with experiment (Fig. 3b), considering that the (unknown) IPs were only estimated from the CSM result $IP_z = IP_{z-1} + q/4\pi\epsilon a$. With these CSM IPs, agreement obtains again in the larger cluster limit.

In order to gain some physical insight into the nature of the ionization suppression, we modified the standard CSM. The dotted curves in Figs. 3a and b show the result of omitting the polariza-

tion term from the CSM. Dynamic polarization is clearly required for any agreement with experiment. For the larger clusters, the agreement becomes quantitative. For smaller clusters, the effect of dynamic polarization is in the right direction but its magnitude is insufficient. In the absence of a simple model, a full quantitative description of dynamic polarization in the small clusters will require detailed many-body quantum mechanical calculations in the presence of a strong external field.

In conclusion QS-SAE models can fail dramatically for multi-electron systems even in the adiabatic, quasi-static limit. Using the saturation intensity method, we observed a dramatic suppression of strong field ionization in size-selected metal clusters. We attributed this to the multi-electron nature of metal clusters: their dynamic polarization in a laser field leads to a dynamic screening of the active electron and a suppression of ionization. In order to gain physical insight, we compared our results to simple classical conducting sphere barrier suppression models and showed that the polarizability term is required in order to get convergence with experiment in the larger cluster limit. We are currently studying the infrared strong field ionization of Vanadium, Niobium and Tantalum metal clusters in order to make further comparisons. The strong field ionization of polyatomic systems can contain, due to failures of the adiabatic and single active electron approximations, physics much richer than that seen in atoms.

Acknowledgments

The authors wish to acknowledge the developmental work of Dr. Michael Schmitt (Univ. Wuerzburg) and we thank P.B. Corkum, M.-Yu. Ivanov, M. Kitzler (Univ. of Ottawa), T. Brabec (Univ. of Ottawa) and E. Zaremba (Queen's Univ.) for valuable discussions.

[1] B. Walker, B. Sheehy, L. F. DiMauro, P. Agostini, K. J. Schafer, and K. C. Kulander, Phys. Rev. Lett. **73**, 1227 (1994).
[2] M. Lezius, V. Blanchet, D. M. Rayner, D. M. Villeneuve, A. Stolow, and M. Y. Ivanov, Phys. Rev. Lett. **86**, 51 (2001).
[3] M. Lezius, V. Blanchet, M. Y. Ivanov, and A. Stolow, J. Chem. Phys. **117**, 1575 (2002).
[4] A. N. Markevitch, S. M. Smith, D. A. Romanov, H. B. Schlegel, M. Y. Ivanov, and R. J. Levis, Phys. Rev. A **68**, 011402 (R) (2003).
[5] S. M. Hankin, D. M. Villeneuve, P. B. Corkum, and D. M. Rayner, Phys. Rev. Lett. **84**, 5082 (2000).
[6] S. M. Hankin, D. M. Villeneuve, P. B. Corkum, and D. M. Rayner, Phys. Rev. A **64**, 013405 (2001).
[7] J. Muth-Bohm, A. Becker, and F. H. M. Faisal, Phys. Rev. Lett. **85**, 2280 (2000).
[8] V. R. Bhardwaj, D. M. Rayner, D. M. Villeneuve, and P. B. Corkum, Phys. Rev. Lett. **87**, 253003 (2001).
[9] I. V. Litvinyuk, K. F. Lee, P. W. Dooley, D. M. Rayner, D. M. Villeneuve, and P. B. Corkum, Phys. Rev. Lett. **90**, 233003 (2003).
[10] V. R. Bhardwaj, P. B. Corkum, and D. M. Rayner, Phys. Rev. Lett. **91**, 172302 (2003).
[11] W. A. de Heer, Rev. Mod. Phys. **65**, 612 (1993).
[12] T. Seideman, M. Y. Ivanov, and P. B. Corkum, Phys. Rev. lett. **75**, 2819 (1995).
[13] C. Rose-Petruck, K. J. Schafer, K. R. Wilson, and C. P. J. Barty, Phys. Rev. A **55**, 1182 (1997).
[14] M. Lezius, S. Dobosz, D. Normand, and M. Schmidt, Phys. Rev. Lett. **80**, 261 (1998).
[15] T. Ditmire, J. W. G. Tisch, E. Springate, M. B. Mason, N. Hay, R. A. Smith, J. Marangos, and M. H. R. Hutchinson, Nature (London) **386**, 54 (1997).
[16] L. Köller, M. Schumacher, J. Kohn, S. Teuber, J. Tiggesbäumker, and K. H. Meiwes-Broer, Phys. Rev. Lett. **82**, 3783 (1999).
[17] M. Smits, C. A. de Lange, S. Ullrich, T. Schultz, M. Schmitt, J. G. Underwood, J. P. Shaffer, D. M. Rayner, and A. Stolow, Rev. Sci. Instrum. **74**, 4812 (2003).
[18] S. Lochbrunner, J. J. Larsen, J. P. Schaffer, M. Schmitt, T. Schultz, J. G. Underwood, and A. Stolow, J. Electron Spectrosc. Relat. Phenom. **112**, 183 (2000).
[19] M. V. Ammosov, N. B. Delone, and V. P. Krainov, Sov. Phys. JETP **64**, 1191 (1986).
[20] S. Augst, D. Strickland, D. D. Meyerhofer, S. L. Chin, and J. H. Eberly, Phys. Rev. Lett. **63**, 2212 (1989).
[21] M. B. Knickelbein, S. Yang, and S. J. Riley, J. Chem. Phys. **93**, 94 (1990).
[22] M. B. Knickelbein, J. Chem. Phys. **115**, 5957 (2001).
[23] J. D. Jackson, *Classical Electrodynamics* (Wiley, New York, 1975), 2nd ed.

7. SUMMARY

In this thesis, the Multi Active Electron (MAE) response in the Strong-Field Ionization (SFI) process is studied. Ionization is the process where a negatively charged electron is removed from the system, leaving behind a positively charged ion. The energy required for ionization can be extracted from an energy source such as a laser. In chapter 1, it is explained that the theoretical description of ionization in strong laser fields is complicated by large energy shifts of the field free Eigenstates of the system (AC Stark shift) and by the increased probability of highly nonlinear interactions. Perturbation theory becomes inapplicable and different approaches have to be developed. First, the two limiting theoretical cases of the description of SFI are introduced. In the first case, Multi Photon Ionization (MPI), the system absorbs an integer number of photons until the ionization energy is exceeded. In the second case, tunnel ionization, a simplified picture can be obtained by considering the electric properties of the oscillating laser field. The potential that binds the electron to the system is modified by the laser field. As a result, a barrier is formed that can be suppressed further by increasing the intensity of the laser. Classically, when the barrier is suppressed sufficiently, the electron can escape over the top of the barrier. In quantum mechanics there is another process possible, called tunneling, where the electron penetrates the barrier before it is fully suppressed. A simple calculation reveals whether ionization takes place in the MPI or tunneling regime: if the time required to tunnel through the barrier is longer than the laser period, the oscillating laser field will change direction before the electron can escape and ionization takes place in the MPI regime. When the tunneling time is fast enough, the ionization process is dominated by tunnel ionization. A major complication in the description of SFI is the response, not of only the tunneling electron, but of all electrons: the MAE response. Traditionally, Single Active Electron (SAE) theories are used instead, which seems to be justified in the case of noble gas atoms. Not very surprisingly, these theories can fail dramatically when applied to MAE systems, like molecules. In this thesis, two qualitative

models are provided to describe the MAE dynamics, as well as a detailed data set that can be used as a test case in the development of quantitative numerical simulations.

As prototype systems, both relatively "simple" transition metal atoms, as well as transition metal clusters are studied. For the latter systems the complexity can be varied by changing the number of atoms per cluster. All measurements take place in the gas phase, where as a function of the laser intensity the ion yield is measured. In chapter 2, the analysis to obtain saturation intensities and absolute ionization rates is presented. The saturation intensities are a measure of the ease of ionization. The absolute ionization rates are obtained by further analysis and require an excellent signal-to-noise ratio. The results are directly comparable with theoretical calculations and provide a major advantage over studies that measure relative rates only. Both the extraction of the saturation intensities and the absolute ionization rates is completely independent of experimental parameters, making the technique universally applicable. In this chapter the vacuum and laser setup is presented as well. The design of a kHz rate laser ablation source to bring the transition metal atoms and clusters into the gas phase, are discussed separately in chapter 3. This unique setup that operates at a repetition frequency of 50 or more times higher than conventional sources, allows for experiments with low count rates as the experiments in this thesis.

In chapter 4, the kHz laser ablation source is used to study the saturation intensities and absolute ionization rates of the transition metal atoms Vanadium (V), Niobium (Nb), Tantalum (Ta), Nickel (Ni) and Palladium (Pd). Even in the case of the relatively simple systems a large discrepancy was found between the experimental data and SAE calculations. The experimental ionization rates are found to be lower by a factor of up to 10^4. The reason for this dramatic suppression of ionization is ascribed to the joint motion of all electrons towards the lower side of the potential: a *dynamic polarization*. The increased density of electrons around the barrier will lead to an increased repulsion of the tunneling electron, *i.e.* a suppression of ionization. An unrealistic but limiting model that is based on the Zero Range Potential (ZRP) is presented. It provides a lower limit for ionization rates of MAE systems, but completely neglects any effect of size. This method makes it possible, however, to bracket the experimental ionization rates between the two limiting cases: SAE and ZRP. A single nonlinear parameter is introduced that is a measure of the contribution of MAE dynamics to the ionization process. Surprisingly, except for niobium, all tested

atoms show a similar contribution from MAE effects irrespective of the number of valence electrons or (static) polarizability. The niobium atom shows a much higher contribution of MAE effects and virtually behaves as if it had a ZRP.

Saturation intensities for the clusters of V/Nb/Ta and Ni are presented in chapter 5. Once more, all saturation intensities are found to be higher than predicted by SAE theories, which is equivalent to an underestimation of the ionization rates. To quantitatively describe the ionization process for larger clusters, a classical method is employed. The cluster is described as a small metal sphere and the MAE effect is taken into account by the polarizability of the sphere. Except for niobium, all clusters converge to this model within the investigated range of number of atoms per cluster. The anomalous results of niobium (the extremely large contributions of MAE effects and the slow convergence of the clusters to classical behavior) might be related to the large fluctuations measured in the static polarizability of its clusters.

Finally, part of the results of this thesis are presented in chapter 6 in the orignal format as they are published in two separate Letters in the scientific journal "Physical Review Letters".

8. SAMENVATTING

De vertaling van de titel van dit proefschrift in het Nederlands luidt: “Multi-Actieve-Elektron invloeden bij de Intens-Veld-Ionisatie van atomen en clusters van overgangsmetalen”. Ionisatie is het proces waarbij één of meer negatief geladen elektronen van een deeltje, bijvoorbeeld een molecule, worden verwijderd en een positief geladen ion achterblijft. Eén van de manieren om dit te bewerkstelligen, is om gebruik te maken van een lichtbundel zoals een laser. In de inleiding van dit proefschrift (hoofdstuk 1) wordt aangegeven hoe de beschrijving van ionisatie in intense velden wordt gecompliceerd door de grote correcties van de veldvrije Eigentoestanden van het systeem en door de toename van de waarschijnlijkheid van niet-lineaire interacties. Storingstheorie is niet meer toepasbaar en alternatieve beschrijvingen zijn nodig. Eerst worden twee limieten uitgelegd om het proces van Intens-Veld-Ionisatie (IVI) theoretisch te beschrijven. In de ene limiet, MultiFoton-Ionisatie (MFI) , wordt een geheel aantal fotonen geabsorbeerd totdat de gecombineerde energie van de fotonen meer bedraagt dan de ionisatieenergie. In de andere limiet spreekt men van tunnel ionisatie, waar de oscillerende elektrische eigenschappen van licht direct worden gebruikt om het elektron te verwijderen. In het ongestoorde systeem (in afwezigheid van het laserveld) is het elektron gebonden aan het systeem door de Coulombinteractie dat een zogenaamd potentiaaloppervlak vormt. Door de interactie van het molecule met het laserveld kan deze potentiaal vervormd worden waarbij een barrière ontstaat. In de klassieke mechanica moet deze barrière zodanig verlaagd worden, dat het elektron over de top van de barrière kan ontsnappen. In de kwantummechanica is er echter een additioneel proces mogelijk, genaamd “tunnelen”, waarbij het elektron door de barrière heen kan bewegen. Met een eenvoudige berekening kan bekeken worden of het elektron voldoende tijd heeft om door de barrière heen te bewegen voordat het oscillerende elektrische veld van het licht van richting verandert. Alleen als dit het geval is, vindt ionisatie plaats in de tunnellimiet, anders wordt het ionisatie proces gedomineerd door MFI. Een groot probleem in de theoretische beschrijving van IVI is

dat in het algemeen niet alleen het tunnelende elektron reageert op het aangelegde veld, maar ook alle andere elektronen in het systeem: de Multi-Actieve-Electron (MAE) respons. Helaas bestaat er op dit moment geen kwantitatieve theorie die alle elektron-elektron interacties kan beschrijven. Er wordt daarom veelvuldig uitgegaan van de beschikbare Eén-Actief Elektron (EAE) theorieën, hetgeen een redelijke aanname lijkt voor toepassing op edelgas atomen. Het is echter gebleken dat deze theorieën, niet geheel onverwacht, dramatisch falen wanneer ze worden toegepast op MAE systemen, zoals moleculen. In dit proefschrift worden twee kwalitatieve modellen gepresenteerd voor de beschrijving van IVI voor MAE systemen, alsmede gedetailleerde data die gebruikt kunnen worden als referentie bij de ontwikkeling van nieuwe kwantitatieve MAE theorieën.

Als prototype MAE-systemen voor de studie van IVI zijn zowel relatief eenvoudige overgangsmetaalatomen onderzocht, alsmede de clusters van overgangsmetalen waarbij de complexiteit kan worden gevarieerd via het aantal atomen per cluster. Alle metingen in deze studie zijn verricht in de gasfase. Als functie van de laserintensiteit wordt de productie van ionen gemeten en in hoofdstuk 2 wordt de analyse van de data beschreven om saturatie-intensiteiten (I_{sat}) en absolute ionisatiesnelheden te bepalen. De waarde van I_{sat} is een indicatie om aan te geven hoe "eenvoudig" een system te ioniseren is. Om de absolute ionisatie snelheden te verkrijgen, worden de data verder geanalyseerd. Een uitstekende signaal-ruis verhouding is vereist voor deze analyse. De resultaten van deze analyse zijn direct te vergelijken met theoretische berekeningen, hetgeen een groot voordeel oplevert ten opzichte van studies waar relatieve ionisatiesnelheden worden gemeten. De bepaling van zowel I_{sat} als de absolute ionisatiesnelheden is volledig onafhankelijk van experimentele parameters en is daarom algemeen toepasbaar. In dit hoofdstuk wordt tevens de vacuüm- en laseropstelling in detail besproken. In hoofdstuk 3 wordt apart beschreven hoe de metaalatomen en -clusters in de gasfase worden gebracht. Het ontwerp van een unieke laserablatie opstelling wordt beschreven die een 50 keer hogere repetitie frequentie heeft dan bestaande opstellingen. De hogere repetitie frequentie van de laser ablatie opstelling maakt experimenten met weinig signaal mogelijk zoals de metingen uit dit proefschrift.

De opstelling voor laserablatie is allereerst gebruikt om I_{sat} en absolute ionisatiesnelheden te meten voor de overgangsmetaalatomen Vanadium (V), Niobium (Nb), Tantalum (Ta), Nikkel (Ni) en Palladium (Pd) (hoofdstuk 4). Zelfs in het geval van deze relatief eenvoudige systemen wordt een grote discrepantie

gevonden tussen de experimentele data en EAE theorieën: de experimentele absolute ionisatiesnelheden zijn tot een factor 10^4 lager. De MAE respons van de onderzochte atomen leidt tot een gezamenlijke beweging van alle elektronen in de richting van de barrière waar het tunnelende elektron doorheen moet ontsnappen: een dynamische polarisatie. Het resultaat is dat het tunnelende elektron wordt afgestoten door de verhoogde dichtheid van elektronen rond de barrière en dientengevolge dat de ionisatiewaarschijnlijkheid verminderd wordt. Een onrealistisch model wordt voorgesteld dat echter wel een onderlimiet stelt aan de ionisatiesnelheid. Dit model is gebaseerd op een uiterste geval, de deltapotentiaal, waarbij ieder effect ten gevolge van de grootte van het systeem verwaarloosd wordt. Het is nu mogelijk de experimentele ionisatiesnelheid te plaatsen tussen de overschatting door EAE theorieën en de onderschatting van het uiterste model gebaseerd op de deltapotentiaal. Een nieuwe niet-lineaire parameter wordt geïntroduceerd die de MAE contributie aan het proces van ionisatie als een percentage weergeeft. Verrassend is dat voor alle geteste atomen, met uitzondering van niobium, ongeacht het aantal valentie-elektronen en de polariseerbaarheid, dit percentage min of meer gelijk is. Voor het niobiumatoom wordt een veel hoger percentage gevonden en een beschrijving door middel van een deltapotentiaal geeft zelfs quantitatieve overeenstemming.

In hoofdstuk 5 wordt I_{sat} voor de clusters van V/Nb/Pd en Ni gerapporteerd. De waarden voor I_{sat} van de onderzochte atomen zijn wederom hoger dan de waarden voorspeld met EAE theorieën (oftewel de ionisatiesnelheden zijn lager). Hier wordt een klassiek model geïntroduceerd, waarbij het cluster als een heel klein bolvormig object wordt beschreven. De MAE dynamica van het ionisatie proces wordt beschreven via de polariseerbaarheid van dit object. Voor alle geteste metalen, behalve niobium, convergeren de experimentele data naar dit model binnen het geteste meetgebied. Het wederom afwijkend gedrag van niobium is wellicht terug te voeren op de extreme variatie die gemeten is in de polariseerbaarheid van niobiumclusters als functie van clustergrootte.

Tenslotte worden twee korte publicaties met de resultaten van dit proefschrift gepresenteerd in hun oorspronkelijk vorm zoals verschenen in het wetenschappelijk tijdschrift "Physical Review Letters" (hoofdstuk 6).

9. DANKWOORD/ACKNOWLEDGMENTS

After all these pages I have to admit that it was a lot of work, but at the same time that the four years I spent in the Femto-Group of the the National Research Council in Ottawa were AWESOME! In this final part of my thesis I would like to thank all the people that were involved in one or the other way to make this time scientifically and socially a part of my life I will never forget.

Allereerst zou ik graag mijn promotor, Kees de Lange, willen bedanken die het in de eerste plaats voor mij heeft mogelijk gemaakt om een promotie-onderzoek in Canada uit te voeren en daarnaast een feilloos vertrouwen had in mijn voortgang zonder de regelmaat van mijn beloofde e-mails. Aan het eind van mijn promotie onderzoek is Wim Ubachs mijn co-promotor geworden en heeft mij belangeloos bijgestaan in het regelen van alle vereiste formaliteiten voor de afronding van mijn promotie.

Next is Albert Stolow who was my official supervisor in Ottawa, but very soon became a true friend. I would like to thank you for your scientific contribution to my thesis, but also for your typically Canadian friendliness. Another great contribution to this work was made by Dave Rayner who also taught me the black magic of producing metal clusters (at kHz rates!). Furthermore it was a great honor to work in the challenging group of Paul Corkum with David Villeneuve, Misha Ivanov and Genady Yudin. I would like to continue by thanking the knowledgeable and skilled technicians without whom not a single experiment described in this thesis could have been completed successfully: Shutao Li, John Parsons, Bert Avery and Dave Joines.

Over the years I got to know many Femto's from all over the world and I would like to thank you all for an extremely nice working climate. I would like to mention Schmiddi and Johnaton, as well as Adrian and Jeff who specifically contributed to this work. Also I would like to thank my fellow graduate students for the fun times we had in the lab: Tony, Lu(l)lo and our Viking. The stress after a frustrating day with failing experiments was quickly relieved with a hockey game of the NRC-Beavers, including Fabien, Igor, Thomas, James, Oli,

Dirk, Zhenia and Jenny.

From the collaboration with the theoretical group of Thomas Brabec at the University of Ottawa (the Romy Schneider Institute) came not only very useful results, but also a few very good friends: Woody, Jürgen and Christian.

Tenslotte wil ik mijn ouders bedanken die mij in de afgelopen (bijna) drie decenia vanaf mijn eerste woordje "GOM" tot en met de voltooiing van dit boekje altijd hebben gestimuleerd om mijn doelen te bereiken. Jullie frequente bezoeken, maar ook die van mijn zus Marion, zusje Marijne en "oudste" vriend Martijn, hebben geholpen om Nederland niet altijd te zeer te missen. Echter, de belangrijkste persoon, zonder wie ik mijn periode in Canada nooit tot een succesvol einde gebracht zou kunnen hebben, is mijn allerliefste Puffin. Ik zal nooit vergeten hoe je speciaal voor mij naar het barre Canada bent gekomen en ik zal de herinneringen aan onze reis tot in Red Bay (Labrador) voor altijd koesteren.

Marc